University College London

Molecular Simulations of Ionic Liquids for CO_2 Capture

Thesis submitted for the degree of Doctor of Philosophy (PhD) by

Qamreen Parker

Supervised by

Prof. Nora H. de Leeuw and Dr Robert G. Bell

University College London

Department of Chemistry

December 2017

Declaration

I, Qamreen Parker, confirm that the work presented in this thesis is my own. Where information has been derived from other sources, I confirm that this has been indicated in the thesis.

Qamreen Parker

December 2017

Abstract

Ionic liquids (ILs) are molten salts at temperatures below 100 °C or at room temperature, achieving this by possessing ions that pack weakly, preventing the formation of a stable crystal lattice. The very low or non-existent volatility of the liquids is one of the most important reasons for why ILs are explored for carbon dioxide (CO_2) capture, along with interesting properties such as thermal stability, nonflammability and tunability for high CO_2 solubility. It is therefore important to understand, at a molecular level, the structure and properties of ILs.

The work presented in this thesis employs classical molecular dynamics (MD) simulations to investigate ILs at varying temperature and varying loadings of CO_2. Initially, the interatomic potentials or force field (FF) that can be used to simulate ILs are researched, before choosing two: The Generalised Amber FF (GAFF) and Canongia Lopez and Padua FF (CL&PFF). After a comparison of densities and structures resultant, further validation on the CL&PFF is reported.

Subsequently, a phosphonium based IL, $[P_{66614}][NTf_2]$, is investigated in a pure state at varying temperatures, to compare with experimental data. We study the density, structure and diffusion of the system, in terms of cation, anion and ion pair. We reinforce the results of our initial FF comparison, as the density is calculated to a high degree of accuracy compared with experiment. We continue to describe the influence of temperature on the structure and dynamics, comparing with experimental data where available. Finally, we considered the IL's reported CO_2 solubility and explored different loadings of CO_2 in the IL system. We observe significant changes in IL structure and diffusion with even small loadings of CO_2, along with interesting CO_2 interactions and diffusion.

Following on from this, we detail the initial modelling of a phosphonium based superbase ionic liquid, with a combination of FFs and scaling of atomic charges to better detail the diffusivity of the IL. Thus, in this thesis, we present ILs as a media that offers significant performance benefits when compared to traditional organic solvents for carbon capture. Additionally, we confirm the suitability of MD simulations for the accurate description and elucidation of structural and diffusive properties of ILs.

Acknowledgements

Firstly, I would like to thank my supervisors, Professor Nora H de Leeuw and Dr Robert G Bell, for providing me with the opportunity to carry out this PhD research as well as, the support and guidance throughout the years. I am very grateful for the direction and the friendly atmosphere during our meetings. Additionally, I would like to thank all the members of the de Leeuw and Bell groups, who always provided help, debate and laughs when most needed. I would also like to acknowledge the EPSRC for the funding and the computing facilities used in this work: Archer, UCL's Legion and Grace.

Finally, I want to thank my family and friends for all the love, support and encouragement throughout this PhD.

Table of Contents

List of Publications and Conferences

- Parker, Q.; Bell, R. G.; De Leeuw N. H. Structural and Dynamical Properties of Ionic Liquids: A Molecular Dynamics Study Employing DL_POLY 4. **Molecular Simulation**. Submitted February 2018

- Poster Presentation: Q. Parker, M, Mercy, R. G. Bell and N. H. de Leeuw. **MGMS Young Modeller's Forum**. London 2014

- Poster Presentation: Q. Parker, M, Mercy, R. G. Bell and N. H. de Leeuw. **M3S CDT Annual Industry Day**. London 2014

- Oral Presentation: Q. Parker, M, Mercy, R. G. Bell and N. H. de Leeuw. Molecular Dynamics Modelling of Ionic Liquids for CO_2 Capture. at '**The Science behind CO_2 Capture and Conversion'**, Cuba 2015

- Oral Presentation: Q. Parker, M, Mercy, R. G. Bell and N. H. de Leeuw. At **'International Conference on Carbon Dioxide Utilisation'**, Sheffield 2016, and Poster Presentation, Winner of CO_2Chem Poster prize.

List of Abbreviations

AHA:	Aprotic heterocyclic anion
BMIM:	1-Butyl-3-methylimidazolium
CC:	Carbon capture
CCS/U:	Carbon capture, storage /and utilisation
CL&PFF:	Canongia Lopez and Padua Force Field
DCA:	Dicyanamide
EMIM:	1-Ethyl-3-methylimidazolium
FF:	Force Field
FIL:	Functionalised ionic liquid
GAFF:	Generalised Amber Force Field
IL:	Ionic liquid
IP:	Ion pair
MD:	Molecular dynamics
MEA:	Monoethanolamine
MSD:	Mean square displacement
NTf_2:	Bis(trifluoromethylsulfonyl)imide
OAc:	Acetate
P_{66614}:	Trihexyl(tetradecyl)phosphonium
RDF:	Radial distribution function
SDF:	Spatial distribution function
TSIL:	Task-specific ionic liquid

List of Tables

List of Figures

Chapter 1

Introduction

In this chapter, we introduce the research objectives of this PhD thesis, the field of carbon dioxide capture and current methods and media used in industry. Following this, the uses and properties of ionic liquids are explored with the aim of explaining the benefits of researching these as a medium for carbon dioxide capture. Finally, we provide an overview of computational simulations of ionic liquids reported in the literature.

1.1 Research Overview

The global annual temperature has increased by an average rate of 0.17°C per decade since 1970; [1], [2] the steady increase of CO_2 levels in the atmosphere due to processes such as fossil fuel burning is correlated to this global warming. Thus, capturing CO_2 to prevent pollution to our atmosphere is an important action. Ionic liquids (ILs) are salts containing poorly coordinated ions, due to them consisting of bulky or organic groups. Thus, the salts are liquid at below 100°C or room temperature. ILs have recently been reported to have high CO_2 capacities and are thus worthy of research as a medium for industrial CO_2 capture.

For ILs to be used for carbon capture processes, detailed descriptions and explanations of CO_2 sorption on various ILs are required. Specific ILs have been chosen based on experimental collaborators' work at the University of Sheffield and Queen's University Belfast, all for a larger project "A Comprehensive and Coordinate Approach to Carbon Capture and Utilisation" (4CU).[3] "Task-specific" ILs (TSILs) which chemically (and physically) react with CO_2 in a reversible manner will be considered the long-term goal of the project.

Molecular Dynamics (MD) simulations are widely-used and well-known: bridging the gap between experimental results (such as sorption capacities, densities, viscosities etc.) and chemical theory. For instance, detailed atomistic representations of the molecular structure can be seen with simulations that can substantiate experimental measurements of properties and structure, such as spectroscopic data. Various physical and chemical properties are needed, such as density and viscosity, to support experimental data and provide vital theoretical explanations. This provides the basis of the research project undertaken for the length of this PhD.

1.2 Carbon Capture, Storage and Utilisation

One of the main contributions to man-made atmospheric CO_2 emissions is from the power sector, where CO_2 is released during the burning of fossil fuels. Other industrial processes such as making cement, iron and steel or chemical plants are also responsible for copious quantities of CO_2 production. Thus, methods of carbon capture, storage /and utilisation (CCS/U) are required at these point sources. At fossil-fuel burning power plants, the resultant flue gas (*i.e.* post-combustion gas exiting to the atmosphere) is made up of nitrogen, carbon dioxide and water vapour, with a smaller percentage of soot, nitrogen and sulphur oxides. The flue gas from an anaerobic digester however would predominantly consist of methane and CO_2. These exiting flue gases require CO_2 removal, as without this, large volumes of CO_2 would escape to the atmosphere.

1.2.1 Carbon Capture Routes:

Carbon capture technologies can be implemented through three ways which are described below: [4]

1.2.1.1 Post-combustion Capture

With this route, separation of CO_2 is mainly from N_2 in flue gas from the combustion process, *i.e.* end-of-pipe, shown in Figure 1.1. This is normally at atmospheric pressure and low CO_2 content (3-20 %).[5] A benefit of this route is that that can be an “add-on” technology, meaning it can retrospectively be fitted to older plants.

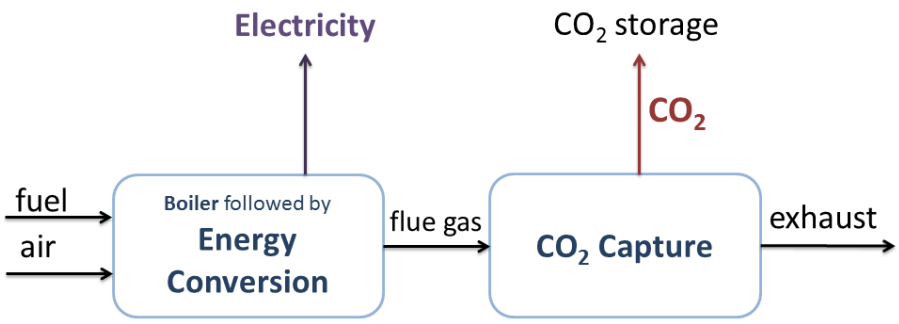

Figure 1.1. Flow-diagram of post-combustion carbon capture.

1.2.1.2 Pre-combustion Capture

At the beginning of this process is the conversion of fossil fuels (*via* methane) into syngas. CO_2 is captured from H_2 in shifted syngas, which is prior to combustion, graphically represented in Figure 1.2. There is a high CO_2 partial pressure, allowing for a less energy intensive process compared to post-combustion capture. However, this method requires the capture equipment to be integrated into the overall process.

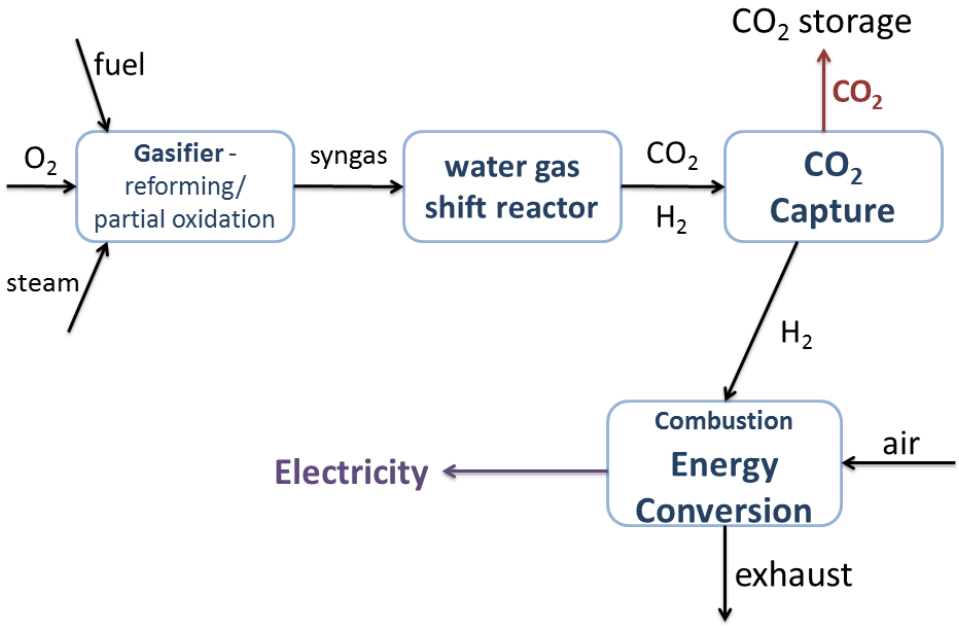

Figure 1.2. Flow-diagram of pre-combustion carbon capture.

1.2.1.3 Oxy-fuel (denitrogenated) Combustion Capture

This method involves separation of oxygen (O_2) from nitrogen (N_2) in air prior to combustion, as depicted in Figure 1.3. The fuel is combusted in oxygen diluted with recycled flue-gas rather than air, to control the temperature. This O_2-rich, N_2-free atmosphere results in final flue gases consisting mainly of CO_2 and water (H_2O). Thus, a high concentration CO_2 stream is produced for easier purification.

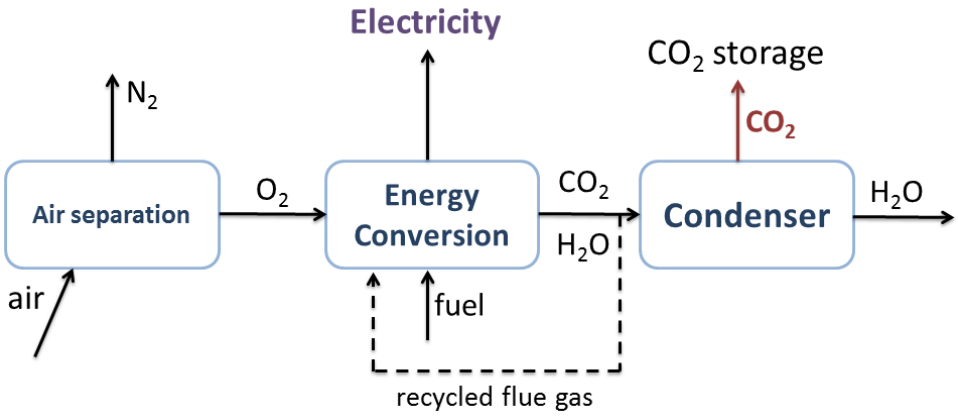

Figure 1.3. Flow-diagram of Oxy-fuel combustion capture.

To summarise the capture routes, Table 1.1 compares the different capture routes with three key aspects.

Table 1.1. Carbon Capture routes compared for gas mixture of separation, process pressures and [CO_2] percentage concentrations.

	Post-Combustion (flue gas)	**Pre-Combustion (shifted syngas)**	**Oxy-fuel Combustion (exhaust)**
Separation	CO_2-N_2	CO_2-H_2	O_2-N_2
Pressure (bar)	~ 1	10-80	~ 1
[CO_2] (%)	3-15	20-40	75-95

1.2.2 Current Mediums for CCS/U

The foremost Carbon Capture (CC) method currently being employed at power plants is amine scrubbing. Monoethanolamine (MEA) has a relatively fast and high CO_2 absorption capacity with low viscosities, and as such is usable in mass scaled CC scrubbers in power-plants. Low viscosities are required to keep a good movement of the solvent for optimum uptake. Typically 20/30% wt % MEA solutions are used and these separation methods have been known and utilised for over 70 years, at first separating CO_2 from natural gas and hydrogen.[6] As organic solvents, amine solutions are corrosive and incredibly volatile – adding to harmful emissions and needing replenishment in the process. Prone to thermal and chemical degradation, the operative temperature range is also restricted, adding to the list of inefficiencies. However, the key obstacle to the cost of this method is the large enthalpy of reaction; thus regeneration of the CO_2 has an extremely large energy barrier.[7], [8]

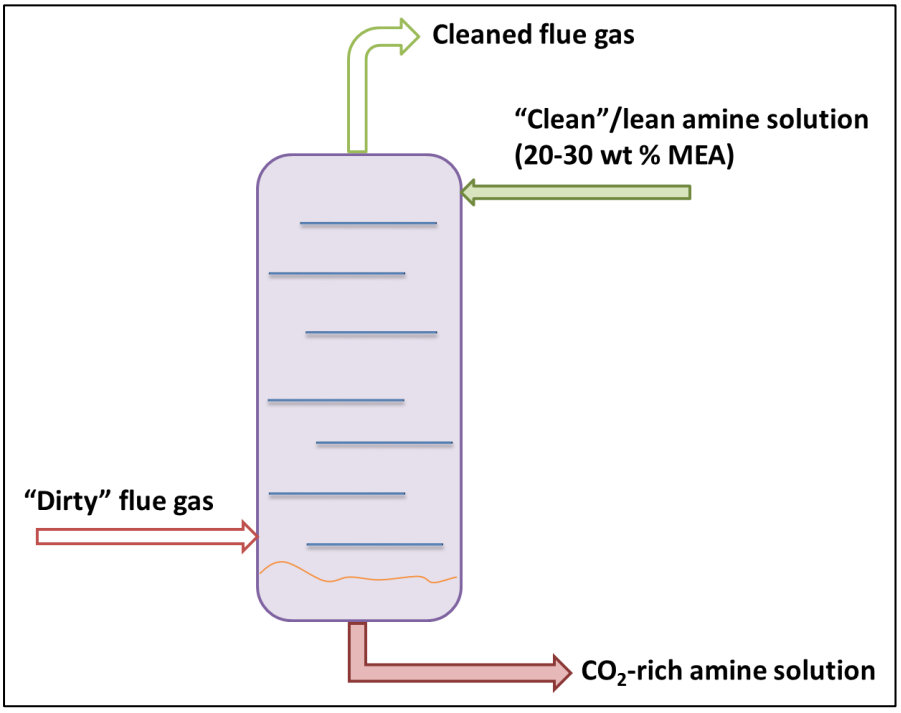

Figure 1.4. Simplified schematic of a CO_2 capture scrubber, highlighting the need for low volatility, low viscosity liquids that efficiently absorb CO_2.

Some examples of inorganic solvents for CC are aqueous ammonia or potassium carbonate. Whilst these solvents involve a lower operational temperature (*e.g.* chilled ammonia), the energy requirements at regeneration are similar to that of the MEA method.[9] With high energy inputs and other operational complications associated with the above conventional methods, it is apparent that whilst CC is important it is also important the process of CC is cost-effective, easy to implement and itself environmentally benign. An ideal solution would be a novel liquid solvent that be applied in the conventional scrubber method (Figure 1.4). Storage of the CO_2 is usually deep underground and achieved by injection into carefully surveyed and selected geological formations. Instead of being stored, the carbon captured can also be utilised to make useful fuels, which is still a relatively uncharted field and hence a significant addition to the collaborative 4CU project detailed in 1.1 Research Overview.

1.2.3 New Prospects for CO_2 Capture

There are different types of processes applied to research on CC: the use of solvents/sorbents that either absorb or adsorb the CO_2, the use of membranes to separate the CO_2 or cryogenic separation.[10] Sorption of the CO_2 can either be chemical (when chemical bonds are made/broken) or physical (no chemical bonds are made but instead intermolecular forces hold the CO_2 to the solvent). The literature exploring and reporting the design and testing of innovative solvents/sorbents has rapidly increased over the years; micro-porous materials such as zeolites, metal oxides and metal-organic frameworks are all examples of new prospects explored for CCS/U and are the focus of much work and review.[7], [11], [12]

Blanchard *et al.* (The Brennecke group) in 1999 were the first to publish ILs' ability to dissolve CO_2 (Figure 1.5).This process was reported to be reversible, with pure IL

achieved on the release of the CO_2.[13] ILs for CO_2 capture and green processes is popular research around the world.[14], [15] Anderson *et al.* even found ILs a suitable medium for the physical absorption of SO_2 gas.[16]

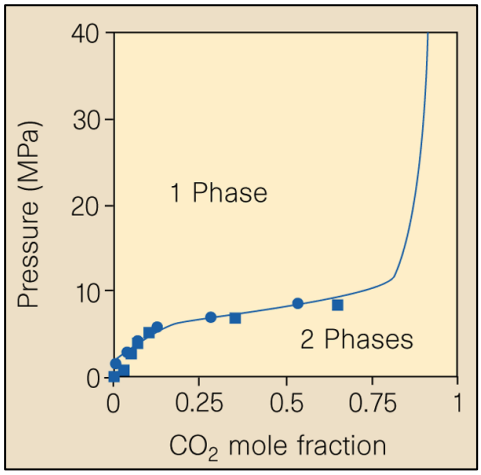

Figure 1.5. Absorption isotherm of CO_2 in 1-butyl-3-methylimidazolium hexaflourophosphate [BMIM][PF_6], showing highly soluble nature of CO_2 in the IL, without the IL dissolving in the CO_2. Figure reproduced with permission from paper by Blanchard *et al.* [13]. Copyright 1999 by Springer Nature.

1.3 Ionic Liquids for Carbon Capture

1.3.1 Discovery and History of ILs

Conventional inorganic salts are known for their crystalline properties; strong electrostatic attraction between the ions yields a close packing lattice that requires high temperatures to melt *e.g.* 845 °C for LiF. Ionic liquids, on the other hand, are made up of two moderately bulky (or one very bulky) oppositely charged ions. Due to the inability of these bulky ions to close-pack, the cohesive energy is remarkably low making these organic salts low-temperature (< 100 °C) melting compounds. The vastly tuneable properties of ionic liquids are very advantageous for many uses; ILs

can be made up of a variety of ions, and these ions can contain functional groups. These alterations can change the physical and chemical properties of the IL, for instance the viscosity or density.

Whilst the date of discovery of ILs is not definitive (the earliest publication known describing an IL, ethylammonium nitrate, is by Paul Walden in 1914),[17] it can be concluded that the research field has been steadily growing for the last century.[18] The range of uses and consequently literature on the topic of ILs has exponentially increased over the past two decades, mainly due to the use of them as "green solvents" – non-volatile, environmentally benign solvents.[19] Specific applications of ILs vary from electrochemical devices (*e.g.* batteries, thermo-electrochemical cells etc.),[20] organic synthesis and catalysis,[21] and solvent extraction.[22]–[24]

There is a truly enormous field of ILs already being researched, but with "one million possible simple systems, then there are one billion (10^{12}) binary combinations of these, and one trillion (10^{18}) ternary systems possible"[25] the surface of possibilities has only been grazed.

1.3.2 Conventional Ionic Liquids

The first IL used in the experiments with CO_2 was 1-butyl-3-methylimidazolium hexafluorophosphate [BMIM][PF_6]. The Brennecke group found a high solubility of CO_2 in this IL, reaching a mole fraction of 0.6 at 8 MPa, and it is stable in oxygen and water. However whilst an environmentally friendly "green process" was reported – the removal of organic pollutants - it was the process of using supercritical CO_2 to extract non-volatile naphthalene from the IL, not using ILs for CC.[13] Nonetheless, following on from the Brennecke group's findings, studies into ILs, the interaction of ILs with CO_2 and thus research into ILs in CC has increased all over the world,[19] with a large

emphasis on imidazolium-based cations with [PF_6] and [Tf_2N] anions. A trend was seen in anion fluorination and CO_2 capture; the more fluorine atoms present the higher the CO_2 solubility.[8], [26] Ultimately, the use of conventional ILs is limited by physical sorption so the next step to achieving greater sorption is by incorporating chemical, in addition to physical, sorption.

1.3.3 Functionalised Ionic Liquids (FILs)

When a functional group is added to the one or both ions of the IL, the resultant IL is called functionalised and this is usually done to tune the IL to a specific task. As these task-specific ILs (TSILs) had been tested for synthetic and separation purposes,[15], [27], [28] Davis, Jr *et al.*[29] were the first to synthesise and report CO_2 capture using an amine functionalised IL based on the imidazolium ion with a non-functionalised BF_4 anion. However, due to a similar reaction scheme as with organic amines, a limited stoichiometry of 1:2 (CO_2: IL) is seen and shown in Figure 1.6. The mechanism involves the formation of a carbamate; stabilisation of the carboxylic and amine groups by charge separation to make a carbamate salt.

Unfortunately, this promising 1:2 capacity is countered by the large increase in viscosity of the IL, so noted by the de Haan group. They reported the same increase in CO_2 absorption compared to non-functionalised ILs but expanded on the concept with primary and tertiary amine groups present.[30] That being said, the Davis group were successful in introducing TSILs for CO_2 capture to the research scene, which led to further research into amine functionalised ionic liquids and the leap to amino acid functionalised ILs.

With the addition of these functional groups that can chemically react with CO_2, these TSILs are basically adapted to allow for both physical absorption (as seen in conventional ILs) and chemical sorption.

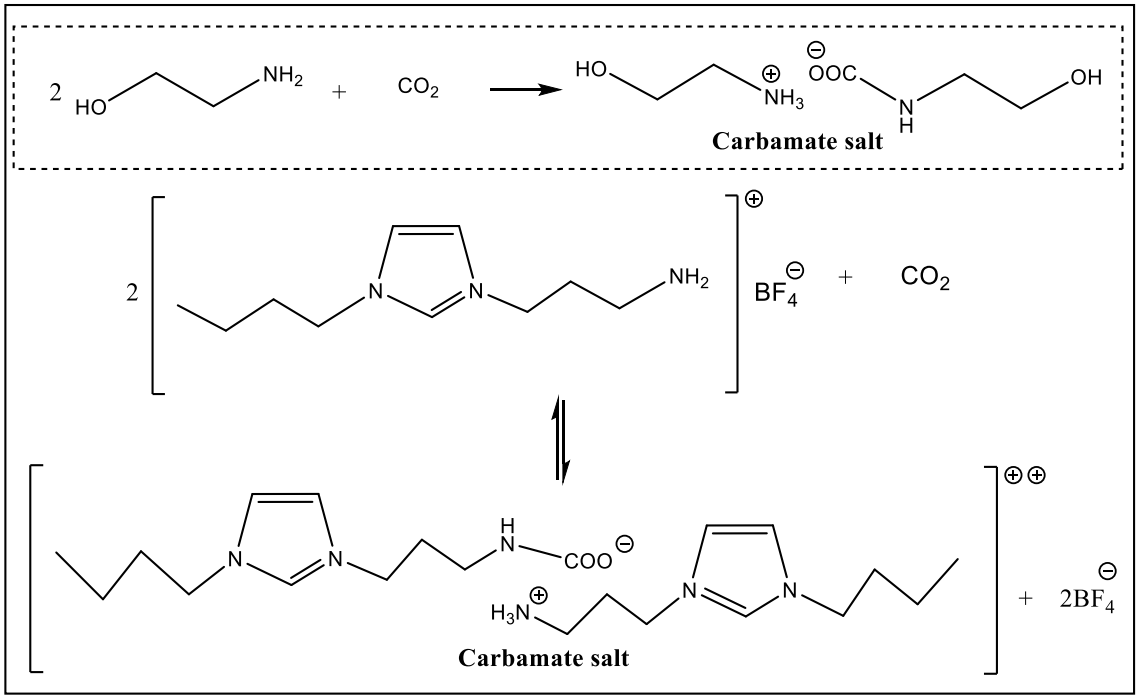

Figure 1.6. Reaction scheme for MEA with CO_2, compared to reaction of TSIL and CO_2, as proposed by Davis *et al.*[29]

In 2006, Zhang *et al.* reported a difference between the previously attempted cation amine functionalization and a new type of anion functionalised IL, amino acid ILs (AA ILs).[31] These were based on tetrabutylphosphonium [P_{4444}] and AAs glycine, L-alanine, L-serine and L-lysine. Their results were that in water (1 wt. %), close to equimolar sorption can be seen with these wet ILs, however dry, at equilibrium, the same 50 mol % limited stoichiometry is seen as with the simpler cation amine FILs.[31] Unfortunately, this paper along with the Ohno group's work on AA FILs[32], [33] ultimately concluded the same 1:2 stoichiometry (even though increased capacities were seen) and a crucial scientific opportunity was missed. Nonetheless, the ILs were economical and exhibited a good capacity of CO_2 at low temperatures.

As a result, the Brennecke group once again took the lead; they published findings on AA FILs trihexyl(tetradecyl) phosphonium methioninate [P_{66614}][Met] and prolinate [P_{66614}][Pro] absorbing CO_2 with equimolar (1:1) sorption.[34] This paper was crucial as it proposed a reaction scheme (Figure 1.7) for the 1:1 reaction of CO_2 with the AA FILs. This mechanism was three times proven: measured heats of absorption and reaction, FTIR spectroscopy showing key features - one of which is the lack of ammonium formation (this would be present for the 1:2 amine mechanism in Figure 1.7) and corroborative computational calculations. The use of quantum mechanical/ab initio calculations on anion-tethered amine group and cation-tethered amine groups were used to explore which ion functionalization favoured 1:1 and 1:2 stoichiometry and it was shown that indeed amine functionalisation on the anion favoured the 1:1 mechanism (Figure 1.7) whilst tethering to the cation favours the less promising 1:2 stoichiometry (Figure 1.6). The findings are significant in showing that these AA FILs can absorb CO_2 with a high molar capacity compared to cation-functionalised ILs and organic amine solvents. Another degree of freedom is also added; changing the specific location of the functional amine group on the anion can also alter the properties of the IL.[34]

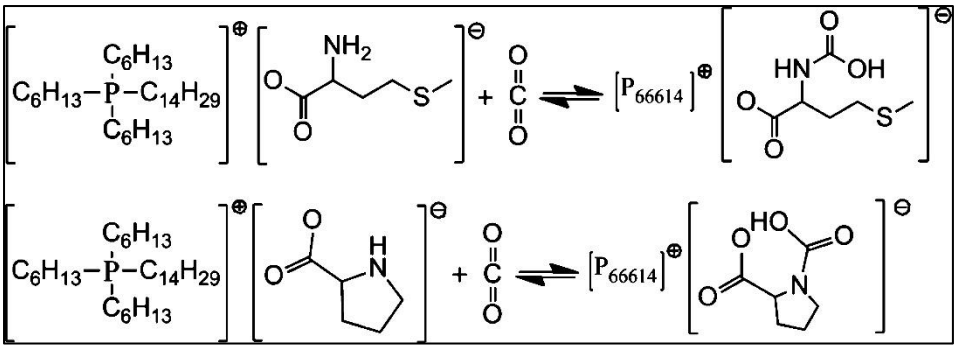

Figure 1.7. Reaction Scheme for 1:1 stoichiometry with amino acid functionalised ILs [P_{66614}][Met] (above) and [P_{66614}][Pro] (bottom), taken with permission from [34]. Here there is no ion pair mechanism leading to the carbamate salt.

The group added more phosphonium AA FILs to their findings in subsequent publications,[35], [36] with AAs anions such as glycinate, alanate, sarcosinate, valinate, leucinate, isoleucinate[29] and asparaginate, glutaminate, lysinate etc.[36] It is significant to note here that whilst most of these AA FILs followed the 1:1 (efficient) stoichiometry, large increases in viscosities once CO_2 is absorbed was seen throughout the group. This dramatic jump in viscosity is thought to be affected by the number of hydrogens on the anion; decreasing the number of hydrogens on the anion available for hydrogen bonding will allow for less viscous final liquids.[35], [37] Significantly, $[P_{66614}]$[Pro] has the smallest increase in viscosity (only double, compared to the usual two orders of magnitude increase for other AA FILs).[26], [36] An explanation put forward by the group regarding this is the ring structure that possibly limits the hydrogen bonding that can occur.

Another example of anion FILs for CO_2 capture is the use of carboxylate anions, *e.g.* acetate ions. This has received special attention for the significantly lower energy input required in the regeneration step, patented by Chinn *et al.* in 2005 who showed that 1-butyl-3-methylimidazolium acetate [BMIM][Ac] with 14 wt. % water surpassed conventional IL [BMIM][BF_4] in CO_2 sorption almost to the extent of typical organic amines that chemically complex to CO_2.[38] The research proposed a bicarbonate group being produced that captures the CO_2 whilst Maginn *et al.* countered this mechanism in one of his reports, instead putting forward an acetic acid formation.[39]

This led to the detailed study by Shiflett *et al.* who, using spectroscopic analysis, disputed Maginn's mechanism; they did report a slight smell of acetic acid during their experiments and so presumed it a lesser mechanism in the process. They conclude that the CO_2 is forming a very low vapour pressure molecular complex with the IL that is reversible, with barely any degradation of the IL.[40] The Shiflett group continued to publish evaluative data on the use of [BMIM][Ac] for CO_2 capture, claiming 16 % lower energy losses with the IL likened to MEA with 11 % cheaper investment and a

12 % reduction in equipment footprint.[41] They expanded the carboxylate functionalised ILs in their next paper reporting different absorptions of IL, 1-ethyl-3-methylimidazolium acetate [EMIM][Ac] to the triflouroacetate IL, [EMIM][TFA]. The [EMIM][Ac] showed the expected chemical absorption (far higher) than the [EMIM][TFA] which showed physical absorption only. There have also been computational studies on these acetate FILs that will be presented further on in Section 1.4.

A far more recent type of FIL is aprotic heterocyclic anions (AHAs) and these were first designed and synthesised by the Brennecke group in 2010. They reported high capacities, and viscosities that remain insensitive to change upon CO_2 sorption, with these AHA ILs.[42] The topic remains current to the group; exploring further the tuning of AHA ILs with electron-withdrawing and steric hindering substituents on the FILs, to change the enthalpy of CO_2 absorption.[43] ILs made up of $[P_{66614}]$ and super-base derived protic anions were reported in the same year by Wang *et al.* with the same promising advantages such as: equimolar CO_2 interaction, efficient capture and release, as well as relatively small changes in viscosities.[44] CO_2 is apparently reacting with the superbase-derived ILs to form a liquid carbamate type salt (Figure 1.8), which is proven by NMR and IR spectra.

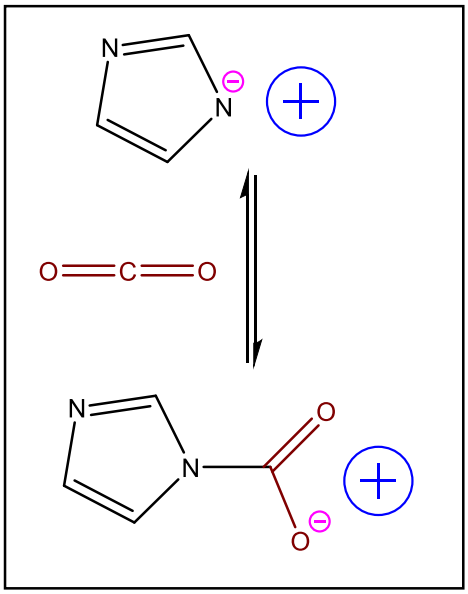

Figure 1.8. CO_2 reaction with imidazolide based FIL, the cation is simplified.

With two different research groups working on this class of functionalised ions, it is likely that a wide range of these AHA FILs will be presented shortly. However, whilst the lack of a large viscosity change is promising with these FILs, the starting viscosities are still too high to realistically be used in industrial applications.[8] Some examples of the AA functionalised ion structures along with the AHA/Superbase FILs are shown in Figure 1.9. Recently published work, by Wu and Maginn, shows the water solubility and CO_2 dynamics of some super-base ions with the tetrabutylphosphonium cation.[45]

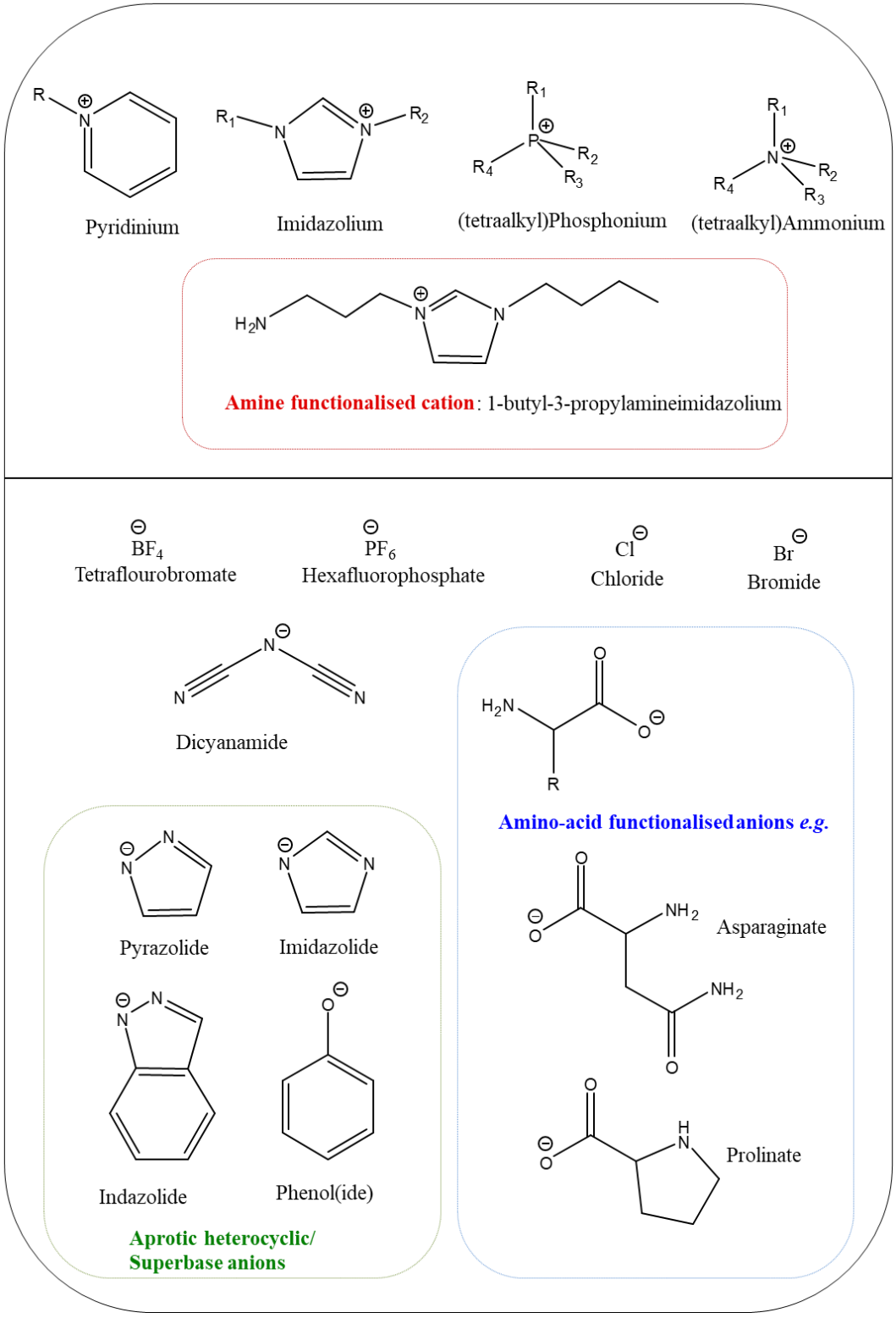

Figure 1.9. A summary of the typical cations and anions used in ionic liquids research; CO_2 capture task-specific/functionalised ions presented in groups. Drawn in ChemDraw.

1.3.4 Supported Ionic Liquid Membranes (SILMs)

As fluidity of solvents for CC in industrial processes is a concern, solid supported ILs are a possible solution for this. This was attempted to increase the absorption capacity as well as to tackle the problem of viscosity.[46] With ILs being relatively non-volatile the SILMs are thought to have a long usable lifetime with increasing contact area between gas molecules and the ILs [47], [48] (compared to bubbling gas through the IL/using conventional scrubbing methods).

These membranes can support conventional ILs or TSILs/FILs[49], [50] accommodating increased sorption capacities. Examples of porous supportive materials studied are polymeric materials,[51], [52] aluminium oxide (Al_2O_3),[53] and ceramic or zeolite materials.[54] Whilst the potential for industrial use is exciting, there are some drawbacks to the supported IL membranes, *e.g.* instability at pressurised and high temperature conditions[55] and thick membranes.[56], [57]

1.3.5 Polymerised Ionic Liquids

Polymeric ILs are a new type of functional polymer made with monomers that are IL cations and/or anions *e.g.* imidazolium and hexaflourophosphate. Tang *et al.* made the interesting discovery of an increased affinity (multiplied by 1.4-2.1) for CO_2 by polymeric ILs in comparison with conventional ILs.[58] An example of a polymeric IL they synthesised and tested is poly[(1-(4-vinylbenzyl)-3-butylimidazolium hexafluorophosphate] (PVBIH) and tetrafluorateborate (PVBIT).

In addition to the higher absorption capacity, they also reported a much faster rate of absorption and desorption (Figure 1.10). As a purely surface adsorption would achieve 0.0128 wt % sorption (by calculation), it is concluded that the bulk plays the most significant role in the sorption capacities of PILs making it an absorbing solid

material for CCS. The Tang group then published a mere 10 months after, the selective CO_2 sorption, over N_2 and O_2, of ammonium-based PILs and again indicating a bulk and surface sorption mechanism.[59]

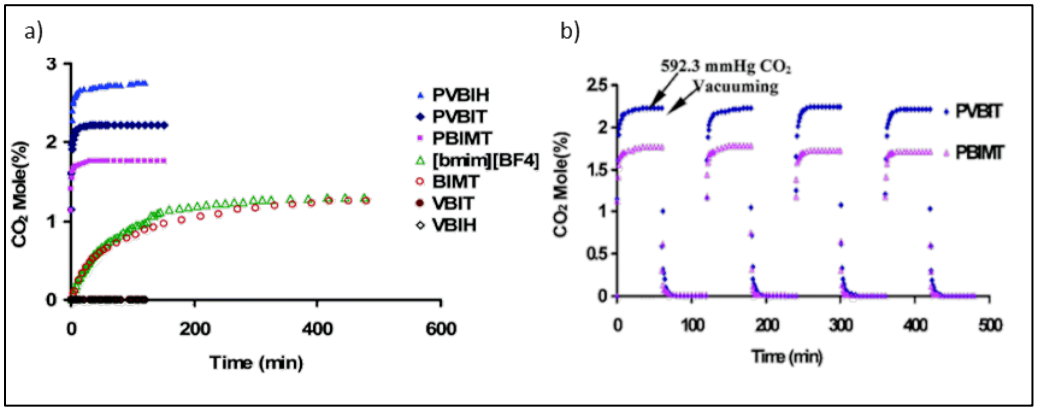

Figure 1.10. a) CO_2 capacity difference between polymeric ILs (top three curves) and typical ILs (bottom four). b) Fast rates of absorption and desorption (by vacuuming). Reproduced from reference [58] with permission from The Royal Society of Chemsitry.

1.3.6 Mixtures: IL/water, IL/amine and IL/super-base solutions

As ILs pose the dilemma of being a highly viscous medium, mainly after CO_2 uptake, that cannot be used in large scale industrial processes, a small adjustment can yield far better viscosities while maintaining high CO_2 sorption. A previously mentioned paper by Zhang *et al.*[31] reported the first AA IL for CO_2 absorption and noted the increased sorption with the presence of water. Contrarily, Ventura *et al.* studied CO_2 capture with a tri-iso-butyl(methyl)phosphonium tosylate/water system and reported that whilst there was a decrease in the viscosity there was also a decrease in the CO_2 absorption capacity.[60]

With conventional organic solvents, *e.g.* MEA, volatility and degradation properties are the main disadvantages for CC. On the other hand, ILs whilst non-volatile and

chemically/physically stable have viscosity as a problem for use in industrial use especially as there is an increase in viscosity after CO_2 capture. IL/MEA mixtures could be the answer to tackle both these problems.

Noble *et al.* were the first to propose and publish conventional ILs and amine solutions, where the solutions contained 50 mol % MEA, showing an increase in energy efficiency and rapid and reversible CO_2 sorption.[61] Due to the significant decrease in viscosity, these non-functionalised IL/MEA mixtures absorbed at a much faster rate than the cation functionalised ILs.[8], [29] The Zhang group[62], [63] have added at least 20 more mixtures of ILs and amines (*e.g. N*-methyldiethanolamine, MDEA) and/or water to their collection. One paper shows the addition of MDEA to $[N_{2222}][Gly]$ improves the CO_2 sorption rate and overall capacity.[62]

IL/super-base mixtures were initially studied before the super-base functionalised ILs were synthesised by the Wang group.[64] They combined an alcohol-functionalised IL with a super-base (a bicyclic amidine or a guanidine). It was established that the IL/super-base systems were highly efficient for CO_2 capture and release, with a nearly 1: 1 stoichiometry, and only a slight loss of activity is seen when recycled.

Ionic liquid mixtures are an interesting and viable option for industrial processes; low viscosity, low volatility, reasonable sorption capacities and easy regeneration are all greatly promising and possible.

1.4 Computational Modelling of Ionic Liquids

There are many vital questions regarding ILs that make molecular modelling the way forward, especially when exploring the microscopic structure. Molecular modelling has proved fundamental in the understanding of chemical structure and composition effect on the properties on the condensed phase.[65] In addition to this, simulations can result in predicted properties that are later proved experimentally. However, ILs present major challenges for computational researchers as ILs have a mix of strong intermolecular interactions over short and long distances. That being said the molecular simulation field is rather large and constantly being improved making it opportune timing for the exciting and novel complex fluids that are ILs to be studied and explored further.[66]

In recent years, detailed atomistic simulations - molecular dynamics, quantum mechanics (QM)/*ab initio* molecular dynamics (AI-MD), along with Monte Carlo and Coarse-Grained models of computational calculations on ionic liquids have been emerging around the research world. For precise electronic structure and the nature of bonding pre, during and after sorption, QM and AI-MD methods are used; simple classical potentials are too basic for specific electronic and atomistic details at a molecular level. A previously mentioned piece of research on AHA ILs was initialised with the use of AI calculations, important as it proved anion FILs were better at CO_2 absorption than cation FILs.[34] It is important to note computationally expensive QM methods are very much needed for deeper understanding of electronic structure and bonding. But for bulk properties, MD simulations are much more achievable in realistic time-frames.

As efficient and effective CO_2 capture and release is required of the ILs, MD plays an essential role in predicting and explaining the various chemical and physical properties of ILs. Properties such as thermal stability, solvation properties, density and viscosity are important to determine for realistic use of ILs in industrial processes.

A lot of the findings presented above in the conventional, and functionalised ILs sections are from MD and AI-MD calculations.

1.4.1 Molecular Dynamics (MD) of Ionic Liquids

Molecular Dynamics (MD) uses predefined force fields to compute the movement of a set of interacting particles, based on Newton's equation of motion. A simplistic algorithm followed in an MD simulation is shown in Figure 1.11. An incredibly powerful and widely-used tool, MD allows for long timescale simulations of large systems to be computed without being very computationally expensive, compared with quantum mechanical (QM) methods.

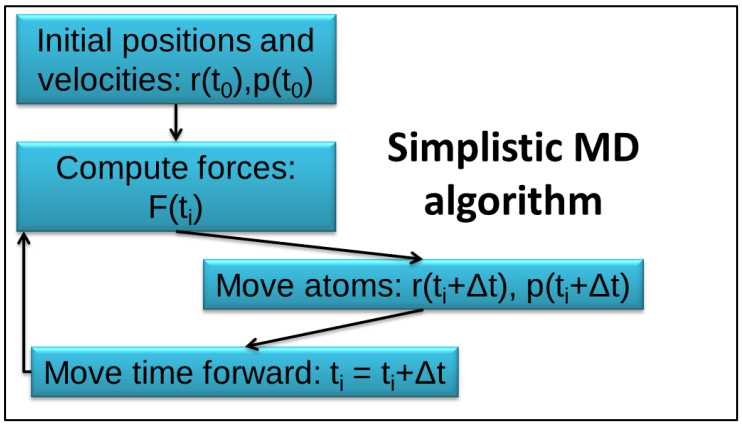

Figure 1.11. Simplification of the sequence of steps that occur in a typical molecular dynamics calculation where *r* is atom position, *p* is atom velocity, *t* is time, Δt is timestep and *F* is calculated forces.

Whilst molten salts have been computationally studied for at least half a century, the first step into IL simulations was only in the late 1990s and this was on tetraalkylammonium chloride which even having a melting point above 100°C was key early work leading to the simulating of actual ILs.[66] In 2001, the first research to have developed an MD potential and simulations on imidazolium ions was

published.[67] Hanke *et al.* described both the crystalline structure of [C1mim][Cl], [C1mim][PF_6], [C2mim][Cl] and [C2mim][PF_6] and the liquid structures of the dimethyl imidazolium salts. These liquid simulations were carried out applying an explicit atom and united atom potential; they concluded that the cheaper united atom potential was significantly poorer at modelling of the static solid and dynamic liquid simulations.[67] However, as computational methodology has developed it is obvious the simulations were probably not long enough (only 100 ps) to truly attain reliable self-diffusivities.[66] This same group (Lynden-Bell) simulated the solvation of small molecules in imidazolium based ILs.[68] They showed strong hydrogen bonding interactions between water/methanol for the [Cl] ion, and dimethyl ether/propane to the imidazolium based cations. These simulations were carried out at 400 K and were the first to simulate IL mixtures along with calculating the free energy of these systems.

A contending group in the IL and IL simulation field were the joint Brennecke and Maginn groups of University of Notre Dame. They published in 2002, the first Monte Carlo molecular simulation of [BMIM][PF_6], after developing a united atom FF using AI calculations and previous literature parameters.[69] Maginn's group too switched to an all-atom model for the potential finding a significant increase in the accuracy of the liquids densities (from 3-5% to 1% within the experimental data).[66], [70] Another finding of their paper was that there was long-range order evident in the liquid phase of the ionic liquid, as shown by radial distribution functions, RDFs (Figure 1.12). Molecular simulation studies were also done by other groups,[71]–[73] and overall these early studies were useful in giving an idea of how useful molecular simulations could be for accurately modelling ILs along with determining some challenging characteristics.

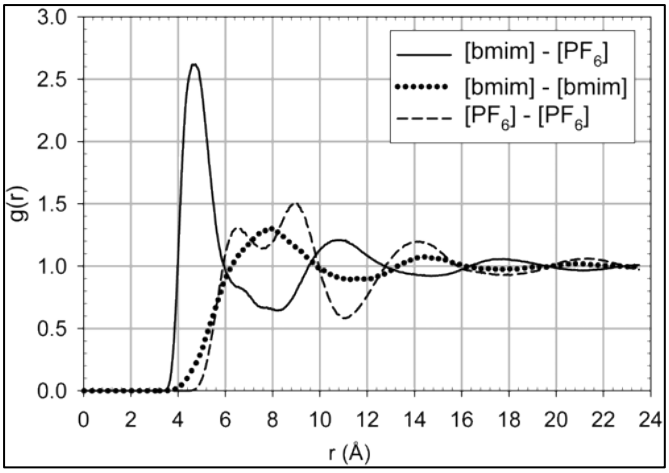

Figure 1.12. Centre of mass radial distribution functions (RDFs) of IL [bmim][PF_6] at 298 K. Maginn concluded the RDFs suggested that the ions were aggregating into well-defined ion clusters hence creating a long-range order. Taken with permission from [70]. Copyright 2002 American Chemical Society.

The most widely studied ILs by MD are imidazolium-based, *e.g.* by Wang *et al.*[73] who confirmed ab initio simulations[74] that placed anions close to the C2 carbon of the imidazolium, explained as being the most acidic site of the ring (between two nitrogen atoms). Figure 1.13 shows the depiction of the probability distribution that Wang *et al.* produced a very useful tool of analysing MD calculations.

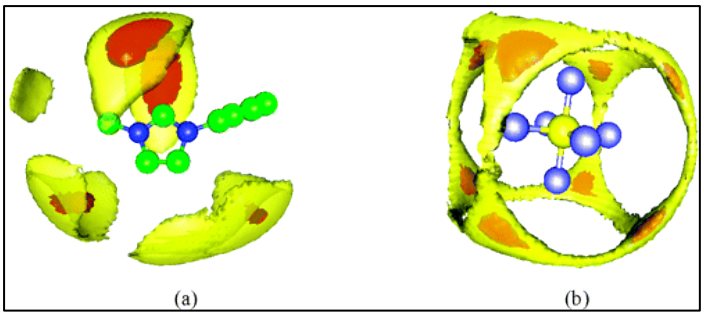

Figure 1.13. 3-D probability distributions of a) Cl^- around dimethylimidazolium and b) hexaflourophosphate. An extremely high probability (red) is seen at the C2 of the [Im] ion. Taken with permission from [73]. Copyright 2004 American Chemical Society.

MD has proven useful for characterising structural properties of ILs; Padua *et al.* simulated ionic liquids belonging to the imidazolium family of ions, and noted nano-structural organisations of the ions by polar and non-polar regions.[75] In another key computational study, Gutowski and Maginn have attributed slow translational and rotational dynamics, leading to a strong hydrogen-bonded network, for the dramatic increase in viscosity of the amine FILs using molecular dynamics simulations to make this conclusion.[37] A rather substantial piece of research, the estimates of self-diffusion coefficients and rotational time constants, as well as hydrogen bond analysis were consistent with the experimentally observed changes.

More recently, a publication that combined experimental work with MD simulations to study the CO_2 absorption with carboxylate anion FILs, is a good example of the advantages of using computational modelling to interpret the ability and mechanism of CO_2 sorption. Stevanovic *et al.* determined that CO_2 solvated preferentially in the non-polar domain of the IL 1-butyl-1-methylpyrrolidinium acetate, $[C_1C_4Pyrro][OAc]$.[76] Even the shortcomings of MD were helpful in reinforcing the conclusion that the high CO_2 solubility of $[C_1C_4Pyrro][OAc]$ (instead of the IL with the triflouroacetate anion) was due to a chemical reaction. This is due to the inability to the reproduce experimental solubility of the [OAc] IL whilst correctly predicting the solubility of the [TFA] IL.

Finally, there is great opportunity for the development and use of Monte Carlo simulation methods when modelling ionic liquids. E.J. Maginn claimed that as Monte Carlo simulations are important for overcoming the inherent “sluggish dynamics”, the field was “ripe for future development”.[66]

1.5 Summary

As evident from the introduction and literature review presented here, IL research is gaining momentum, with computational modelling being key in both providing new insights into the features and improving our understanding of ionic liquids. The field is evolving quickly and with such a large database of IL ions to choose from, the possibilities for study is practically endless.

To this end, the next chapter will provide detail into the methods used for this body of work, describing the MD theory implemented in the running and analysis of simulations, along with the interatomic potentials utilised.

The first research chapter, Chapter 3, of this thesis will look at validating and comparing two force fields for molecular dynamics modelling of ILs. This is an important initial step in this body of work, before attempting to tackle the simulations of ILs of interest.

Following on from this, the second research chapter details the calculations and analysis carried out on a traditional IL: Trihexyltetradecylphosphonium bis(trifluoromethylsulfonyl)imide, $[P_{66614}][NTf_2]$, using the FF selected from the first research chapter's work.

Finally, MD simulations of $[P_{66614}][NTf_2]$ with different loadings of carbon dioxide were calculated and the analysis of this is presented in Chapter 5. The presentation of on-going and future work is presented with some concluding remarks in Chapter 6.

Chapter 2

Computational Theory and Methodology

In this chapter, we describe the theory and methodology adopted to obtain the results of this study. To investigate our system, we have used the molecular dynamics computer simulation method to study the physical movements of atoms and ions in our systems. Interatomic potentials are implemented to be able to reproduce the bulk properties and structure of liquids. Molecular dynamics packages, Amber and DL_POLY, were utilised for calculations.

2.1 Molecular Dynamics

Molecular Dynamics (MD) uses predefined force fields to compute the movement of a set of interacting particles, based on Newton's equations of motion. It is a technique used to study the time evolution of interacting particles.[77], [78] A typical algorithm followed in an MD simulation is shown in Figure 2.1. An incredibly powerful and widely-used tool, MD allows for long timescale simulations of large systems to be computed without heavy computational expense, compared with quantum mechanical (QM) methods.[79]

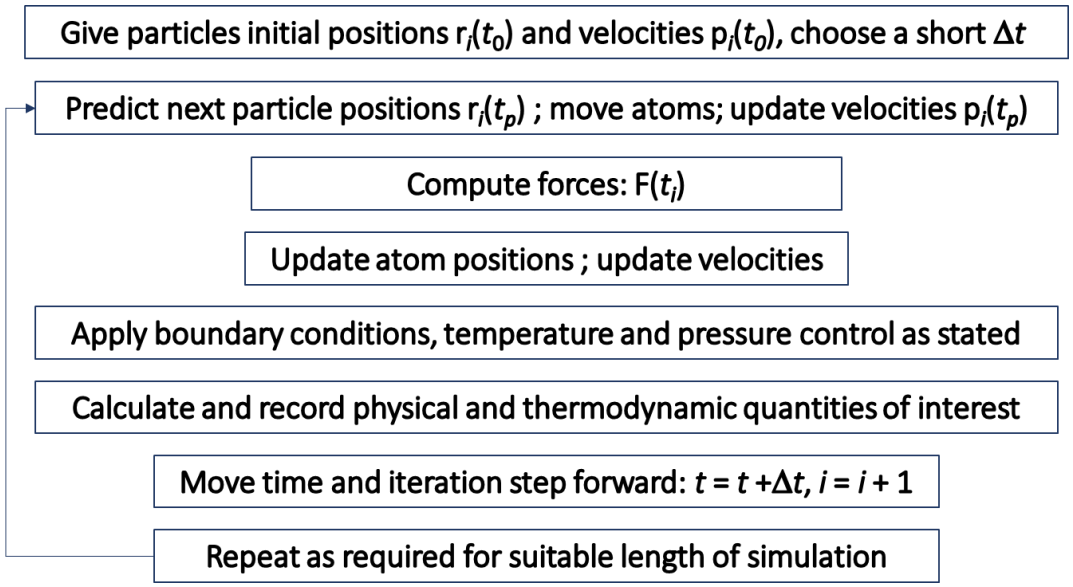

Figure 2.1. Sequence of steps that occur in a typical molecular dynamics calculation.

From classical mechanics, Newton's second law of motion forms the base of the motion of classical particles:

$$\boldsymbol{F}_i = m_i \boldsymbol{a}_i \tag{2.1}$$

The mass of the particle is m_i, its acceleration is $\boldsymbol{a}_i$, and $\boldsymbol{F}_i$ is the force acting upon it due to interaction with other species and any external stimuli. This assumption is valid for the motion of non-light atoms, whilst vibrations with frequencies (ν) fulfil $h\nu > k_B T$. This relationship is true at high temperatures.

Another assumption employed in MD simulations is that no electrons are explicitly included. The interaction between particles is computed by a potential energy function. This assumption is reliant on the applied force-field models employed to account for the intra- and inter-molecular interactions between particles. Essentially, the accuracy and suitability of the simulation is based on the interatomic force-field selected. The molecular mechanics and interatomic potentials are described in detail in Section 2.2.

2.1.1 Total Energy Conservation

A system's total energy (*E*) is said to be conserved over time, *i.e.* energy cannot be created or destroyed. *E* can be written as the sum of the system's kinetic (*K*) and potential (*V*) energies.

$$E = K + V \tag{2.2}$$

It is assumed that these parts are time independent, and the total energy is a constant of motion. Consequently, no time-independent or velocity-dependent forces may act on the system. Finally, in MD simulations where N interacting particles are in a system, the particles follow Newton's equations of motion and conserve energy, *E*.

2.1.2 Integrating Newton's Equation of Motion

For a classical particle with mass *m* that is moving under the influence of a force **F**(r)

$$m\frac{d^2\boldsymbol{r}}{dt^2} = \mathbf{F}(\mathrm{r}) \tag{2.3}$$

and the classical equations of motion are expressed through equations 2.4.

$$\frac{d\mathbf{r}(t)}{dt} = \frac{\mathbf{p}(t)}{m} = \mathbf{v}(t) \tag{2.4a}$$

$$\frac{d\mathbf{p}(t)}{dt} = \mathbf{F}(\mathbf{r}) \tag{2.4b}$$

$$\frac{d\mathbf{v}(t)}{dt} = \frac{\mathbf{F}(t)}{m} \tag{2.4c}$$

p is the particle's momentum (**p**=*m***v**(*t*); **v**(*t*) is the particle's velocity), and *t* is time. To define the particle trajectory dependent on the external force-field **F**(**r**), we need to integrate the equations 2.4*a*-*c*, giving the position **r**(t), and momentum **p**(t) at each time.

For a moving particle that is under a constant force, such that **F**(r) = *F*, the evolution of a particle's momentum and position with time is given by:

$$\mathbf{p}(t) = Ft + \mathbf{p}_0 \tag{2.5a}$$

$$\mathbf{r}(t) = \frac{1}{2}\frac{F}{m}t^2 + \frac{\mathbf{p}_0}{m}t + \mathbf{r}_0 \tag{2.5b}$$

where $\mathbf{r}_0$ and $\mathbf{p}_0$ are the particle's initial position and momentum. Thus, the knowledge of these initial terms is what defines the particle's trajectory.

Realistically, a simulation is a system of *N* interacting particles where the force acting on a particle changes with changing particle position, *i.e.* the force is the gradient of the potential $\mathbf{F} = -\nabla V(r_1, r_2, \ldots, r_N)$. To describe the motion of *N* interacting particles, a set of *N* equations are used

$$m\frac{d^2\boldsymbol{r}}{dt^2} = \mathbf{F}_{\boldsymbol{i}}(\boldsymbol{r}_1, \boldsymbol{r}_2, \ldots, \boldsymbol{r}_N), i = 1, N \tag{2.6}$$

with the equations of motion for each of the *N* particles being

$$m\frac{d\boldsymbol{r}_i}{dt} = \frac{\mathbf{p}_i}{m} \tag{2.7a}$$

$$\frac{d\mathbf{p}_i}{dt} = \mathbf{F}_i \qquad (2.7b)$$

The force acting on the particles has a complicated form and thus equation 2.7 cannot be analytically solved. Instead, to solve these differential equations, a finite difference approach is utilised by breaking down the calculation into short time steps (Δt). At every time step, the forces acting on the particles is calculated and then combined with the current positions and velocities to yield new positions and velocities. Then the particle is moved to the new position and the forces are recalculated. The force acting on a particle is assumed to be constant during each time step. This procedure is repeated for a set simulation time to generate a dynamical trajectory, which is describing the time evolution of $\mathbf{p}_i$ and $\mathbf{r}_i$ for each particle on a time grid

$$\{\mathbf{r}_i(t_0), \mathbf{r}_i(t_0 + \Delta t), \mathbf{r}_i(t_0 + 2\Delta t), \dots\} \qquad (2.8a)$$

$$\{\mathbf{p}_i(t_0), \mathbf{p}_i(t_0 + \Delta t), \mathbf{p}_i(t_0 + 2\Delta t), \dots\} \qquad (2.8b)$$

Therefore, MD computes the microscopic dynamics of a system, in terms of a trajectory for each individual particle in the system. MD is a deterministic technique; with the initial set of positions and momenta, you can completely define the time evolution. Additionally, the configuration of the interacting particles at each time *t* is completely defined by

$$\{\mathbf{x}_1(t), \mathbf{x}_2(t), \dots, \mathbf{x}_N(t)\} \qquad (2.9)$$

where $\mathbf{x}_i = (\mathbf{r}_i, \mathbf{p}_i)$ and defines the position and momentum of particle *i*.

2.1.3 Finite Difference Methods

As MD simulations require time integration algorithms to integrate the equations of motion to obtain trajectories, a number of these have been developed. When choosing an integration algorithm some key considerations need to be made: it is

important that the algorithm be computationally efficient; preserve energy and momentum of the system; and allow the utilisation of adequately long-time steps for integration.

2.1.3.1 The Verlet algorithm

For one set of N particles, with positions **r**(*t*), the positions a small-time step later **r**(*t*+Δt), are given by a Taylor expansion about **r**(*t*):

$$\mathbf{r}(t+\Delta t) = \mathbf{r}(t) + \mathbf{v}(t)\Delta t + \frac{1}{2}\mathbf{a}(t)\Delta t^2 + \frac{1}{6}\mathbf{b}(t)\Delta t^3 + O(\Delta t^4) \qquad (2.10a)$$

The velocities **v**(t) are the first derivatives of the positions **r**(*t*), the accelerations **a**(*t*) are the second derivatives of **r**(*t*) and the hyperaccelerations **b**(*t*) are the third derivatives etc. $O(\Delta t^4)$ is the truncation error of the algorithm.

The positions, at a small-time step earlier r(*t*-Δt) are:

$$\mathbf{r}(t-\Delta t) = \mathbf{r}(t) - \mathbf{v}(t)\Delta t + \frac{1}{2}\mathbf{a}(t)\Delta t^2 - \frac{1}{6}\mathbf{b}(t)\Delta t^3 + O(\Delta t^4) \qquad (2.10b)$$

Adding equation 2.10a and 2.10b together, we obtain the basic form of the Verlet algorithm, which allows us to solve Newton's equation numerically:

$$\mathbf{r}(t+\Delta t) = 2\mathbf{r}(t) - \mathbf{r}(\mathrm{t}-\Delta t) + \mathbf{a}(t)\Delta t^2 + O(\Delta t^4) \qquad (2.11)$$

a(*t*) is the force divided by the mass, and the force is a function of **r**(*t*):

$$\mathbf{a}(t) = -\frac{1}{m}\mathbf{F} = -\frac{1}{m}\nabla_{\mathrm{r}}\, V(\mathrm{r}_1, \mathrm{r}_2, \ldots, \mathrm{r}_N) \qquad (2.12)$$

Consequently, with only the knowledge of the particles current position, last position and current acceleration, we can solve for the position of the particle a time step Δt into the future. It is noted that the velocities are not directly calculated, which is useful for the estimating of the kinetic energy, *K*. The velocity is obtained from:

$$\mathbf{v}(t) = \frac{\mathbf{r}(t + \Delta t) - \mathbf{r}(t - \Delta t)}{2\Delta t} \tag{2.13}$$

Thus, the basic form of the Verlet algorithm does not handle the velocities with the same accuracy as the particle positions are treated with; equation 2.13, $O(\Delta t^2)$ and equation 2.11, $O(\Delta t^4)$.

2.1.3.2 The Verlet Leapfrog algorithm

The lack of explicit velocities along with the numerical errors can be remedied by the Leapfrog algorithm. [80] Here the Taylor's expansions are calculated at half time steps for the velocities and not at the same time as positions. Whilst this corrects the numerical accuracy, it is impossible to obtain the total energy of the system at the current time step; the kinetic and potential energies are not calculated at the same time. Instead the total energy comes from an average value over a given time interval.

2.1.3.3 The Velocity Verlet algorithm

Lastly, the velocity Verlet algorithm was introduced as an improvement of the basic Verlet and Leapfrog algorithms. Now, the positions, velocities and accelerations are computed at the same time.

$$\mathbf{r}(t + \Delta t) = \mathbf{r}(t) + \mathbf{v}(t)\Delta t + \frac{1}{2}\mathbf{a}(t)\Delta t^2 \tag{2.14a}$$

$$\mathbf{v}(t + \Delta t/2) = \mathbf{v}(t)\Delta t + \frac{1}{2}\mathbf{a}(t)\Delta t \tag{2.14b}$$

$$\mathbf{a}(t + \Delta t) = -\frac{1}{m}\nabla_{\mathrm{r}} V\left(\mathbf{r}(t + \Delta t)\right) \tag{2.14c}$$

$$\mathbf{v}(t + \Delta t) = \mathbf{v}(t + \Delta t/2) + \frac{1}{2}\mathbf{a}(t + \Delta t)\Delta t \tag{2.14d}$$

Equation 2.14*b* describes the half-step velocities that are used to advance particle positions by a full timestep. This means less memory is required and greater computational efficiency is achieved compared to the basic Verlet algorithm, whilst generating identical trajectories and properties and removing the phase shift abnormalities of the Leapfrog algorithm. Significantly, it is clear from the above that the choice of time-step is crucial. The chosen time-step cannot be too small as only a portion of the trajectory will be sampled; the time-step cannot be too large as this may lead to instabilities in the integration algorithm because of high energy overlaps between particles. It should be noted that, for all simulations presented in this thesis, the velocity Verlet algorithm was implemented.

2.1.4 Ensembles

A statistical ensemble is a finite collection of all possible systems that have different microscopic states but the same thermodynamic state. The simplest ensemble is the microcanonical one, *i.e. NVE* ensemble, in which the number of particles (*N*), the cell volume (*V*) and the total energy (*E*) are conserved. However, this ensemble does not represent the majority of real systems; temperature and pressure are required for more realistic simulations. These ensembles are the *NVT* and *NPT* ensembles that are described below. There is also a forth ensemble, the grand-canonical ensemble (μVT), which represents a system that is open, as energy and particles can be exchanged with a reservoir, whilst the chemical potential (μ) is kept fixed.

2.1.4.1 Canonical Ensemble

In the canonical ensemble, usually referred to as the *NVT* ensemble, along with *N* and *V*, temperature *T* is kept constant. The energy of endothermic and exothermic

processes is exchanged with a thermostat, that adds or removes energy to the system to maintain the temperature around a specified average.

2.1.4.2 Isobaric-Isothermal ensemble

In this ensemble, temperature, pressure and number of particles is kept constant (*NPT*). This is an extension of the canonical ensemble and is the most commonly employed ensemble, as chemical reactions are typically carried out under constant pressure conditions. There are two methods typically utilised to maintain this ensemble: a weak coupling to an external pressure bath – the Berendsen barostat;[81] or *via* the addition of an extra degree of freedom to the Hamiltonian – the Parrinello-Rahman barostat.[82]

Berendsen Barostat and Thermostat

Berendsen *et al.*[81] developed a simple thermostat, where a hypothetical external heat bath of a fixed temperature is coupled to the simulation cell. The practical inference of this is frequent collisions of the simulated particles with light particles forming an ideal gas at the fixed temperature. This is attained by introducing a velocity scaling factor (λ), with a value of λ such that the change of temperature with time is proportional to the temperature difference between external bath and simulation cell.

$$\frac{dT(t)}{dt} = \frac{1}{\tau}\left(T_0 - T(t)\right) \tag{2.15}$$

The barostat also maintains the pressure of the system by a weak coupling of the system to an external pressure bath. The principle of least local perturbation is used to do this.

Once again, it should be noted here that the *NPT* ensemble was used for all MD simulations in this body of work, specifically the implementing the Berendsen barostat

and thermostat. There is another barostat and thermostat available such as the Nose-Hoover; where an additional degree of freedom in the determination of E accounts for the effect of the external bath on the system.[83]

2.1.5 System Size and Periodic Boundary Conditions

It is important that the system size chosen for these simulations is a balance between: explicitly representing a large enough system of the particles in bulk, and the size and computational cost of the simulation. Thus, an approach to minimise the computational cost of simulations of bulk periodic structures is to utilise periodic boundary conditions (PBC). Essentially, PBC allows for a finite system to imitate an infinite system. Without PBC, the simulation box would be depictive of a cluster of particles, enclosed by surfaces. Instead, to model realistic bulk materials, the simulation box is replicated through space, forming an infinite lattice by rigid translation in all three (x, y, z) Cartesian directions. In other words, the total simulation box is made up of the central unit cell in a supercell. Using PBC, if a particle is moving out of the unit cell, an identical particle replaces this at the opposite face of the cell. Effectively, the number of particles within the unit cell is conserved, and no particle feels any surface forces, as the surface of the cells are removed by the existence of the adjacent periodic cells. Figure 2.2 depicts PBC in a graphical representation.

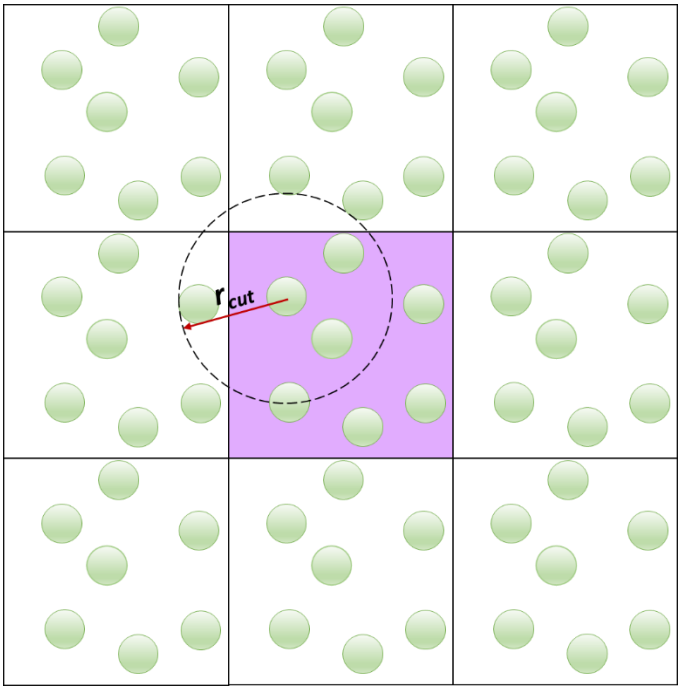

Figure 2.2. Graphical representation of periodic boundary conditions. Centre purple box is the simulation box, and the white boxes are the periodic images of this. Green filled circles are particles and r_{cut} is the cut-off radius – this distance is the limit of interaction. The simulation box does not have to be cubic; however, simple cubic PBC has been utilised here for ease of visualisation and was implemented in the simulations of this thesis.

Another important point is that in an MD simulation, a particle may interact with another particle in a neighbouring cell (which is an image of a particle within the unit cell), if it is within the cut-off radius, labelled r_{cut} in Figure 2.2. It will then ignore the equivalent particle in the simulation box as it is too far away. In other cases, the interaction comes from a particle in the simulation cell itself. This is known as the minimum image convention, as the interaction is always calculated with the closest image. Thus, the rule is that r_{cut} cannot be larger than the half width of the simulation cell, *i.e.* $2r_{cut} < L_{box}$, to ensure that the cut-off radius only allows a particle to interact with one image of any given atom.

2.2 Molecular Mechanics and Interatomic Potentials

Quantum mechanical calculations offer a rigorous description of the molecule modelled from both a structural and electronic point of view.[79] MD, as opposed to such AI techniques, is based on empirical observations of interatomic interactions. In the case of MD, the nuclear motion is considered while implying a fixed electron distribution associated with each atom, *i.e.* a charge. Thus, a model has been developed where molecules are represented as a collection of spheres joined together by springs. Therefore, classical physics and simple potential energy functions can be used, and large systems and long simulation times can be computed, with MD runs that result in good statistical data.

Bonding information must therefore be provided rather than being assigned as a result of solving the electronic Schrodinger's equation. This information is contained within a force field; it is composed of bonded and non-bonded interactions. The sum of the bonded and non-bonded interactions for a single particle yields the total energy, with the negative differential of that total energy with respect to particle position returning the force on that particle.

$$U_{total} = U_b + U_\theta + U_d + U_{id} + U_{nb} \tag{2.16}$$

where $U_b + U_\theta + U_d + U_{id}$ are the bonded terms; specifically, the bond, angle, proper and improper dihedral functions, *i.e.* the intramolecular terms. U_{nb} is the non-bonded term made up of intermolecular interactions, namely the electrostatic and van der Waals interactions.

2.2.1 Bonded Interactions

Bonded interactions are described by the bonded terms of a force field, and is made up of the bonds, angles and dihedral energies.

2.2.1.1 Two Body Harmonic Bond Stretching Potential

A simple harmonic oscillator approximation is applied when considering the bond between two particles. The potential energy of bond stretching is described by:

$$U_b(\mathbf{r}) = \frac{1}{2}k_b(r - r_0)^2 \tag{2.17}$$

where k_b is a harmonic spring constant between the two particles and where r is the bond length and r_0 is an ideal bond length such that $(r - r_0)^2$ is the squared distance of bond length from the ideal value.

2.2.1.2 Three Body Harmonic Angle Bending Potential

The three-body angular bond potential describes the angular vibrational motion occurring between three atoms and is traditionally treated the same way as a bond length, described by a harmonic bending potential.

$$U_\theta(\mathbf{r}) = \frac{1}{2}k_\theta(\theta - \theta_0)^2 \tag{2.18}$$

where k_θ is a harmonic spring constant, the current angle is θ and θ_0 is the ideal angle such that the potential energy increases as the angle deviates from that ideal.

2.2.1.3 Four Body Dihedral Angle Potentials

The harmonic description is only valid for small deformations - 2 and 3-body terms only; dihedral terms are required to describe the 4 body terms present in molecules of more than 3 atomic spheres.

For the torsional potential, a periodic function provides a better description:

$$U_{\Phi}(\mathbf{r}) = k_{\Phi}[1 + \cos(m\Phi - \delta_0)] \tag{2.19}$$

Where k_{Φ} is a force constant proportional to the barrier to rotation, m is the periodicity – indicating the number of minima in the function and δ is a phase angle that determines which torsional angle Φ that corresponds to a minimum (the optimum value). A depiction of a proper dihedral angle is in Figure 2.3.

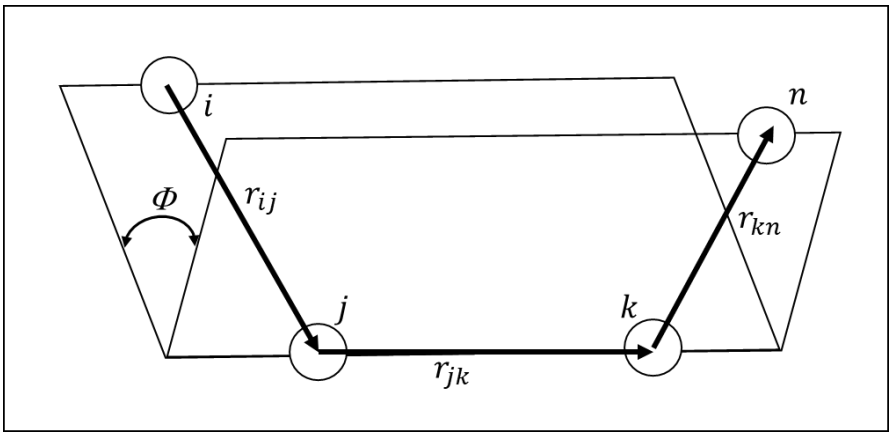

Figure 2.3. A graphical representation of a proper dihedral angle, with associated vectors. Adapted from reference [84].

Whilst a proper dihedral follows the sequence of 4 atoms in a single line, $i - j - k - n$, in Figure 2.3, an improper torsional angle lies between the plane containing atoms $i - j - k$ and atoms $j - k - n$, shown in Figure 2.4.

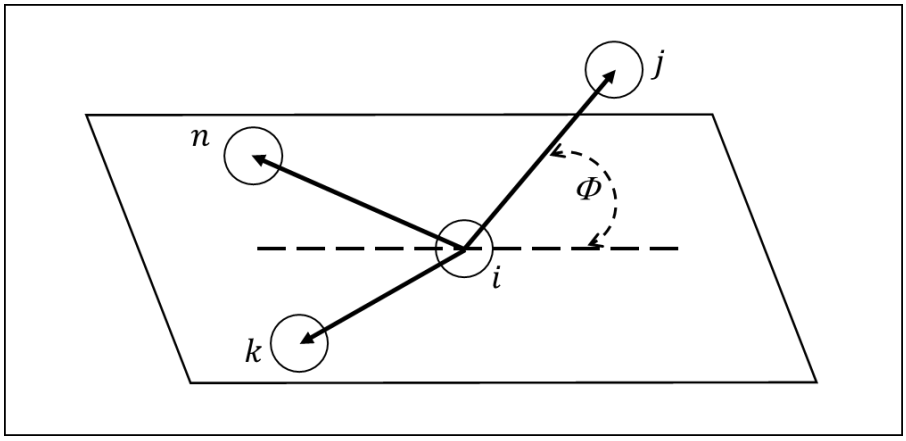

Figure 2.4. A graphical representation of an improper dihedral angle, with associated vectors.

Improper torsional angles are used to maintain planar groups such as carbon rings, and chirality on a tetrahedral group, ensuring that structures do not flip or pucker. Here, a harmonic potential may be used:

$$U_{\Phi}(\mathbf{r}) = \frac{1}{2} k_{\Phi}(\Phi - \Phi_0)^2 \tag{2.20}$$

2.2.2 Non-Bonded Interactions

For interactions that are not defined by the connectivity of bonds in the molecules, the terms are instead dependent on the distance between particles or atoms. These interactions can be considered to consist of two parts: Van der Waals and electrostatic or coulombic interactions.

2.2.2.1 Van der Waals Interactions

Often referred to as the combination of attractive and repulsive forces between two non-bonded atoms, the interaction can be described by the simple 6-12, also called

Lennard-Jones (L-J), the Born-Huggins-Mayer or a Buckingham potential,[85] to name a few. Most commonly used, despite the relative simplicity is the 6-12 Lennard-Jones potential that does not require the calculating of large numbers of square roots and exponentials. It depends only on two parameters and is expressed as:

$$U_{LJ}(\mathbf{r}) = 4\epsilon_{ij}\left[\left(\frac{\sigma_{ij}}{r_{ij}}\right)^{12} - \left(\frac{\sigma_{ij}}{r_{ij}}\right)^{6}\right] \tag{2.21}$$

where ϵ_{ij} is the minimum of the potential of the interaction between atoms i and j, σ_{ij} the collision diameter (the separation at which the energy is zero) and r_{ij} is the separation distance. London dispersion-attraction forces are mediated by the r^{-6} term, whilst short range repulsions are accounted for by the r^{-12} term. At short distances the repulsive term dominates this potential. As the distance increases the potential goes to zero, so typically a cut-off distance is used to shorten the potential to zero quicker, making the calculation more computationally efficient.

2.2.2.2 Electrostatic Interactions

Atoms that are highly electronegative attract electrons more than less electronegative atoms, and this gives rise to an uneven distribution of the charge in a molecule. The electrostatic interactions are usually calculated using partial charges on the atom centres with the energy calculated using Coulomb's law:

$$U_{el}(\mathbf{r}) = \sum \frac{q_i q_j}{D r_{ij}} \tag{2.22}$$

where q_i and q_j are the charges of atoms i and j, separated by distance r_{ij}, and D equates to:

$$D = 4\pi\epsilon_0 \tag{2.23}$$

ϵ_0 is the free space permittivity. The electrostatic term becomes less accurate for highly polarisable ions or groups, and this is when polarisable force-fields would be required.

2.2.2.2.1 Ewald Summation

Direct calculation of the coulombic equation for an infinite number of atoms where the interactions increase with distance proves to be impractical, leading to slow convergence and long calculation times. Ewald proposed a solution for this named the Ewald Summation,[86] where the Coulombic term is rewritten as a sum of two convergent parts. A short-range contribution is calculated in real space, whilst a long-range contribution is calculated in reciprocal space (using a Fourier transform).

$$E_{el} = E_{real} + E_{reciprocal} + E_{self} \tag{2.24}$$

E_{self} is the self-energy, a correction term that cancels out the self-interactions of the artificial counter charges. Consequentially, use of the Ewald summation method is restricted to systems that are charge neutral and with a dipole moment of zero.

The smooth particle mesh Ewald (SPME)[87] is a commonly used algorithm that requires less computational time and memory than the original Ewald method. Here, the interaction potential is divided into two terms. Additionally, the summation of point particle interaction energies is altered to two summations.

The particle contribution of SPME is:

$$E_{short-range} = \sum_{i,j} \varphi_{short-range}\left(r_j - r_i\right) \tag{2.25}$$

The Fourier transform summation is:

$$E_{long-range} = \sum_{i,j} \widetilde{\Phi}_{long-range}\left(\boldsymbol{k}\right)|\tilde{\rho}(\boldsymbol{k})|^2 \tag{2.26}$$

where the $\tilde{\rho}(\boldsymbol{k})$ is calculated with a fast Fourier transform on a mesh (discrete lattice). The energy function is smooth so that the derivative of it is analytically calculated. Hence, the name smooth particle mesh Ewald. The SPME method is utilised by DL_POLY, and is restricted to periodic systems only, *i.e.* requiring the use of PBC.

2.2.3 Summary of Interatomic Potentials

The complete force field equation, in terms implemented by the forcefields utilised in this thesis is:

$$
\begin{aligned}
&U(\mathbf{r}) \\
&= \sum_{bonds} \frac{1}{2} k_b (r - r_0)^2 + \sum_{angles} \frac{1}{2} k_\theta (\theta - \theta_0)^2 + \sum_{dihedrals} k_\Phi [1 + \cos(m\Phi - \delta_0)] \\
&+ \sum_{\substack{improper \\ dihedrals}} \frac{1}{2} k_\Phi (\Phi - \Phi_0)^2 \\
&+ \sum_{non-bonded}^{i} \sum_{interactions}^{j \neq i} \left\{ 4\epsilon_{ij} \left[\left(\frac{\sigma_{ij}}{r_{ij}} \right)^{12} - \left(\frac{\sigma_{ij}}{r_{ij}} \right)^{6} \right] + \frac{1}{4\pi\epsilon_0} \frac{q_i q_j}{r_{ij}} \right\}
\end{aligned}
\tag{2.27}
$$

2.2.4 Force Field Parameterisation

The short-comings of non-specific or “off-the-shelf” FFs is the inability to accurately describe the complex liquids; a purely organic or inorganic FF would fall short. Parameterisation or refinement of a force field is required for the accurate simulation of specific materials. This can be done in two ways: obtaining a simultaneous best fit of calculated results against experimental data, with the use of least-squares

optimisation methods; or a trial and error procedure with AI calculations, where small changes are made to the parameters to achieve the best possible fit. [79]

Whilst ILs share part of their molecular structures with molecules that have been parameterised in existing FFs (OPLS, AMBER, CHARMM etc), their ionic character arising from their electrostatic charges need to be included. The first - currently, one of the most widely-used [88], [89] – FFs parameterised for ILs is called the CL&P force-field (after creators Canongia Lopes and Padua) and was first developed in 2005 as a systematic all-atom force field, based on the OPLS-AA/AMBER force fields [90]. Whilst many short-range parameters were found in the OPLS-AA/AMBER framework, ab initio calculations were used to calculate charge parameters, equilibrium bond lengths and angles.

Key features in the parameterisation were the flexibility of the ions and the atomic point-charge distributions, whilst the L-J, bond and angle parameters were easily transferred. The Coulombic parameters are determined from calculations of the electron density at the MP2 theoretical level, with large basis sets. The atomic charges (from the electron density) are then optimised to reproduce the electrostatic field generated by the ion. The flexibility of the ions is accurately described by fitting torsional energy profiles for parameterisations against *ab initio* calculations.

2.2.5 Force Fields (FFs) for Ionic Liquids MD

Succeeding the primitive FFs used in the initial simulations of ILs (described in Chapter 1, Section 1.4.1,[64]–[70]) there are now FFs specifically designed for MD simulations of ILs. The CL&P FF has many advantages; including an extensible FF that is backwardly compatible with previously parameterised systems. Continuous growth of the FF is reported – originally there were only dialkylimidazolium cations with different anions, *e.g.* triflate and bistraflamide,[91] bromide and dicyanamide.

The FF now includes non-imidazolium cations such as, pyridinium and phosphonium. [92] The group have 5 publications and over 20 ions parameterised; the most recent paper [93] in 2010 added another 6 ions consequently creating a large variety of ionic liquids that could be simulated (Figure 2.5).

Cations		Anions	
Imidazolium		Chloride, Bromide [2,3,9]	Cl^- Br^-
…1,3-dialkyl [2,3]		Triflate [8]	$CF_3SO_3^-$
…1-alkyl [9]		Bis(sulfonyl)imide	
…1,2,3-trialkyl [10]	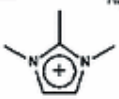	…bis(trifluoromethyl) [8]	$(CF_3SO_2)_2N^-$
…functionalized [10,11]	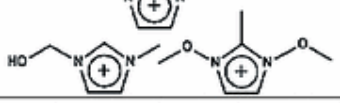	…bis(fluoro) [11]	$(FSO_2)_2N^-$
		…bis(perfluoroalkyl) [11]	$(C_nF_{2n+1}SO_2)_2N^-$
N-alkylpyridinium [9]	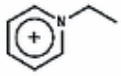	Alkylsulfates [10]	$C_nH_{2n+1}SO_4^-$
Ammonium		Alkylsulfonates [10]	$C_nH_{2n+1}SO_3^-$
…Tri-, tetra-alkyl [8]		Phosphate	
…*N*,*N*-pyrrolidinium [8]	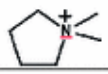	…hexafluoro [2,3,8]	PF_6^-
		…trifluorotrifluoroalkyl [11]	$PF_3(C_nF_{2n+1})_3^-$
Tetralkylphosphonium [9]		Nitrate [2,3,8], Dicyanamide [9]	NO_3^- $N(CN)_2^-$

Figure 2.5. Summary list of ionic liquid ions modelled by the CL&P FF by the end of 2010. Image reproduced with permission from [88]. Copyright 2012 by Springer Theoretical Chemistry Accounts.

Within the creators' groups the CL&P FF has been used for simulations of many ionic liquids, some including carbon dioxide simulations.[76], [94] Around the world research has been done using the CL&P FF.[89], [95] In recent years, Chaban and Prezhdo [96] used the CL&P FF to simulate ILs to efficiently and accurately predict properties such as density and self-diffusion coefficients.

A contending large group on FF development for ILs with CO_2 is the Wang group, who around the same time published their FF closely based on the AMBER FF. [73] They too reported better densities, compared with experimental data, with their FF

than other FFs and the Wang FF is being used by other groups.[97] The CL&P and Wang FF are examples of all-atom non-polarised FFs. In addition to these, in the recent years, a united-atom FF was proposed by Ludwig *et al.* [98] and they reported all simulated properties to be in excellent agreement with experimental work, whilst being 100% faster to simulate. Coarse-grained simulations were also reported (in 2013) by Laaksonen *et al.* [99] where they showed good agreement of RDFs simulated with effective pair potentials to atomistic simulations, but emphasised the need to use explicit long-range interactions to improve the reliability of thermodynamic, scattering and dynamic properties.

2.2.6 Polarisable Force Fields

Whilst the above methods are all worthwhile mentions, there has been increasing debate over the need for polarised FF for ionic liquids simulations as even CL&PFF had been reported to give a poor description of the dynamics of ILs (whilst giving good representations of the static properties) [100]. An electronically polarisable model was first developed by Voth *et al* [101] in 2004 and whilst the computational expense is increased, the ions are more mobile hence significantly improving the agreement of dynamic properties between simulation and experiment. Other researchers have also started developing polarised FFs for ILs, *e.g.* Borodin, in 2009, tested the FF for a large range of ILs before publishing a paper reporting good dynamical properties. [102] The work they presented is to be part of their own Atomistic Polarisable Potential for Liquids, Electrolytes & Polymers (APPLE&P). They claim that the MD simulations performed on 30 ionic liquids predict/describe properties that show good agreement with experimental data such as: density, heat of vaporisation, ion self-diffusion coefficients, conductivity and viscosity. The atomic polarisabilities were determined by fitting to the molecular polarisability in the gas phase from QM calculations, such

as density functional theory calculations. Once again while this shows much better agreement, as a quantum chemistry-based polarisable FF, a dramatic increase in computational time and memory is to be expected.

Instead of switching from a classical FF that is well-parameterised and highly transferable for a large variety of ILs, another proposition, put forward by Dommert and Holm [103], is to adapt the classical FF to derive partial charges from “bulk-like” ab initio MD simulations thus adding in corrections that the lack of polarisation requires.

2.3 Computer Codes and High-Performance Computers

There are now many available computer codes with which to run MD simulations, the choice of which is usually dependant on the potentials used and the target applications. Some examples of open-access and commercial software packages are LAMMPS, Amber, GROMACS and DL_POLY. Two codes were used for this research thesis:

1. The AMBER12[104] software package, specifically the SANDER MD engine. The package is often used for biomolecular systems and organic systems.
2. DL_POLY[105], typically DL_POLY 4[106] was used for most of the calculations, as the code is designed to be a general purpose classical MD package and additionally offered improved parallelisation of the calculation over several nodes.

High Performance Computing clusters were used for running these simulations, namely the UK National Supercomputing Service, ARCHER, and UCL’s Research Computing Services, Legion and Grace. Some benchmarking of AMBER, DL_POLY Classic and DL_POLY 4 is presented in Appendix II.

2.4 Running a Simulation

2.4.1 Initial Packing of Systems

Initial systems were built using fftool, a code written by Padua [107] and PACKMOL: A package for building initial configurations for MD simulations. [108] First, the fftool script and files are downloaded, containing numerous ion .xyz coordinate files and an il.ff file, which contains the parameters for CL&Pff. The instructions for preparing an input file for Packmol is followed for a system. Then using Packmol, the molecules are packed within spatial regions with the desired density and in such a way that the distance between any pair of particles is larger than a threshold tolerance, also specified. Further detail into the packing strategy is provided in a publication. [109] Fftool is then used for the building of DL_POLY input files containing the force field parameters (FIELD) and the coordinates of all the atoms (CONFIG). For AMBER simulations, tleap and xleap tools are used within the AMBER package for building input files for MD with the Generalised AMBER force field (GAFF).

2.4.2 Optimisation of the Initial Structure

Optimisation is a general term used to describe the process of structure relaxation. Another term to describe this process would be energy minimisation. Potential energy surfaces are often multi-dimensional surfaces, containing many points at which you are in a minimum. A minimum energy point would be when the first derivative equals zero and the second derivative is positive. If the system is too far from a minimum energy structure, the forces at the first step of an MD run could immediately fail, and the simulation would be too unstable to proceed.

Instead there are minimisation algorithms to help improve the quality of the starting structure, by searching the energy surface for minima. Two methods are used in this body of work:

1. “Zero” temperature MD. This is a MD simulation at 10 K, where every time step the molecules move in the direction of the computed forces, but are not allowed to acquire a velocity too large to result in any instabilities.
2. The Conjugate Gradient Method (CGM). This is a first order method and uses the first derivative of the function to determine the direction towards a minimum. This is different to the steepest decent method in that previous steps are included in the current search, allowing for increased convergence when close to a minimum.

2.4.3 Equilibration and Production

At the start, an equilibration period is necessary; usually this lasts a few thousand steps. This stage is used to ease the system towards the desired thermodynamic state (temperature and density) and equilibrate the kinetic and potential energies of the system. Once the temperature scaling/equilibration has been achieved, one can start the production run. A MD production run is usually run for many thousands of steps, and it is to this trajectory that analysis is applied.

2.5 MD Analysis

Many MD simulations can be analysed by simply visualising the trajectory and making key observations by eye, such as order/disorder, phase transitions and diffusion. There are some computational software programs that are used to draw the 3-dimensional structure of a trajectory and animate the time evolution of the system, a commonly used software for MD trajectories is Visual Molecular Dynamics (VMD).

[110] With numerous atomic representations possible (*e.g.* ball and stick, solid spheres, line, etc.), it is key to choose a suitable representation for the application. Additionally, specific colouring of atoms can prove to be a useful visual aid.

2.5.1 Thermodynamic Properties

As the simulation evolves, the MD code keeps computes and records various intensive and extensive thermodynamic properties, such as energies, volume, temperature, pressure etc. However, there are additional structural and diffusive analysis techniques that one may compute to further describe the system.

2.5.2 Radial Distribution Functions

Radial distribution functions (RDF) from MD trajectories is a pair correlation function which describes the average structure of particles in a molecular simulation. It is utilised to describe how density varies as a function of distance from a reference particle. An x-y plot is used to show the probability (g(r)) of finding a particle at a distance (r) from a particle. The calculation of the RDF is done by first selecting a particle (or group of particles) to be a reference. Then a series of concentric spheres are drawn, at fixed distances (Δr) apart with a reference particle at the centre. With snapshots taken at regular intervals, a count can be taken of the number of particles in each shell. The particle number data is averaged and divided by the volume of the shell to calculate the average density of particles. A depiction of this analysis method is presented in Figure 2.6.

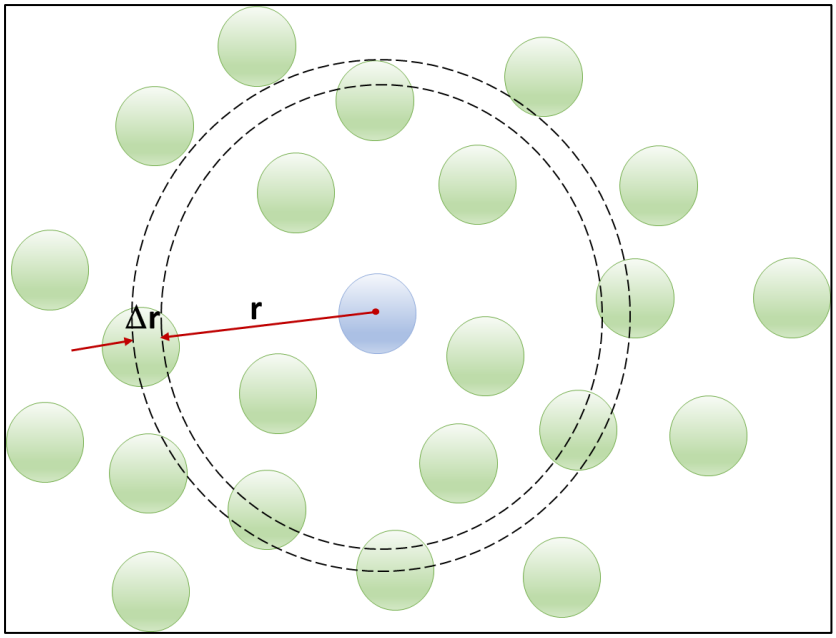

Figure 2.6. Graphical representation of radial distribution function.

In this body of work, TRAVIS was used for the calculation of RDFs, although VMD could also have been used (and was for comparison/validation).

2.5.3 Mean Square Displacement

In statistical mechanics, the mean square displacement (MSD) is a measure of the deviation of the position of a particle with respect to a reference position over time. Thus, how fast or slow the movement of an atom type or molecule is can be described by calculating the MSDs and plotting them comparatively. Some kinetic concepts can be utilised when analysing MSD plots; the elastic mean free path (l) rationale is imagined, where l is the typical distance travelled by a particle before a scattering event randomises direction of momentum, while conserving energy. Collision time can be described as:

$$\tau = \frac{l}{v_F} \tag{2.28}$$

where v_F is the assumed typical speed. Thus, on scales short compared to *l*, the motion is described as ballistic. Alternatively, on scales long compared to *l*, the motion is diffusive.

Furthermore, the self-diffusion coefficients of the atom types in the IL can be calculated from the MSDs of the atom types. The slopes of the MSDs are plotted, and the gradient is divided by 6 as per the MSD equation for a 3-dimensional simulation.

$$< r^2 > = 6Dt + Constant \tag{2.29}$$

After converting the units of diffusions coefficients from $Å^2\ ps^{-1}$ to $m^2\ s^{-1}$, the diffusion coefficient values can be compared to literature values.

Finally, from the diffusion coefficients, *D*, one can calculate the activation energy of diffusion of the particle, from equation 2.30

$$D = D_0\ exp\left(-E_a/k_BT\right) \tag{2.30a}$$

$$\ln D = lnD_0 - \frac{E_a}{k_BT} \tag{2.30b}$$

D_0 is the temperature-independent pre-exponential, also described as the diffusion coefficient at infinite temperature, E_a is the activation energy of diffusion, k_B Boltzmann's constant, and *T* temperature. Therefore, E_a can be obtained from the gradient of ln(D) versus 1/T Arrhenius plots.

2.5.4 Spatial Distribution Functions

Where RDFs show the probability of finding a particle at a certain distance in a distance vs. probability plot, spatial distribution functions (SDFs) depict the probability of finding a particle at a certain position in space around a fixed reference group of particles. They can be imagined as a "three-dimensional" augmentation of RDFs.

Here, a reference molecule requires selecting, along with three reference atoms (A-B-C, that are in a line), to place A at an origin, then B in the positive X axis and C in the X-Y plane with a positive Y value. This makes up a fixed plane vector in the molecule that is kept consistent throughout the snapshots of the trajectory to calculate the probabilities in the space around the reference molecule. SDFs are thus made up of a reference molecule structure (a .xyz coordinate file), with an isosurface depicting the probability of the observed atom or molecule (a gaussian cube file that contains volumetric data on a 3-D grid). TRAVIS was used for calculating the SDF and outputting the coordinate and smoothed gaussian cube file, and VMD was used for the visualisation. Finally, when visualising the SDF, an isovalue requires selecting and is done so based on how much information one wanted depicted. It is analogous to the cut-off in a RDF plot, *i.e.* the 3-D representation may show more than one coordination shell, and to "zoom" into the first or second of this, an appropriate isovalue needs to be chosen.

Chapter 3

Force Field Validation

Choosing a suitable force field (FF) is important to the validity and experimental accuracy of the IL simulations. The FFs we selected for comparison are the Generalised AMBER FF (GAFF) and CL&PFF. We have chosen 3 ionic liquids (ILs) to model with the two FFs, and two different molecular dynamics (MD) codes: AMBER and DL_POLY 4. We observe that AMBER calculations are more computationally efficient and highly parallelisable compared to DL_POLY, however on evaluation of IL densities CL&PFF, with DL_POLY, yields data more comparable with experimental studies. When considering the structure of the ILs, radial distribution functions are used to show that the FFs are in fact describing different degrees of long range structure. Additionally, at room temperature, the GAFF seems to show no diffusion of the ions whilst CL&PFF displays slow dynamics. We have demonstrated the importance of FF choice and validated the use of CL&PFF for further MD simulations of ILs.

3.1 Introduction

Chapters 1 and 2 illustrate both the numerous advantages of molecular dynamics simulations of ionic liquids and the main difficulties present when attempting to accurately model and describe ILs. Choosing a suitable FF is incredibly important to the validity and experimental accuracy of the IL simulations. To this end, the first major section of this research details the comparison of two popular FFs: Generalised AMBER FF (GAFF) and CL&PFF. GAFF is used to simulate large organic molecules and biological molecules [111] and as the ions considered in this study are all of a bulky organic nature, GAFF is a good FF to compare with. CL&PFF is a IL-specific FF that has been parameterised for various IL ions.

With the purpose of exploring a variety of ions: three ILs are considered: trihexyl(tetradecyl)-phosphonium chloride, $[P_{66614}][Cl]$, 1-butyl-3-methylimidazolium acecate, [BMIm][OAc] and 1-ethyl-3-methylimidazolium dicyanamide, [EMIm][DCA]. We aim to compare these systems in terms of density and IL structure, showing similarities and differences between the two FFs.

3.2 Computational Methods

PACKMOL [108] was used to build initial systems of similar atom size ~25500 (number of ion pairs in Table 3.1), AMBER 12 [104] and *DL_POLY* 4 [106] were used for minimisations and MD calculations using the GAFF and CL&P force fields respectively.

As achieving the correct density was desired, the isothermal-isobaric (NPT) ensemble was employed, using the Berendsen thermostat and barostat set at 298 K and 1 atm. A time step of 1 fs was used for a total of a 5 ns trajectory that was the production run. If a system was unstable and initial simulations failed, the canonical ensemble (NVT) was used and slow heating starting at 5 K was performed. An equilibration was considered successful only after stable and consistent results (energy and density) over periods of at least 500 ps. Simple cubic periodic boundaries were used for all simulations, achieving as close to true bulk properties as possible.

The reason two different MD programs were used for the two different FFs is simply due to ease of setting up with these force fields, and for comparison of calculation time and performance. AMBER, a package of molecular simulation programs used widely in biochemistry [112], deals with larger organic and biological compounds. As such, the time taken to perform long timescale calculations is greatly reduced comparative to the DL_POLY software. However, as only 5 ns simulations were carried out, DL_POLY jobs still completed in a reasonable time, of 2 to 3 days. This was for a long enough simulation time as there were no fluctuations in energies and volumes of the simulations.

Table 3.1. Names, structural formulae and abbreviations of the cations and anions used in this study. Ionic liquids simulated along with the number of ion pairs for each simulation box.

Ionic liquid	**Molecular structures of cation and anion pairs.** Atom colours are as follows: hydrogen (white), carbon (grey), phosphorus (cyan), oxygen (red), nitrogen (blue) and chlorine (green).	**Number of ion pairs**
trihexyl(tetradecyl)-phosphonium chloride, $[P_{66614}][Cl]$	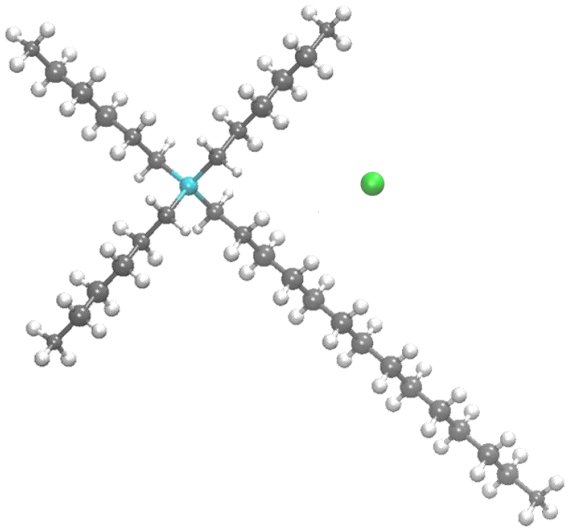	250 (later 94 and 500)
1-butyl-3-methylimidazolium acecate, [BMIm][OAc]	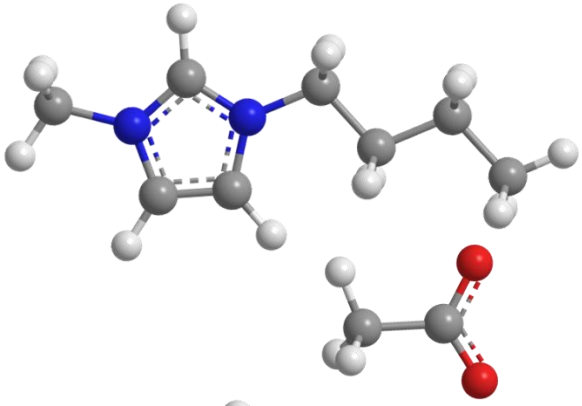	797
1-Ethyl-3-methylimidazolium Dicyanamide [EMIm][DCA]	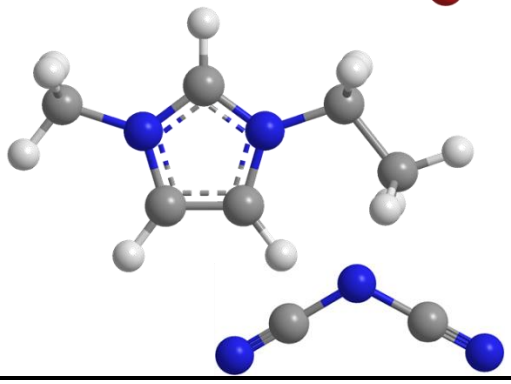	1062

3.3 Results and Discussion

3.3.1 Average Densities of Simulated Ionic Liquid Systems

The first property of the simulated system that can be easily compared to experimental is the density.

Table 3.2. Densities of ILs simulated compared to experimental data,[113] with percentage differences (%).

Density *(mol dm^{-3})*	**[P_{66614}][Cl] (%)**	**[BMIm][OAc] (%)**	**[EMIm][DCA] (%)**
Experimental	1.698	5.321	6.258
CL&PFF	1.660 (-2.2)	5.316 (-0.1)	6.262 (+0.06)
GAFF	1.630 (-4.0)	5.294 (-0.5)	6.279 (+0.3)

Experimental densities, [113] are well reproduced by molecular dynamics calculations with both force fields (see Table 3.2). However, CL&P seems to achieve values closer to experimental values, reducing the percentage differences by a factor of > 2. It is evident both FFs are resulting in much better densities for the imidazolium based ILs and this could be due to the largely different structures between the phosphonium based IL and the imidazolium based ILs. A probable reason behind this discrepancy could be the difference in conformational flexibility. Modelling a substantial number of large organic molecules made up of long alkyl chains accurately, in addition to the ionic nature, is a challenge. Perhaps this is more of a challenge than an accurate FF representation of the imidazolium, acetate and dicyanamide ions that contain rigid rings and groups.

3.3.2 Structural Analysis – Radial Distribution Functions

As seen above the densities resultant from the MD calculations of both FFs are in good agreement with experimental data and are not conclusive of disparities between the FFs. Radial distribution functions (RDFs) are often used to describe any long-range order in liquid and amorphous materials.

1. [P_{66614}][Cl]. The P-P RDF (see Figure 3.1 (top)) shows a peak at 7 Å with a large first solvation shell at 10 Å for both FFs. A difference is that a shoulder at 5 Å is seen with CL&P, which shows that the FF possesses greater ionicity to allow sharper RDFs. A more defined long-range order is seen with CL&P (black line): a second shell seen at 17 Å and a third shell at 23 Å. The charge on the phosphorus is +0.68 and first neighbouring carbons bonded to this central atom have a charge of -0.31. A tetrahedral geometry around the phosphorus atom and the long alkyl chains in every direction means the approach of another phosphorus is impossible within a 5 Å radius. The immediate structure around the phosphorus is seen in Figure 3.1.

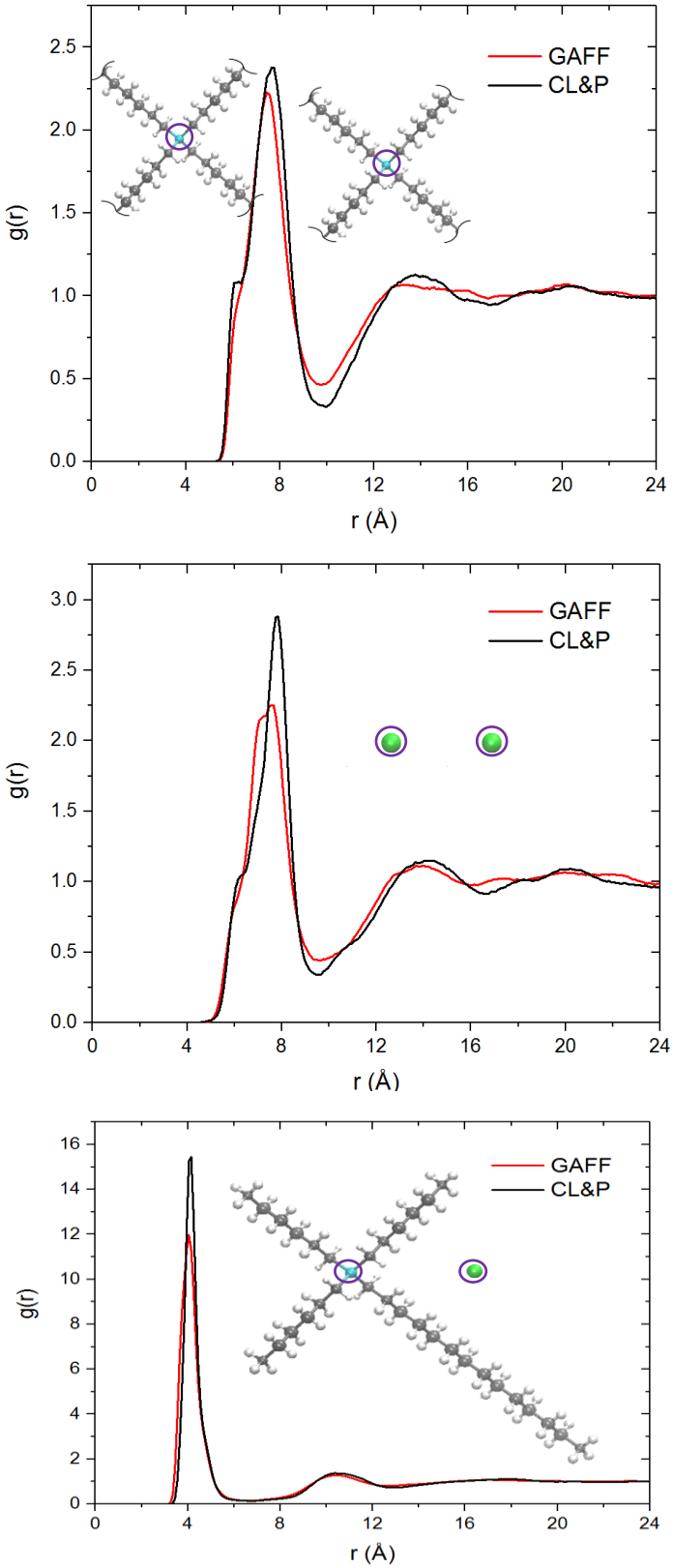

Figure 3.1. Site-site radial distribution function g(r) vs distance, r (Å), at T = 298 K, for $[P_{66614}][Cl]$. Cation-P to cation-P (top), anion Cl^- to Cl^- (middle) and cation-P to anion-Cl^- (bottom).

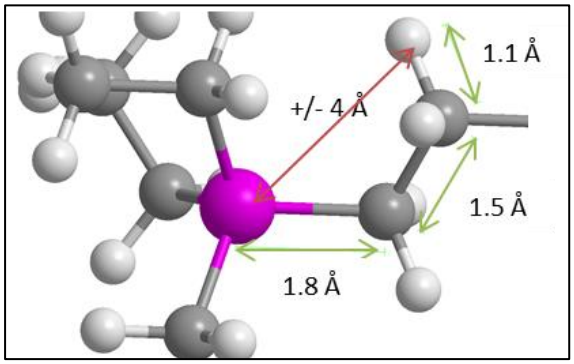

Figure 3.2. Zoom in of the geometry of tetrahedral phosphorus (pink) and alkyl chains.

At the first peak for the Cl-Cl RDF (Figure 3.1 (centre)) a slight increased distance at 7.5 Å is seen and can be explained by the increase in electrostatic repulsion with -1 charges on the chloride ions compared to the +0.68 charges on the phosphorus of the phosphonium cations. The electrostatic effect outweighs the bulky alkyl chains that would restrict the approach of a cation to another P of a different cation. Again a slightly more defined long range order is seen and this is comparable to previous MD simulations by Maginn [66] and by Padua *et al.* [75]

The cation-anion interaction seems to have much agreement between the two FFs. In Figure 3.1 (bottom), a large peak at ~4 Å is seen with a *g(r)* of 15.5 for CL&P and 12 for GAFF. The first solvation shell is at 7 Å then a second peak is at 10 Å and the second shell at 13 Å. Any long-range order is insignificant, but a plot of after 10 Å does again show a small more defined order with CL&P. The *g(r)*'s of the cation-anion interaction characterised by the height of the first peak is at least a factor of 4 greater than the like-charge ion interactions.

2. [BMIm][OAc]. Figure 3.3 shows the RDFs for the imidazolium ring-carbon situated between the two nitrogens and the carbon of the -CO_2 in the acetate ion (these are circled in the figures). The cation-cation interaction (Figure 3.3 (top)) with CL&P yields two peaks at ~6 Å and 8 Å. These peaks could be explained with pi-interactions being present between 2 to 3 imidazolium rings. In comparison GAFF shows less definition of these first peaks. CL&P shows minor peaks at 14 Å and an even lesser one at 19 Å. GAFF mimics the peak at 14 Å but past this distance no significant order is seen.

Acetate-acetate RDFs (Figure 3.3 (centre)) shows a slight difference between the structures computed with the two FFs. CL&P shows a long-range order in the structure: a first peak at 7.5 Å followed by a second peak at 12 Å and a third peak at 19 Å, the first solvation shell is at 10 Å, the second at 16 Å and the third at 25 Å. The GAFF simulation RDF shows agreement with the first peak and first solvation shell. After the second solvation shell, once again GAFF shows no long-range order.

The bottom RDF of Figure 3.3 shows the cation-anion interaction between the two highlighted carbons. CL&P distinctly shows two sharp peaks at 3.7 Å and ~5 Å and GAFF shows these two peaks with the same sharpness. CL&P then shows a third peak at 10 Å and a forth peak at 17 Å. The GAFF simulated structures show weaker interactions in the long-range with less order past 7 Å.

These RDF plots show that there are slight but significant differences between the structures simulated with the two FFs. There is a difference in the definition of long-range order (being present or not), but immediate solvation shells are not greatly different. CL&Ps long range order is in agreement with past studies on imiazolium based ionic liquids, theoretical and experimental [66], [70]. The increased structure and long-range order in CL&P is most likely due to higher electrostatic contributions which is widely different between the two FFs (Table 3.3).

Table 3.3. Average electrostatic energies per ion pair, in kJ mol^{-1}, for the two systems of $[P_{66614}][Cl]$ and [BMIm][OAc] with the two different force fields.

Electrostatic Energy (kJ mol^{-1})	**$[P_{66614}][Cl]$**	**[BMIm][OAc]**
CL&PFF	-304	-399
GAFF	-99.0	-278

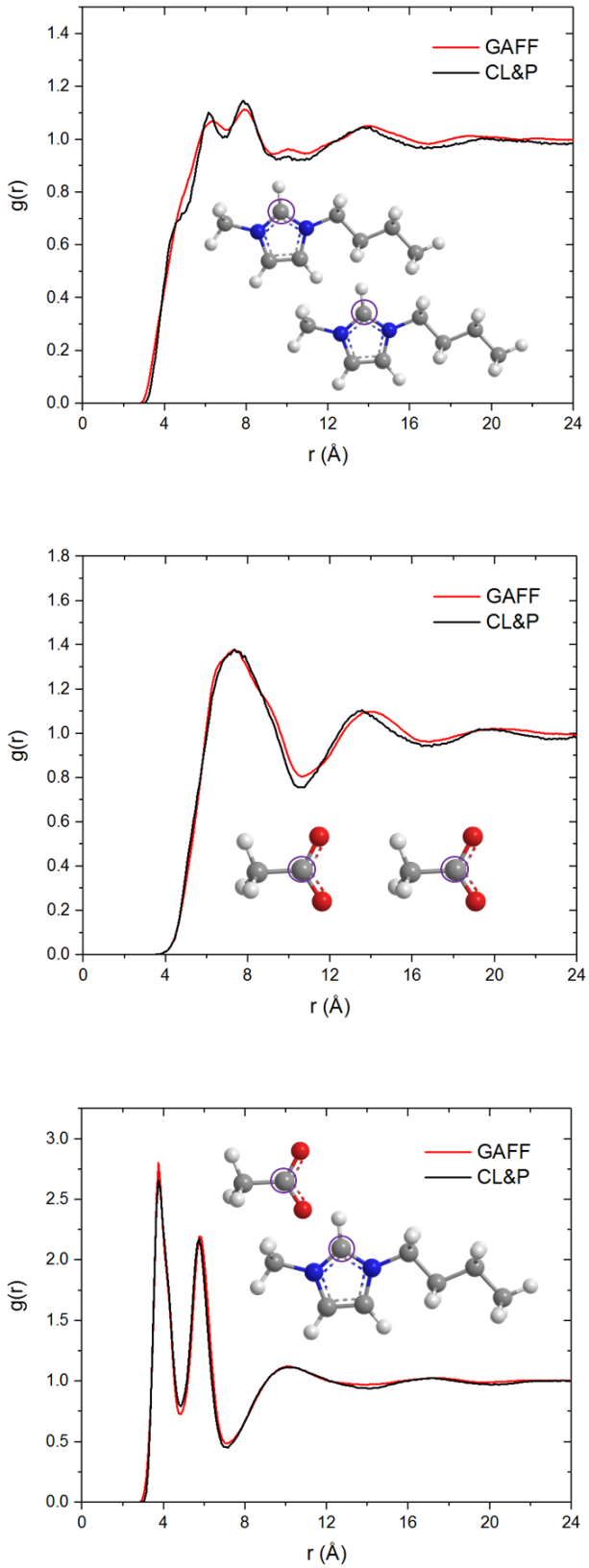

Figure 3.3. Site-site radial distribution function g(r) vs distance (Å) at 298 K, for [BMIm][OAc]. Order of plots from top to bottom: cation-cation, anion-anion and cation-anion.

3.3.2 Comparing diffusion of cation and anion in [P_{66614}][Cl]

Translational dynamics is quantified in terms of mean-square displacements (MSDs) of the central atoms of the cation (P) and anion (Cl). Figure 3.4 compares the cation and anion MSDs for the two FFs used. As dynamics in ionic liquids tends to be slow, typically self-diffusion coefficients of ions about 1 x 10^{-7} cm^2 s^1,[114] additional care needs to be taken to ensure that the system is simulated for a long enough time to be able to observe diffusive characteristics of the ions.

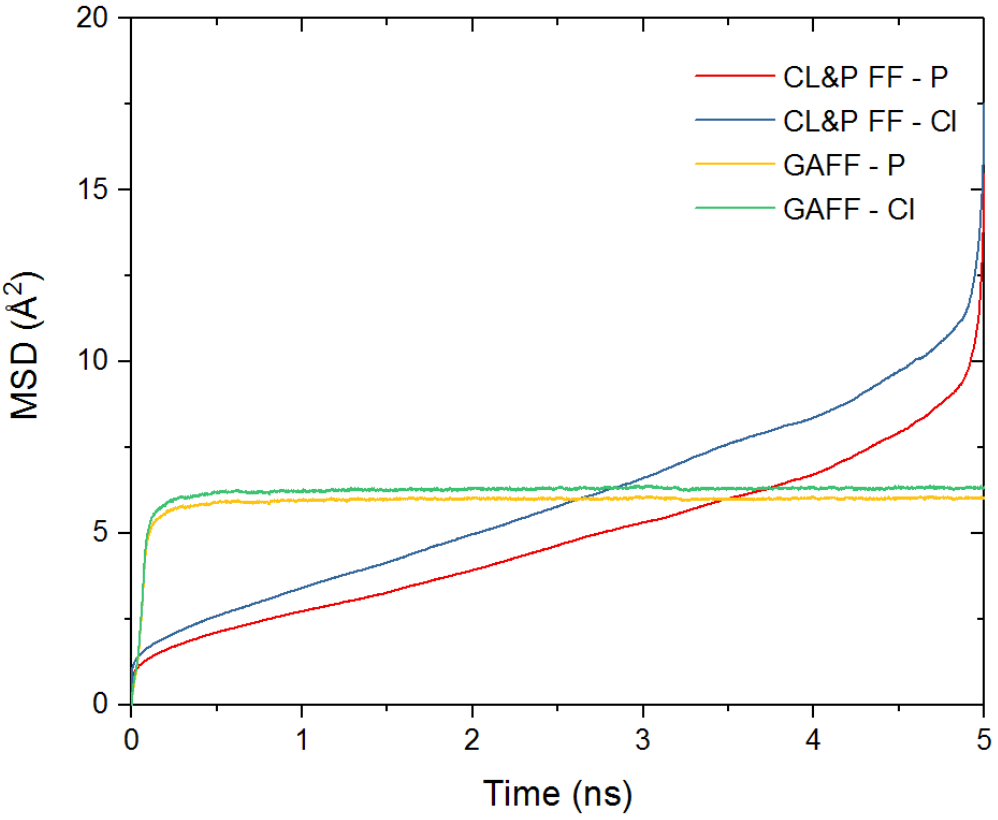

Figure 3.4. Mean-square displacements (Å) vs time (ns) for the phosphorus atom of the $[P_{66614}]^+$ and chloride ion, Cl^-, and T = 298 K.

Both FFs show a greater diffusion of the Cl^- ion compared to the phosphorus of the cation, which is consistent with the chloride ion being a single atom compared to the phosphorus of the phosphonium cation. An obvious difference between the two

forcefields is the shape of the MSD curves, the CL&P FF shows the customary MSD slope for a liquid,[115] whilst the GAFF MSD is showing a diffusion plateau. This means the simulation is showing non-diffusive ions in the system, at this temperature.

This can be attributed to the GAFF interactions requiring further energy to model a liquid structure; heating the system up would yield more diffusive ions. At increased temperatures, MSD plots would yield y-axis values of greater than 10 $Å^2$ and show steeper gradients.

3.3.3 Varying System Size of $[P_{66614}][Cl]$: 94 Ion Pairs and 500 Ion Pairs

Another measure of a force field's validity is the ability to reproduce resultant structures for varying system sizes. Long range order was seen in the structures for the ILs above modelled with the CL&P FF. To this end, a smaller system of $[P_{66614}][Cl]$ containing only 94 ion pairs, was simulated, effectively a third of the simulation box size above. The density achieved was consistent with the larger 250 ion pair system at 1.657 mol dm^{-3}, results presented in Table 3.4. Comparatively, a 1 ns simulation of 500 ion pairs of $[P_{66614}][Cl]$ (doubling the system size originally presented above) gives densities of 1.63 mol dm^{-3} for CL&P and 1.56 mol dm^{-3} for GAFF.

Table 3.4. Densities of ILs simulated with both FFs at different system sizes with percentage differences to experiment (%).

Density */mol dm^{-3}*	**94 Ion Pairs**	**250 Ion Pairs**	**500 Ion Pairs**
CL&PFF	1.657 (-2.4)	1.660 (-2.2)	1.630 (-4.0)
GAFF	1.628 (-4.1)	1.630 (-4.0)	1.560 (-8.1)

A depiction of the final frame in the trajectory is shown in Figure 3.5, where we see that even with a significant difference in simulation cell size, the structure has no discerning difference that can be seen by visualisation.

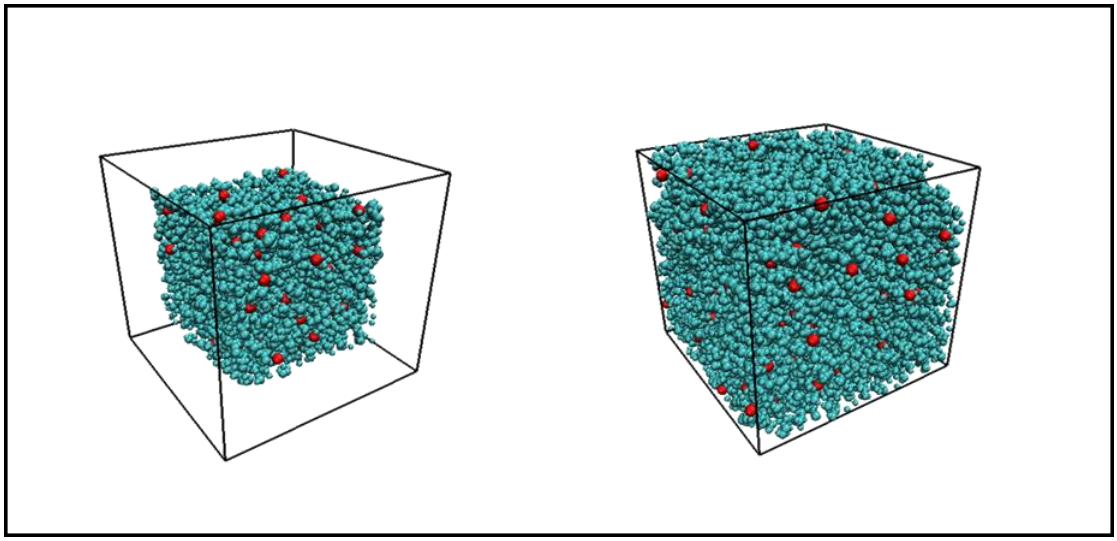

Figure 3.5. Snapshot of final configuration simulating [P_{66614}][Cl] with 94 ion pairs (left) and 250 ion pairs (right), visualised with VMD. Phosphonium cation in cyan, and chloride ion in red.

As for the structures resultant from the two different sized simulations, there is a general agreement in the number and position of peaks (Figure 3.6). The plots of the 94 ion pair simulations are roughened only due to the bin size used for the analysis and this is not indicative of great structural difference. Slightly increased distances of the solvation shells for the 94-ion pair system can be explained by the system-size effects upon cluster organisation. Both system sizes show a shoulder at the first peak for the like-ion RDFs. The long-range order up to 24 Å is mirrored in the smaller system simulation.

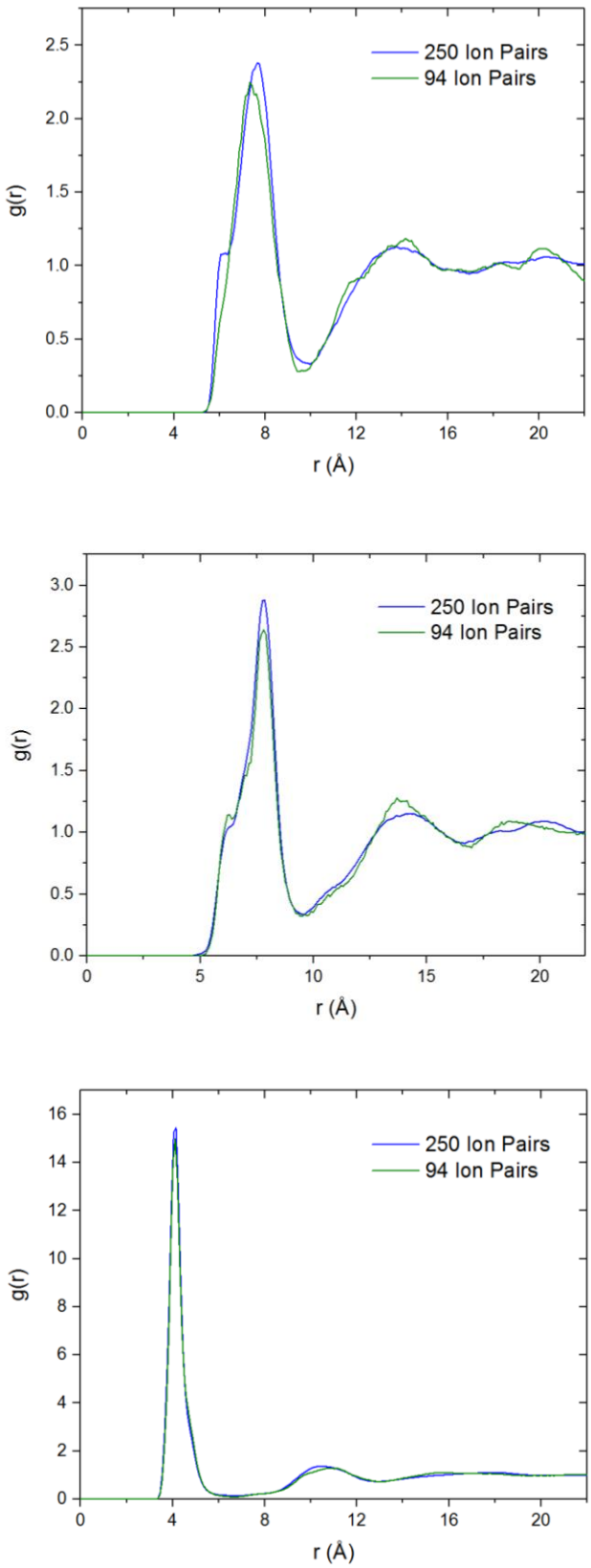

Figure 3.6. Site-site radial distribution function g(r) vs distance (Å) at 298 K, for $[P_{66614}][Cl]$, comparing two different system sizes, blue is 250 IPs and green is 98 IPs, using the CL&P FF.

3.3 Chapter Conclusions

Molecular dynamic modelling of ionic liquids is a growing field and a viable option to answering many questions about the structure and interactions within ILs. Experimental densities are well reproduced with force field methods, as seen in this work and by previous literature stated in the review. Whilst FFs, CL&PFF and GAFF seem likely to underestimate the densities for ILs, CL&PFF still achieved a more accurate density. Some similarities are seen in structures produced for all the ILs $[P_{66614}][Cl]$ and [BMIm][OAc] with the different FFs (i.e. RDFs' first shells) but far greater long range order is resultant with CL&PFF. The density of the [EMIm][DCA] IL only is overestimated with both FFs, and this may be due to underestimation of the charges of the DCA ion.

The validity of the CL&PFF is further examined by changing the size of the simulation box and comparing densities achieved and structural consistency for $[P_{66614}][Cl]$. A good agreement is seen in the different sized simulation cells results for both the density computed and the structure. Specific to this body of work and the 4CU project, this work has helped determine a FF to use for modelling ILs with molecular dynamics.

Chapter 4

Investigating the dynamics and structure of $[P_{66614}][NTf_2]$

Trihexyltetradecylphosphonium bis(trifluoromethylsulfonyl)imide, $[P_{66614}][NTf_2]$, is an IL that has been reported to possess unique properties experimentally, and are thus of interest on a molecular modelling level. Molecular dynamics simulations are calculated for this IL, varying temperature, to investigate the structural and dynamical properties. Experimental density was reproduced, and trends in diffusion are related for our calculations. We show that the IL has long-range order, that the cation diffuses less than the anion, and that the anion's configuration changes with increasing temperature.

4.1 Introduction

Phosphonium-cation based ILs are easily synthesised[116], [117] and may offer superior properties when compared to the more well-researched nitrogen cation-based ILs, such as imidazolium and pyrrolidinium cations. [118] There have been a number of experimental studies on the structure and properties of phosphonium based IL trihexyl(tetradecyl)-phosphonium bis(trifluoromethanesulfonyl)imide, $[P_{66614}][NTf_2]$.[118], [119] In contrast, whilst simulation studies have been carried out,[120] in-depth computational work is less readily available.

Variations of the four substituents on the phosphonium cation and the paired anion makes the possible variety of IL salts vast. An explanation for the delayed work into phosphonium based salts, compared to nitrogen-based ILs, could be due to tributylphosphonium only being available on a large scale after 1990. Following this, tetrabutylphosphonium chloride and bromide have become available on a multi-ton scale.[118], [121]

In this work, we have studied the IL $[P_{66614}][NTf_2]$ for a detailed description of the structure and diffusive properties of this IL at different temperatures. We report calculated densities, diffusion coefficients, radial distribution functions and special distribution functions for our systems. For comparison, experimental densities and viscosities are used for checking the accuracy of the force field and simulation.

4.2 Computational Methods

Liquid-phase classical molecular dynamics (MD) simulations were performed of trihexyl(tetradecyl)-phosphonium bis(trifluoromethanesulfonyl)imide, $[P_{66614}][NTf_2]$ using the DL_POLY 4 program package.[106] The initial configurations for MD simulations were generated by distributing 250 ion pairs in a very large simulation cell using the PACKMOL program.[108] The dispersion interactions were evaluated using a cut-off 10 Å, and the smoothed particle mesh Ewald (SPME) method was used to deal with the full electrostatic interactions. The trajectories were integrated using velocity Verlet algorithm with an initial time step of 1 fs. The temperature and pressure were controlled by the Berendsen method with a relaxation time of 0.8 and 1 ps, respectively. IL force field parameters were taken from the CL&P force field[88] which has been used widely in previously work, and is validated for 3 different ILs in Chapter 3. To minimise possible high energy structures in the initial configuration, a short 200 ps minimisation run was carried out of a low-density system, followed by a simulation at 500 K and 500 atm for 500 ps, to reduce the volume of the box. The NPT ensemble was employed and the density was calculated over a 5 ns MD trajectory, after a 2 ns equilibration run at 289 K, 323 K, 348 K, 373 K and 398 K. The liquid structure and mean squared displacement of the ions were calculated from a 5 ns production run.

4.2.1 Experimental Methods of Collaborators

Synthesis: $[P_{66614}][NTf_2]$ was synthesised from $[P_{66614}]Cl$ (50.8 g, 0.098 mol) dissolved in dichloromethane 100 ml and added dropwise to $LiNTf_2$ (28.7 g, 0.1 mol) dissolved in distilled water (100 ml) and allowed to stir under ambient conditions overnight. The organic layer was then extracted and washed with distilled water (100 cm^3) repeatedly five times and dried *in vacuo*.

Density measurements: The densities of the pure IL samples at 0.1 MPa were measured using a Mettler Toledo DM40 density meter at 25 °C with an accuracy of ± 0.01 °C by means of built-in precise Peltier thermostat. As recommended by the manufacturer, the densitometer was calibrated prior to measurements with degassed water and dehumidified air at atmospheric pressure. The uncertainty of the density is close to 1×10^{-4} g·cm^{-3}.

Viscosity Measurements: Reported thermal properties are given with accuracy close to ± 1 °C. The viscosity of the IL samples was measured before and after CO_2 absorption using a Bohlin Gemini Rotonetic Drive 2. The temperature in the cell was regulated at (25 ± 0.01) °C controlled by a built-in precise Peltier thermostat. The viscosity standard (ASTM Oil Standard S600 of CANNON, 1053 mPa·s at 25 °C) and ultra-pure water were used to calibrate the viscometer. Based on which, the uncertainty of reported viscosity measurements is close to ± 1 %.

CO_2 Sorption: The IL was pre-treated by bubbling with nitrogen at 80 °C for 1 h at a flow rate of 50 cm^3 min^{-1} to dry the sample and the weight of the sample was recorded. The sample was then bubbled with dry CO_2 at a flow rate of 50 cm^3 min^{-1} at room temperature (22 ± 0.1 °C) for the required period of time and the weight gain used to calculate the amount of CO_2 absorbed (taking into account the mass of the headspace). Taken from [122].

Work carried out by experimental collaborators at Queens University Belfast: Ms Corina McCrellis, Dr Rebecca Taylor, under the supervision of Prof Christopher Hardacre. Permission granted to present the experimental work in this thesis for comparative practice.

4.3 Results and Discussion

4.3.1 Density of $[P_{66614}][NTf_2]$

The simulated density of the $[P_{66614}][NTf_2]$ is obtained from MD simulations of the system at different temperatures, ranging from 298 K to 398 K, with 25 K intervals. The density is considered equilibrated after subsequent rolling averages do not fluctuate out of a 5% range; this was after 1 ns of the equilibration run. All the simulated densities at different temperatures are compared with experimental densities in Table 4.1 and Figure 4.1. The agreement between the simulated density at 289 K, 1.409 mol/dm^3, and experimental density, 1.395 mol/dm^3 is very good with an error of 0.9 %. Both simulated and experimental data show the same trend; decreasing density with increasing temperature. As temperature increased however, simulated densities were more overestimated compared to experimental densities. Although, we still maintained accuracy of calculation to experiment within 5 % error. This can be explained by simulations having fixed atom charges in the simulations, *i.e.* there is no polarisability in the force field thus the attractive forces between ions may be over-estimated. This inaccurate description of the interatomic forces may become more significant with increasing temperature and kinetic energy of the atoms.

Table 4.1. Experimental and simulated densities, in mol dm^{-3}, at temperatures 298 and 323 K, with percentage errors showing deviation from experiment.

Temperature (K)	Simulated Density	Experimental Density	Discrepancy (%)
298	1.409	1.395	0.9
323	1.388	1.368	1.0

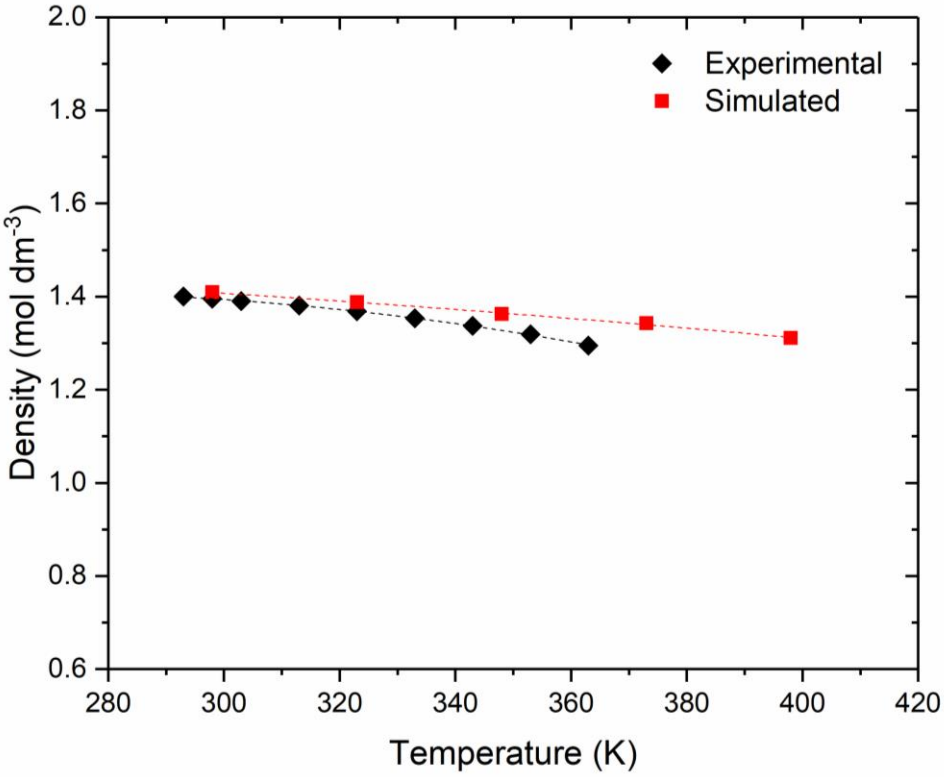

Figure 4.1. Simulated and experimental densities, mol dm^{-3}, of $[P_{66614}][NTf_2]$ shown as a function of temperature, K. Experimental density errors are on the order of 1 x 10^{-4} g cm^{-3}.

The over-estimation in density of calculated ionic liquids systems is seen in other studies.[97], [123], [124] Liu *et al.*[125] compared an all-atom FF and a united-atom FF for molecular simulations of phosphonium based ionic liquids, additionally finding that the united atom FF even further overestimated the density compared to experimental densities at 293 K.

4.3.2 Diffusion of $[P_{66614}NTf_2]$

The force field uses different atom types within the cation and anion (Figure 4.2). Translational dynamics were quantified with mean square displacements (MSDs). These were calculated for each of these atom types at the 5 temperatures (Figure 4.3 and Figure 4.4), except for the HC atom type due to there being 15 000 HC atoms per frame which took extensive calculation time.

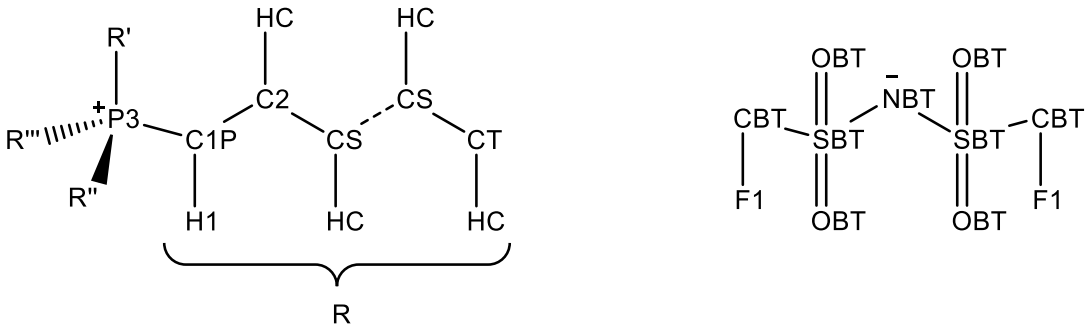

Figure 4.2. Adopted nomenclature for atom types in tetra-alkyl phosphonium cation and bis(trifluoromethanesulfonyl)imide anion. Dashed line indicates the continuation of alkyl chain.

The P3 and NBT atoms are the central and most charged atoms of the molecule and are considered the key atoms of the cation and anion respectively. We can see a greater range of diffusivity with the cation atom types compared to the anion, which can be attributed to the difference in size between the two ions as well as the combined ionic and organic, long-hydrocarbon chain nature of the cation.

Most of the MSDs show a good linearity in the sub-diffusive regime, with only a few pico-seconds of non-linearity in the ballistic motion range.

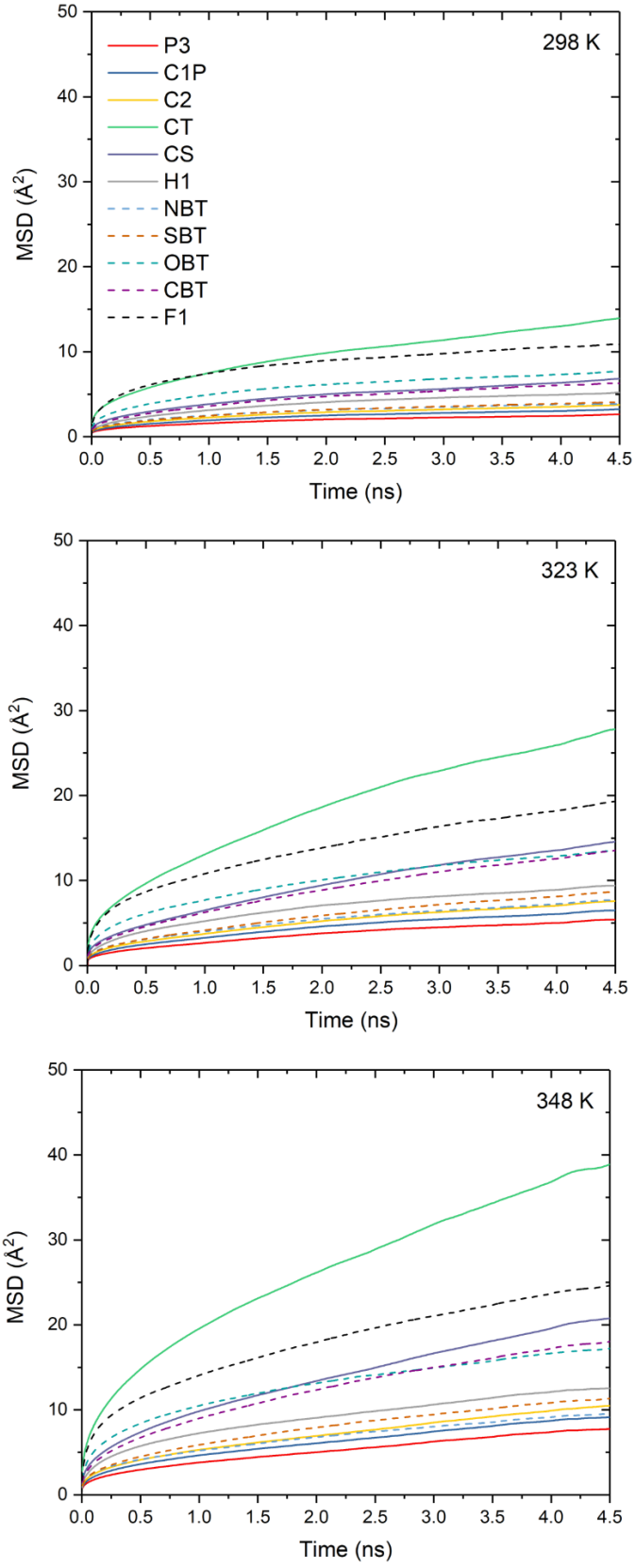

Figure 4.3. Mean square displacement of each atom type in the IL system, at temperatures 298, 323 and 348 K.

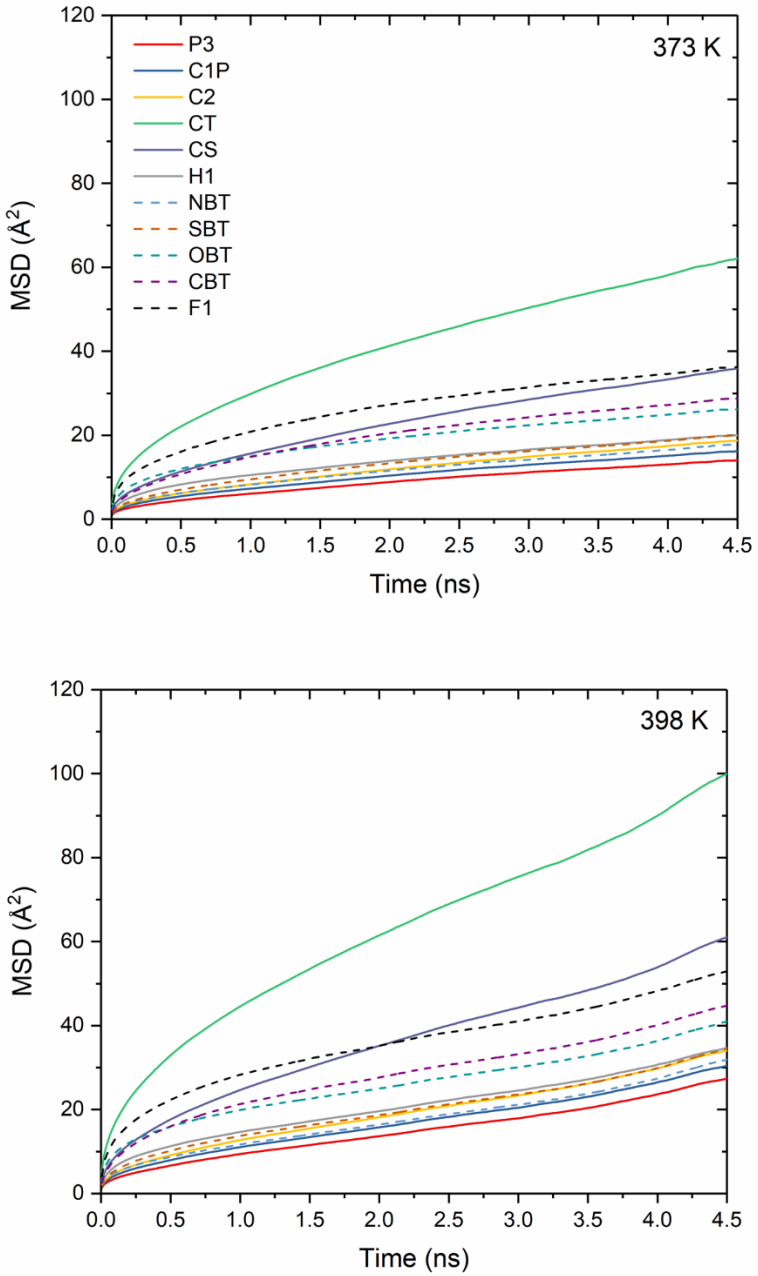

Figure 4.4. Mean square displacement of each atom type in the IL system, at temperatures 373 and 398 K.

To quantify the movement of the cation and anion as entire species, the individual atom type MSDs are summed with respect to their contribution to the ion, *i.e.* there is

a single P3 in every cation, but 4 C1P's and 4 CT's. Finally, to estimate the movement of the ion pair, all atom types are combined for the MSD of the ion pair (IP).

The MSDs of the cation, anion and IP are shown in Figure 4.5. At temperatures 298, 323 and 348 K the cation is the slower ion of the IP. However, at 373 and 398 K the cation in the diffusive range surpasses the anion in the IP.

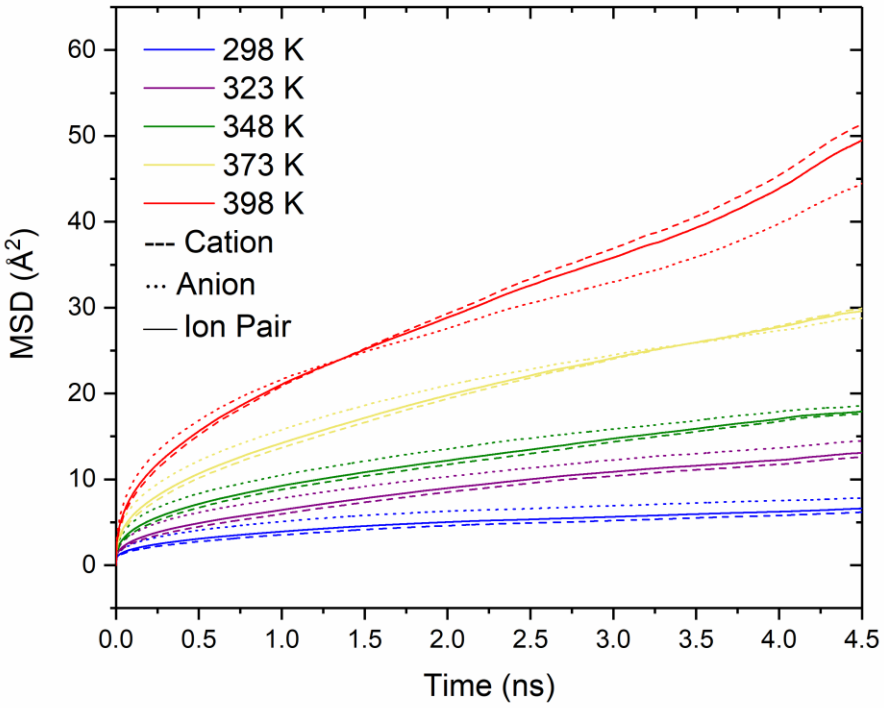

Figure 4.5. Mean square displacement of entire cation (dashed lines), anion (dotted lines) and averaged for total ion pair (solid lines), at temperatures 298 K (blue), 323 K (purple), 348 K (green), 373 K (yellow) and 398 K (red).

The self-diffusion coefficients of the atom types in the IL (Table 4.2) were calculated from the MSDs of the atom types (Figure 4.3, Figure 4.4 and Figure 4.5). The slopes of the MSDs are plotted between 0.25 – 4.5 ns and the gradients are divided by 6 as per the MSD equation (2.29).

After converting the units of diffusions coefficients from $Å^2\ ps^{-1}$ to $m^2\ s^{-1}$, the values can be compared to literature values. The range of these values do correlate with what is found in literature *e.g.* EMIM-SCN (SCN = thiocyanate) 6.98 × $10^{-12}\ m^2\ s^{-1}$ ([42], [45]) as ionic liquids do have slow dynamics.

Table 4.2. Diffusion coefficients, × $10^{-12}\ m^2\ s^{-1}$, of phosphonium atom (P) and terminal carbons (CT) of the cation, the nitrogen atom (N) of the anion, the entire cation, the entire anion and the average for the ionic pair.

Temperature (*K*)	P	N	CT	P_{66614}^+	NTf_2^-	IP
298	1.44	2.05	6.83	1.33	1.45	1.37
323	1.55	2.16	7.67	3.32	3.00	3.00
348	2.23	2.57	10.33	4.52	4.22	4.45
373	4.35	5.22	16.67	8.05	6.67	7.68
398	7.84	8.68	27.83	14.37	10.75	13.38

The diffusivity of the anion is greater than the cation, D_{NTf2} = 1.45 × 10^{-12} m^2 s^{-1} cf. D_{P66614} = 1.33 × $10^{-12}\ m^2\ s^{-1}$ at 298 K. This can be explained by the anion being significantly smaller, occupying smaller volumes and having no long alkyl chains, thus having less steric hindrance and being able to move easily. However, as temperature increases, there is a notable jump in the diffusion coefficient of the whole cation compared to the anion – which can also be explained by the increased contribution of the short-medium range of diffusion by the alkyl chains present in the cation.

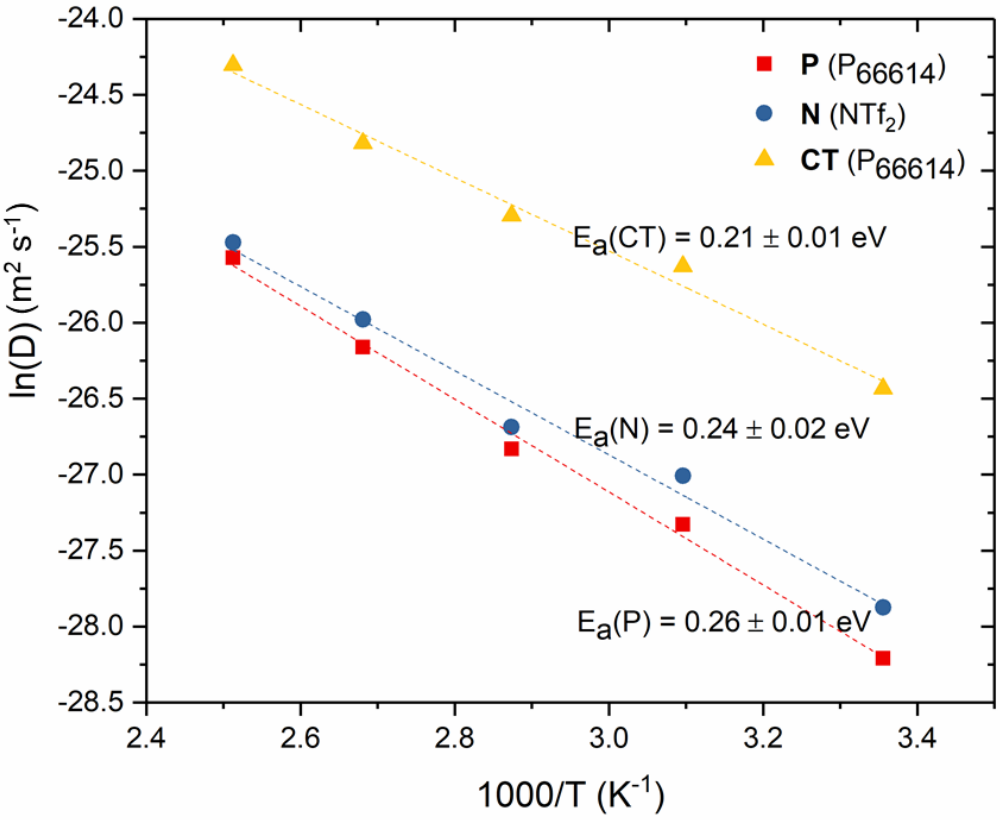

Figure 4.6. Arrhenius plot of diffusion coefficients of phosphorus (P) and terminal carbons (CT) of cation $[P_{66614}]$ and nitrogen (N) of anion $[NTf_2]$.

Arrhenius plots for key atom types diffusion in $P_{66614}NTf_2$ are shown in Figure 4.6, and for the entire cation and anion in Figure 4.7. Activation energies were derived and are displayed on the plots. The activation energies are all in the range of 0.20 – 0.26 eV, a range which agrees with literature values for activation energies of diffusion of ionic liquids. Heintz *et al.* reported activation energies of imidazolium ILs in the range of 17.5-19.3 kJ mol^{-1}, which converts to 0.18 – 0.20 eV. [115]

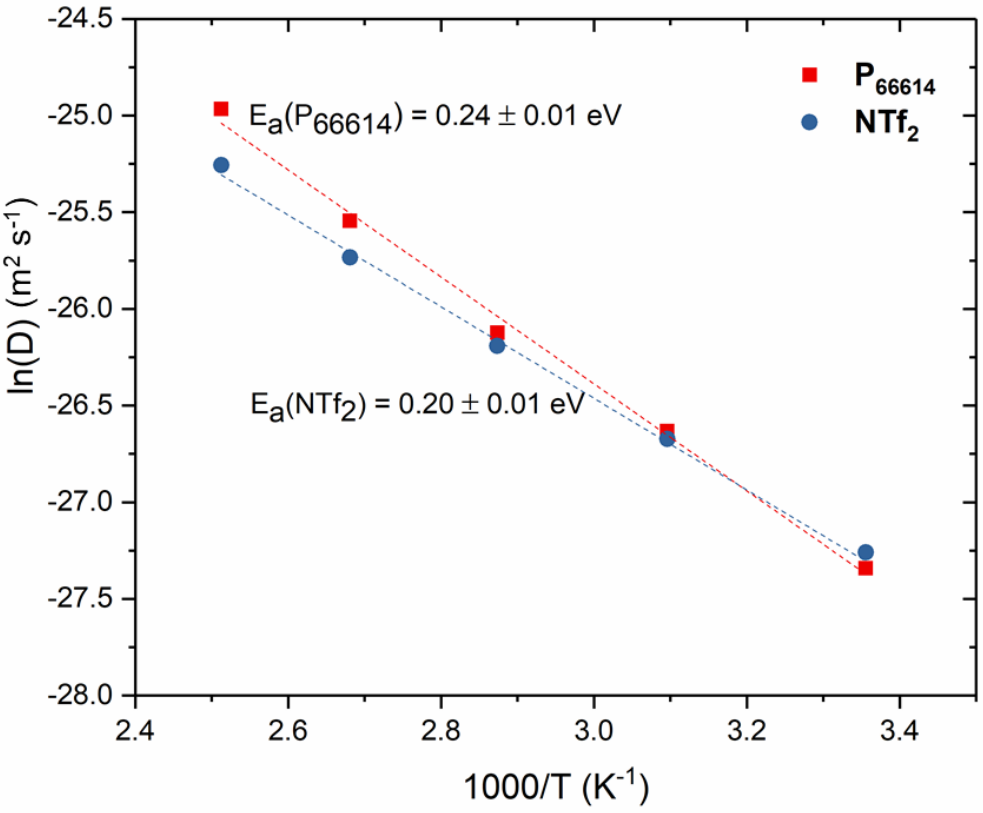

Figure 4.7. Arrhenius plot of diffusion coefficients of cation $[P_{66614}]$ and anion $[NTf_2]$.

To compare the diffusion behaviour with temperature for the entire cation vs. the entire anion, the Arrhenius plots are shown in Figure 4.7, including the activation energies of diffusion. We calculated $E_a(P_{66614})$ to be 0.24 eV whilst $E_a(NTf_2)$ is 0.20 eV. This shows that the NTf_2 anion travels more than the P_{66614} cation, in the IL structure, which is due to its smaller size and the globular nature of the phosphonium based cation.

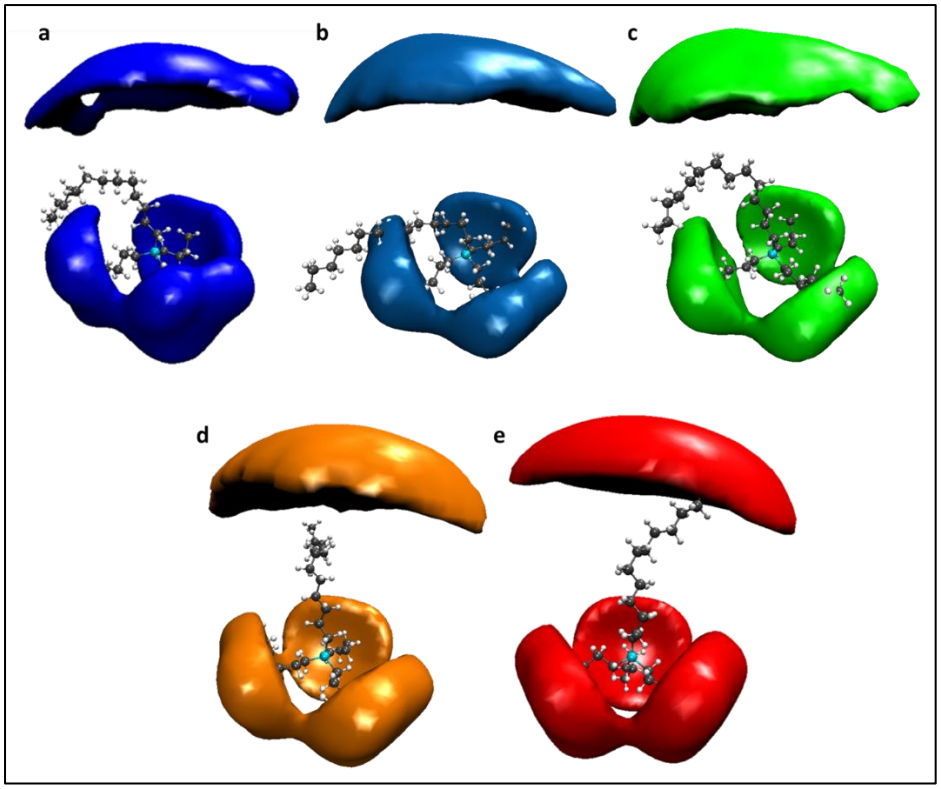

Figure 4.8. Intramolecular spatial distribution functions (SDFs) of the 4 terminal carbons (CT) around the central phosphorus atom, at 5 different temperatures: (a) 298 K, (b) 323 K, (c) 348 K, (d) 373 K and (e) 398 K. Isovalue of 0.25 used, reference molecule created from first time step.

An in-depth consideration into the cation's diffusive behaviour at different temperatures can be achieved by utilising special distribution functions (SDFs) of the terminal carbons of the alkyl chains relative to the phosphorus central atom. Figure 4.8 shows a rougher isosurface at the lower temperature of 298K, explained by less or slower movement of the terminal carbon. Conversely, as the temperature increases we observe enhanced movement of the alkyl chains showed by the smoothed, more regular isosurface. This further explains the increased movement of the cation being due to a less charged more alkyl behaviour at the end of the chains.

There are increased electrostatic interactions at lower temperatures and high van der Waals restricting the movement of the alkyl chains. These are overcome at higher temperatures allowing the alkyl chains to behave more like typical hydrocarbons.

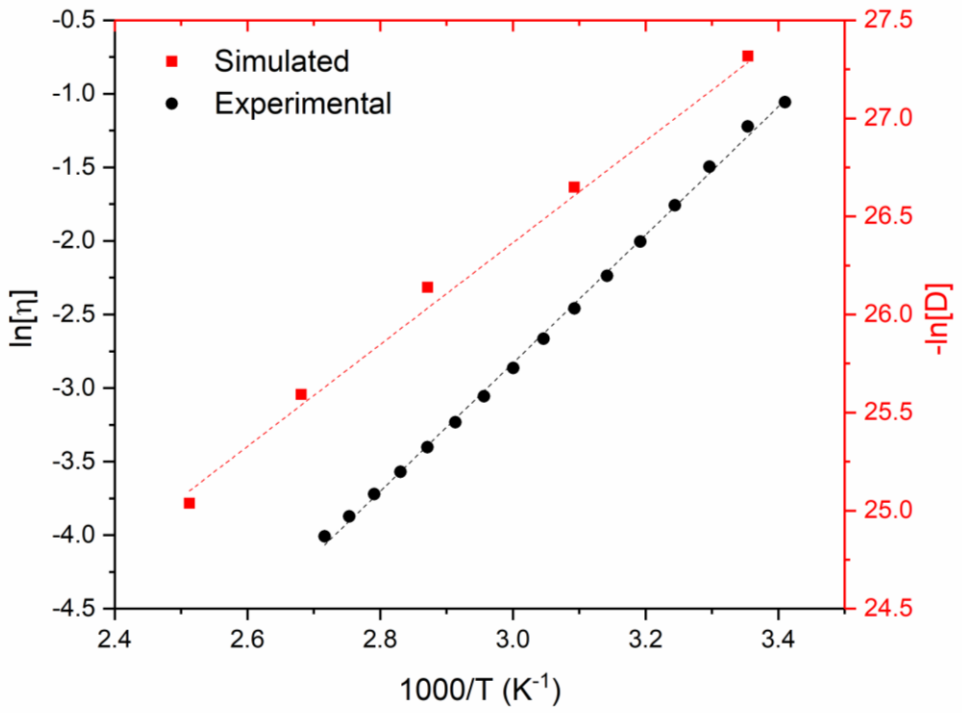

Figure 4.9. Arrhenius plot comparing the experimental viscosity (black circles, left y-axis) and the simulated diffusion coefficient (red squares, right y-axis).

To compare the simulated trend in the log of diffusion coefficient, -ln[D], with trend in log of experimental viscosity, ln[η], the values were plotted counter to each other in Figure 4.9. The experimentally measured viscosities display a continuous variation (linear relationship) with change in temperature. This is consistent with Stokes-Einstein equation:

$$D = \frac{k_B T}{6\pi\eta r} \qquad (4.1)$$

This relationship is reinforced by the molecular dynamics calculations as the simulated diffusivity for the ion pair also shows this linear relationship.

4.3.3 IL Structure of $[P_{66614}][NTf_2]$

Using TRAVIS ("TRajectory Analyzer and VISualizer"), site-site radial distribution functions (RDFs) of ionic liquid $[P_{66614}][NTf_2]$ were calculated at 298 K and are shown in Figure 4.10. The phosphorous of the $[P_{66614}]$ and the nitrogen of the $[NTf_2]$ are considered here to be the most central atoms of the molecule so in Figure 4.10a) the cation-cation and anion-anion interaction is described, b) anion- cation interactions are explored, but also with the sulphur (P-S) and oxygen (P-O) of the anion.

The like-ion to ion RDFs (Figure 4.10a) show long-range order in the IL structure, with anion-anion interactions occurring at a closer approach than cation-cation. This is due to the difference in size of the two; the anion is significantly smaller whilst the cation is more bulky and globular.

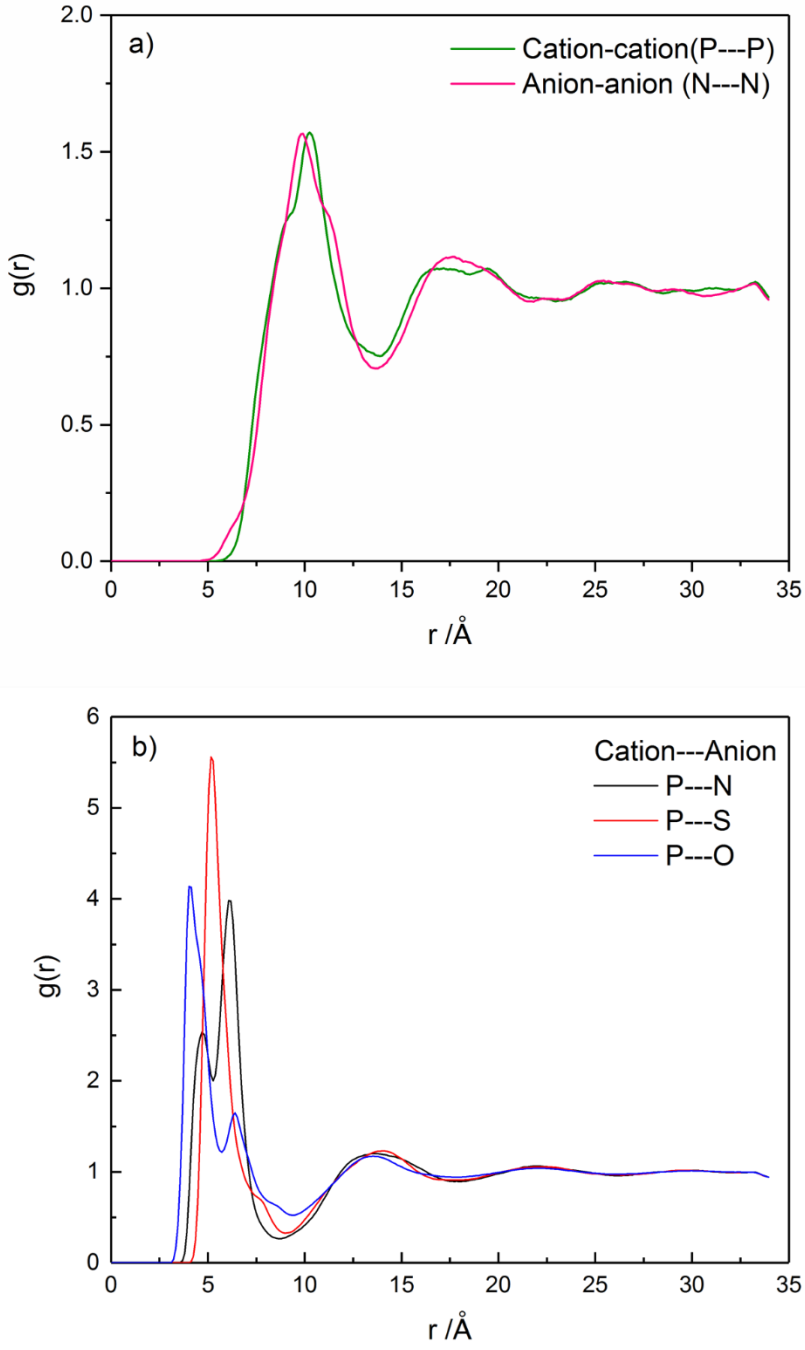

Figure 4.10. Site-site intermolecular radial distribution functions in $[P_{66614}][NTf_2]$ ionic liquid at 298K. a) RDF of phosphorus atom of P_{66614}^+ to itself (cation-cation, green), nitrogen atom of NTf_2 to itself (anion-anion, pink). b) All cation-anion RDFs with P of the P_{66614}^+ and nitrogen (black), sulphur (red) and oxygen (blue) of the anion, NTf_2^-.

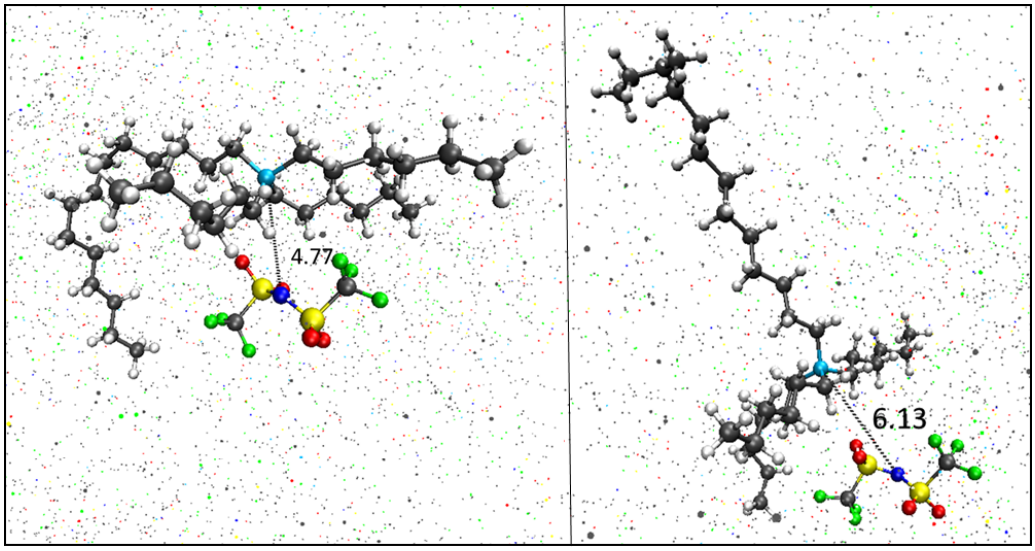

Figure 4.11. Picture of two different P-N distances, in Å, in simulation trajectory at 298 K. Only one IP is shown in CPK, against the bulk of the IL in small points.

The P-N RDF shows a double peak for the first coordination shell, Figure 4.10b (black line). To explore possible conformations that could lead to these peaks, we visualised the trajectory in VMD, Figure 4.11, and were able to snapshot examples of distances between P(P_{66614}) to N(NTf_2) that would correspond to the two different peaks of that first coordination shell.

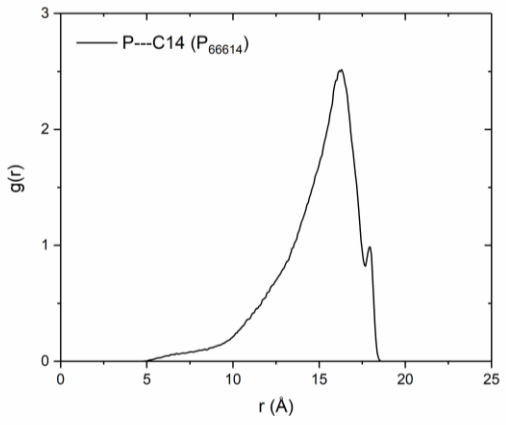

Figure 4.12. Intramolecular RDF between phosphorus to terminal carbon of the C14 chain, at 298 K.

The intramolecular RDF of phosphorus to the terminal carbon of the tetradecyl alkyl chain (Figure 4.12) shows that the range of probabilities for this distance is quite large. A g(r) appears after 5 Å, peaks at 16 Å, shoulders at 17.6 Å before trailing off to zero again at 18 Å. Both the shapes of the SDFs in Figure 4.8 and this P-CT RDF support the known reported behaviour of the P_{66614} cation. [126], [127]

A picture depicting the highly-charged and lesser-charged atoms in the 250 ion pairs, at the end of the production run is depicted in Figure 4.13 shows that whilst there is no clear-cut long-range order, there is grouping of the highly charged atoms whilst the lesser charged atoms are so abundant they spread across the entire simulation box.

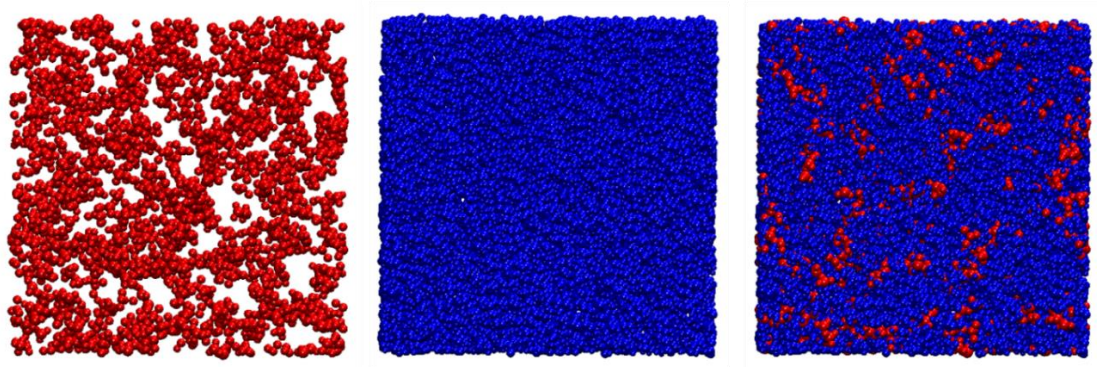

Figure 4.13. Picture of simulation box, 250 ion pairs of $[P_{66614}][NTf_2]$ at 298 K, with all highly charged atoms (P, N and O) coloured red and lesser charged atoms (alkyl C and H) coloured blue.

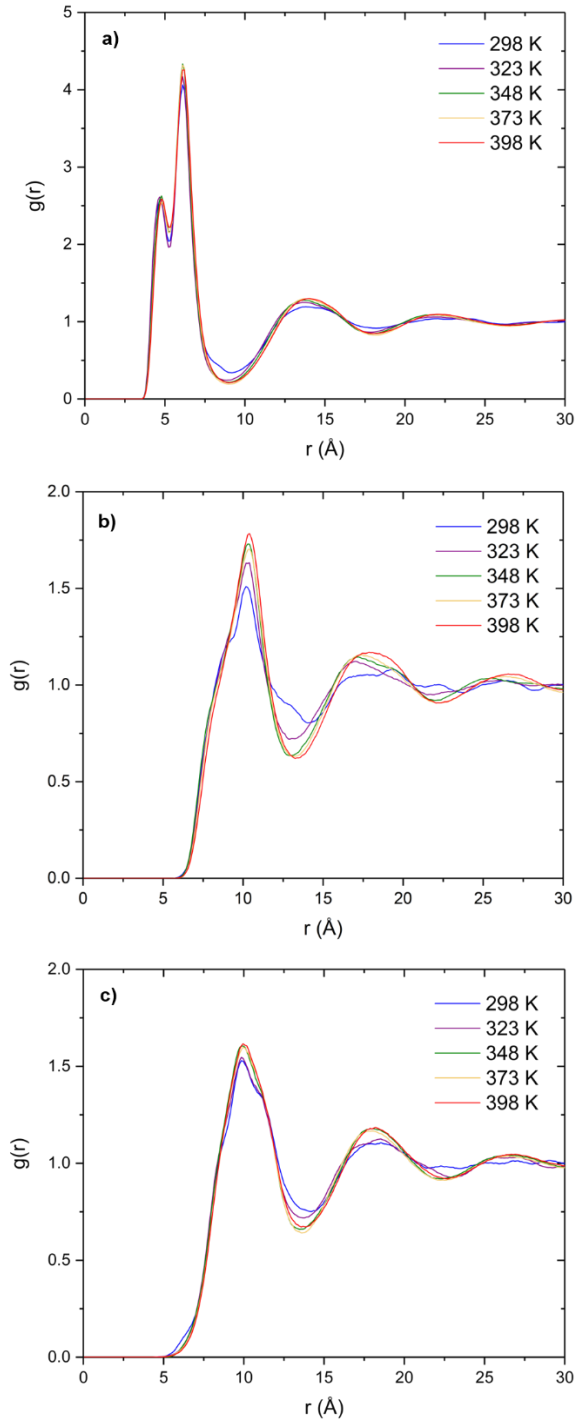

Figure 4.14. Site-site intermolecular radial distribution functions in $[P_{66614}][NTf_2]$ ionic liquid at increasing temperatures. a) RDF of phosphorus atom of P_{66614}^+ to nitrogen atom of NTf_2 (cation to anion), b) P to itself of P_{66614} (cation to cation) and c) N to itself (anion to anion).

Subsequently, a consideration into the effect of temperature on the structure of the IL, is shown in Figure 4.14. We observe the first solvation shell is sharper with increasing temperature, for all three RDFs. It appears that at 298 K, there is more structure with shoulders in both like-like ion RDFs (Figure 4.14b and c). With increasing temperature, there is coalescence of local minima resulting in a smoother RDF and higher intensity coordination peaks for all three shells. This effect of temperature is most distinct in the P-P (Figure 4.14b) interaction. A deeper investigation of the oppositely charged ions RDFs was achieved by observing the time development of the P-N distances at the low and high *T* (Figure 4.15). This shows that there is a possibility of ion pairs exchanging coordination as the plot lines show greater overlapping at the higher *T* (circled red in the plot). This adds to the description for the change in structure seen with increasing *T*.

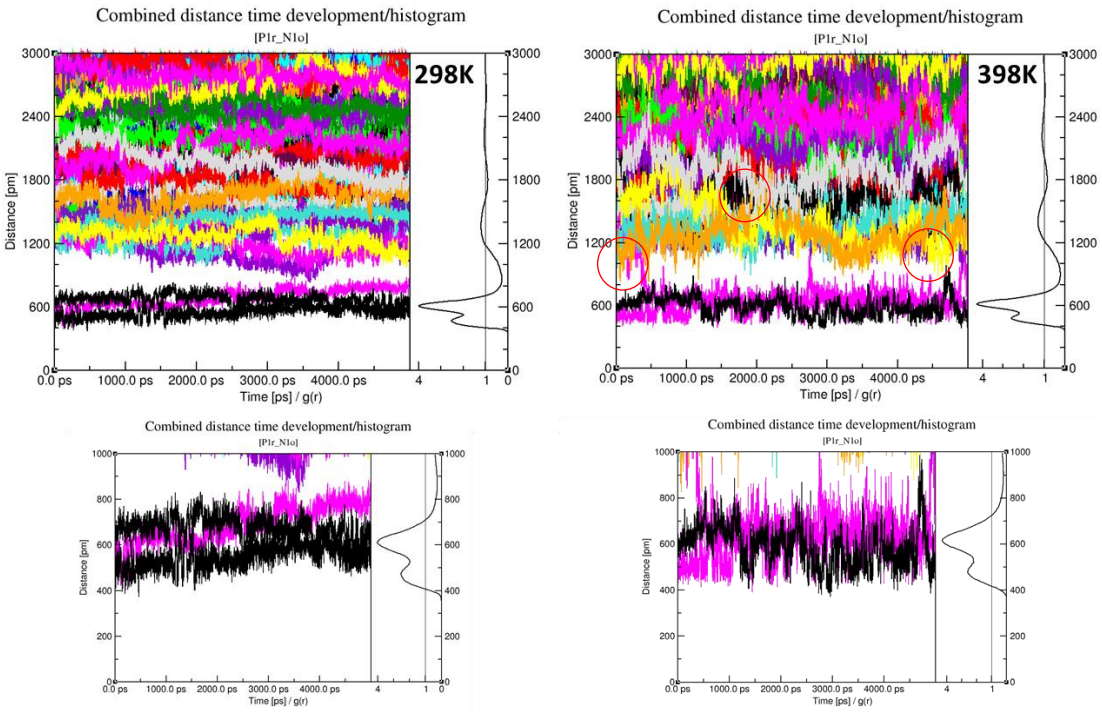

Figure 4.15. Temporal development of distances, in pm, between $P(P_{66614})$-$N(NTf_2)$ averaged out to RDF plots, at *T* = 298 K and 398 K. Image and plot are taken directly from TRAVIS outputs, in the default units of pm and ps.

***Cis/Trans* behaviour of NTf_2.** The ratio of the *cis/trans* orientation of the bis(trifluoromethanesulfonyl)imide anion, $[NTf_2]$, can be obtained from the simulation in two ways. The first is the distribution of $CF_3\cdots CF_3$ distance and the second is the distribution of the C-S···S-C torsional bond angle, as seen in Figure 4.16.

A clear bimodal distribution is seen in both the $CF_3\cdots CF_3$ distances and the C-S···S-C torsional bond angles as a function of the number of anions. The *cis* configuration corresponds with the $CF_3\cdots CF_3$ distance of ~4.2 Å and the C-S···S-C torsional bond angle of ~40°, and the *trans* configuration corresponds with the $CF_3\cdots CF_3$ distance of ~5.1 Å and the C-S···S-C torsional bond angle of ~170°. About 80% of the anions in the simulation exist in the *trans* configuration, at 298 K. These findings are comparable to previous experimental and computational research on 1,3-dimethylimidazolium bis(trifluoromethylsulfonyl)imide.[128]

The effect of increasing the temperature of the system from 298 K to 323 K seems to have no significant effect on the *cis-trans* ratio of the NTf_2, however at 348 K, 373 K and 398 K we see even less *cis* conformations as the ratio moves to the *trans*. A possible reasoning of this could be imagined by considering the energy profile of the system. Upon heating, we are overcoming an energy barrier related to a *cis* local minimum resulting in a decrease in the probability of the *cis* configuration relative to the *trans* configuration.

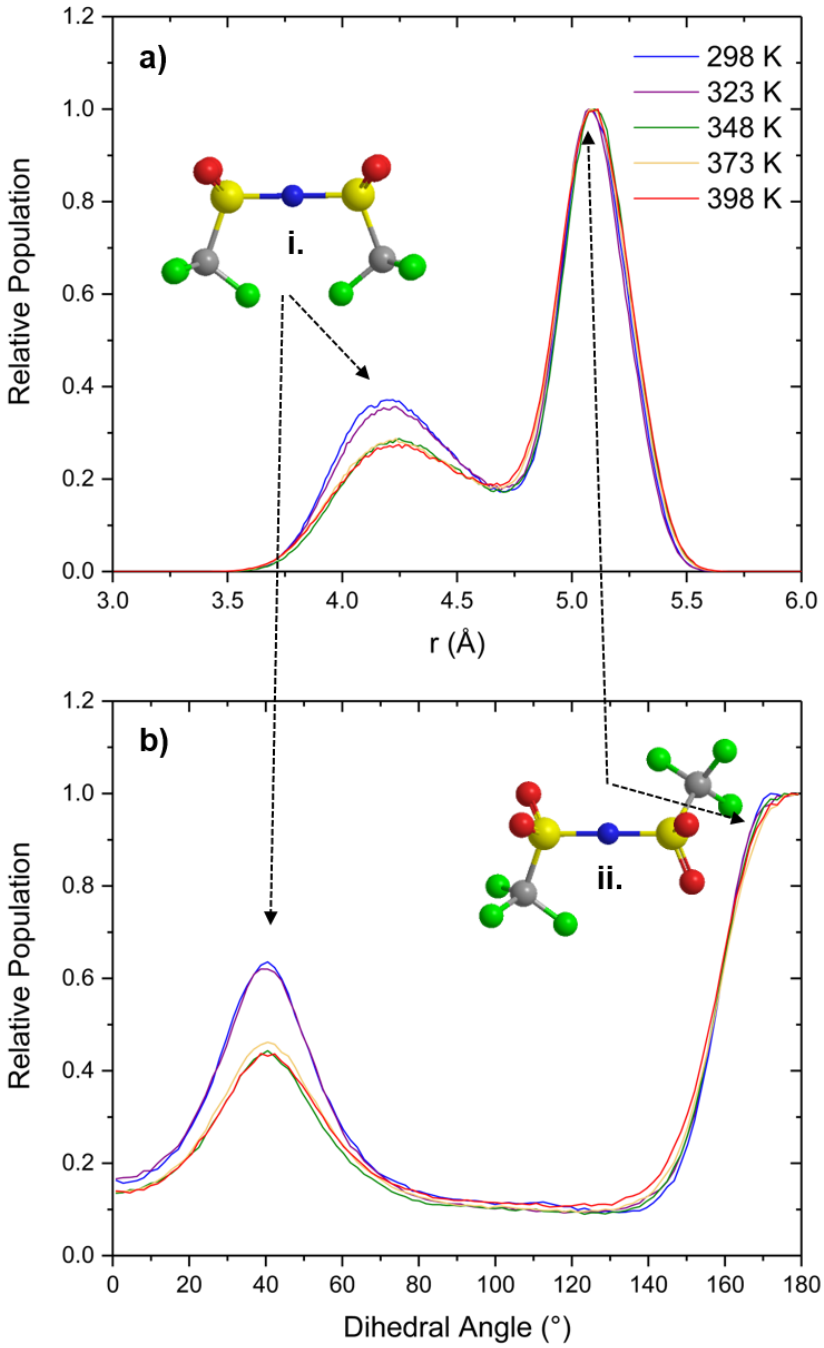

Figure 4.16. Distribution of the a) $CF_3\cdots CF_3$ distances and b) C-S···S-C dihedral angle as a function of the number of anions in liquid $[P_{66614}][NTf_2]$, at different temperatures. Models showing i. the *cis* and ii. the *trans* configuration of the bis(trifluoromethanesulfonyl)imide anion, $[NTf_2]$.

4.4 Chapter Conclusions

Molecular dynamics simulations successfully described the density of a $[P_{66614}][NTf_2]$ system, compared to experimental data, for a range of temperatures. We evaluated the diffusion of different atom types in the IL, along with the average for the cation, anion and the ion pair. We observe the cation diffuses slower the anion, and that the trend in diffusivity of the simulated system is comparable to experimental viscosity. The structure of the IL is investigated with radial distribution functions and compared across different temperatures, to demonstrate that temperature significantly changes structure. Finally, the *cis/trans* configuration ratio in the anion $[NTf_2]$ is measured to note a change in heating the IL between 323 and 348 K.

Chapter 5

Carbon Dioxide Capacity of $[P_{66614}][NTf_2]$

The phosphonium based IL is further explored with the addition of carbon dioxide, as the potential for ILs to be used for CO_2 capture is of interest. Once more, MD simulations are utilised for the study of the IL system with different loadings of CO_2. We observe significant changes in IL structure and IL diffusion, along with the preferential sites of coordination of CO_2 in the IL structure. Carbon dioxide dynamics is reported and show changes with different loadings.

5.1 Introduction

In this work, we have studied the IL $[P_{66614}][NTf_2]$ system with 3 loadings of CO_2 for a description of the structure and diffusive properties of the IL and CO_2 at different temperatures. We report calculated radial distribution functions, mean square displacements, diffusion coefficients and special distribution functions for our systems. Previous researchers have reported unique properties for the IL-CO_2 systems, both experimentally,[97] and computationally. This includes experimental CO_2 sorption and desorption studies on different groups of ILs', monitoring density and viscosity differences upon CO_2 sorption, along with computational studies on the detail of IL-CO_2 interactions. [97], [129], [130]

When deliberating the loadings of CO_2, the first choice was based on experimental data that reported CO_2 uptake of 0.03 nCO_2:nIL at 22 °C.[131] This converts to 7 CO_2 molecules in 250 IPs. Alternatively, a different experimental study reported a CO_2 loading of 0.169-0.205 nCO_2:nIL at T = 20 °C and a pressure of 1-2 atm, which scales to about 50 CO_2 molecules in 250 IPs. [132] 15 CO_2 molecules was chosen as a intermediate between these two but still a dilute system.

5.2 Computational Methods

Liquid-phase classical molecular dynamics (MD) simulations were performed of trihexyl(tetradecyl)-phosphonium bis(trifluoromethanesulfonyl)imide, $[P_{66614}][NTf_2]$ with CO_2 using the DL_POLY 4 program package.[106] The initial configurations for MD simulations were generated by distributing 250 ion pairs, with loadings of 7, 15 and 50 CO_2 molecules, in a simulation cell (80 Å cell length) using the PACKMOL program.[108] The dispersion interactions were evaluated using a cut-off of 10 Å, and the smoothed particle mesh Ewald (SPME) method was used to deal with the full electrostatic interactions. The trajectories were integrated using velocity Verlet algorithm with an initial time step of 1 fs. The temperature and pressure were controlled by the Berendsen method with a relaxation time of 0.8 and 1 ps, respectively.

IL force field parameters were taken from the CL&P force field[88] and CO_2 parameters were taken from the TraPPE force field.[133] To minimise possible unrealistic geometries in the initial configuration, a short 200 ps minimisation run was carried out of a low-density system, followed by a simulation at 500 K and 500 atm for 500 ps, to reduce the volume of the box. The NPT ensemble was employed with a 2 ns equilibration run at 289 K, 323 K, 348 K, 373 K and 398 K. The liquid structure and mean squared displacement of the ions were calculated from a 5 ns production run, with the NPT ensemble.

5.3 Results and Discussion

5.3.1 Carbon Dioxide Coordination around Anion and Cation.

Figure 5.1 shows the atomic site-site radial distribution functions (RDFs) for the phosphorus atom of the cation, $[P_{66614}]^+$, with the carbon and oxygen of the carbon dioxide molecule, followed by the nitrogen and oxygen atoms of the anion, $[NTf_2]^-$, with the carbon dioxide atoms. These RDFs were calculated and plotted for all the carbon dioxide loadings, at two temperatures: 298 K and 348 K, and all show a generally similar structure. There are some changes in the *g*(r) of peaks across the different CO_2 loadings, but these are not qualitative changes. This observation means that the loading of the CO_2 does not greatly affect the CO_2-IL interactions. Significantly, a key observation to be made is that the CO_2 coordinates more and closer with the anion than the cation. The reasons for this are further discussed below. Upon increasing the temperature, the peaks in the RDFs all show a decrease in the *g*(r) and this is expected with an increase of temperature. This is as at high temperatures; more configurations are being sampled – the distribution flattens out and the g(r) peaks have lower maxima. The cell volumes of all simulations at the varying loadings of CO_2 and *T* are presented in Table 5.1, showing significant increases in volume upon heating.

Table 5.1. Simulation cell volumes in nm^3, at temperatures ranging 298 – 398 K, for the different IL systems.

Cell volumes (in nm^3)	**298 K**	**323 K**	**348 K**	**373 K**	**398 K**
Pure IL system	294.48	298.61	302.38	308.64	312.77
IL with 7 CO_2	294.61	297.94	304.01	309.19	314.43
IL with 15 CO_2	295.14	299.42	303.46	310.84	315.54
IL with 50 CO_2	296.47	301.44	305.23	312.91	318.47

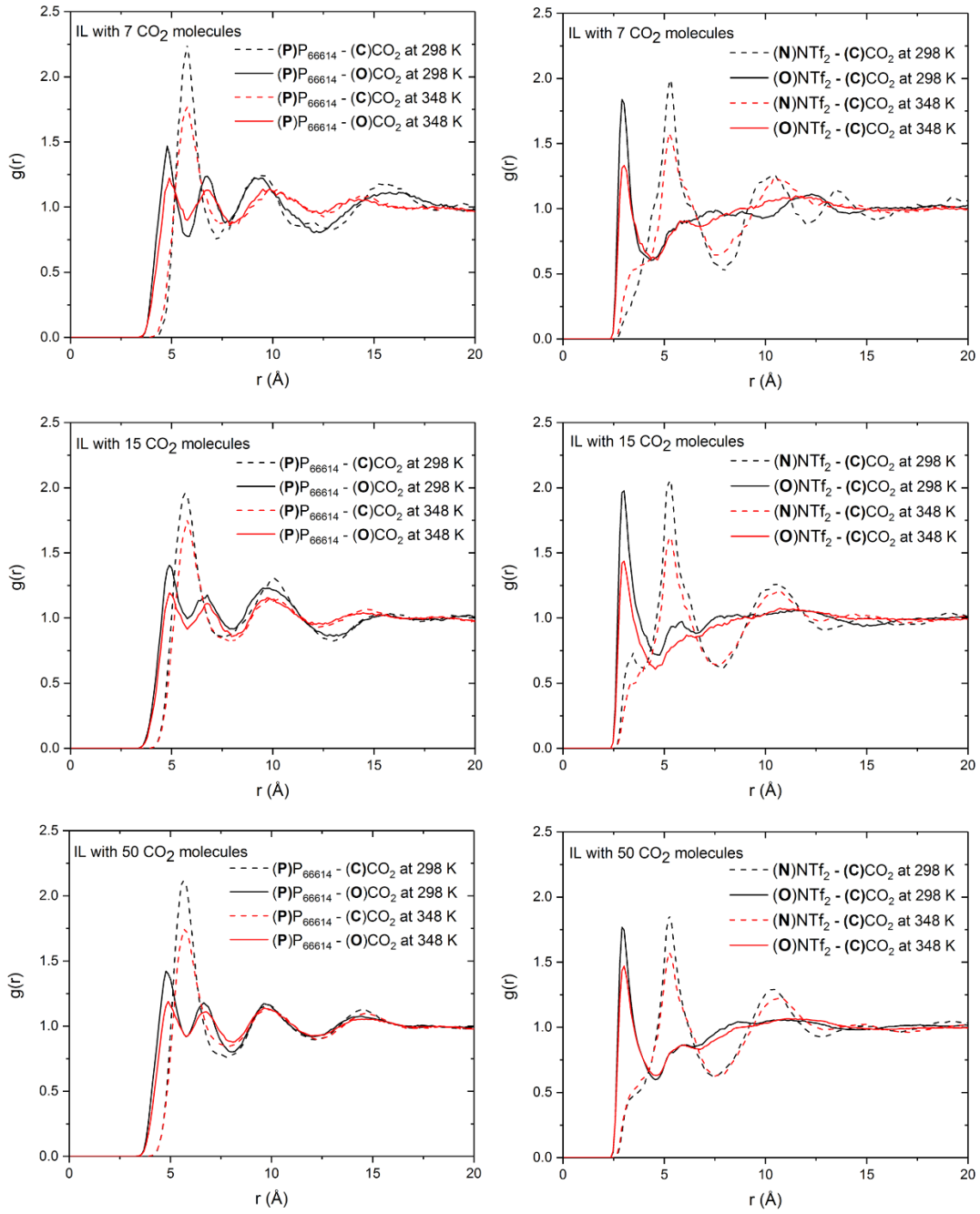

Figure 5.1. Comparison of atomic radial distribution functions between the IL and CO_2, at the three different loadings of CO_2. Labels are kept consistent between the different systems, allowing for direct comparison.

The oxygen of the carbon dioxide makes the foremost approach (peaking at 4.78 Å) to the central phosphorus atom of the P_{66614} cation. This is due to the opposite charges of the atoms; -0.35 $(O)CO_2$ and +0.68 $(P)P_{66614}$. However, the coordination of the CO_2 is at an angle, with the *g*(r) $C(CO_2)$ peak at 5.66 Å and the second *g*(r) $(O)CO_2$ peak at 6.65 Å. This does not fit in with a directly head on approach of the CO_2, which would have yielded a peak at 5.94 Å for *g*(r) $P\text{-}C(CO_2)$ and 7.10 Å for the second peak of *g*(r) $P\text{-}(O)CO_2$. A possible explanation for this is the balance of the attractive forces between the oppositely charged P and $O(CO_2)$, the repulsive forces of the primary carbon (C1P) of the alkyl chains of the cation, which have a charge of -0.31, with the $O(CO_2)$, and the attractive forces between C1P and the positively charged $C(CO_2)$, +0.70. A graphical representation of these charges and interactions are shown in Figure 5.2.

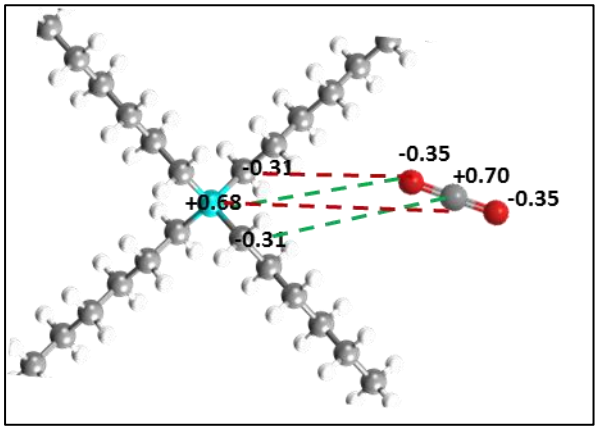

Figure 5.2. Graphical representation of the approach of a CO_2 molecule to the central phosphorus, P, of the cation P_{66614}. Displayed charges are as follows: P, +0.68; C1P, -0.31; $C(CO_2)$, +0.70; $O(CO_2)$, -0.35. Suggested attractive and repulsive forces are represented by green and red dashed line, respectively.

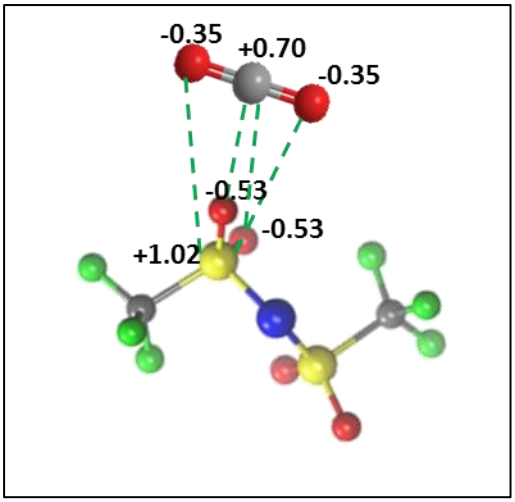

Figure 5.3. Graphical representation of the approach of a CO_2 molecule to anion NTf_2. Displayed charges are as follows: red atom O(NTf_2), -0.53; yellow atom S(NTf_2), +1.02; grey atom C(CO_2), +0.70; red atom O(CO_2), -0.35. Suggested attractive forces are represented by green dashed line.

In the NTf_2-CO_2 RDFs in Figure 5.1, we observe that the oxygen of the NTf_2 anion is the closest atom to the carbon dioxide molecule, specifically the carbon atom of the carbon dioxide. This first peak is of a high and sharp intensity around 3 Å, indicating that the CO_2 molecule does closely interact with the O(NTf_2) anion. The second major peak in the NTf_2-CO_2 RDF plots, is the N(NTf_2) – C(CO_2) RDF, which peaks at 5.3 Å. The charges are spread across the molecule as: nitrogen carrying a -0.66 charge; sulphur is +1.02; oxygen is -0.53; carbon is +0.35; and fluorine is -0.16. There are two double bonded oxygens for each sulphur, making the sulphur-oxygen bond of the molecule polar. We suggest that therefore the carbon dioxide molecule prefers to interact with the O and S of the NTf_2 anion. A graphical depiction of this suggested interaction is shown in Figure 5.3. For both the anion- and cation-CO_2 interactions, it is noted that there is medium-range order with peaks at ~11 Å.

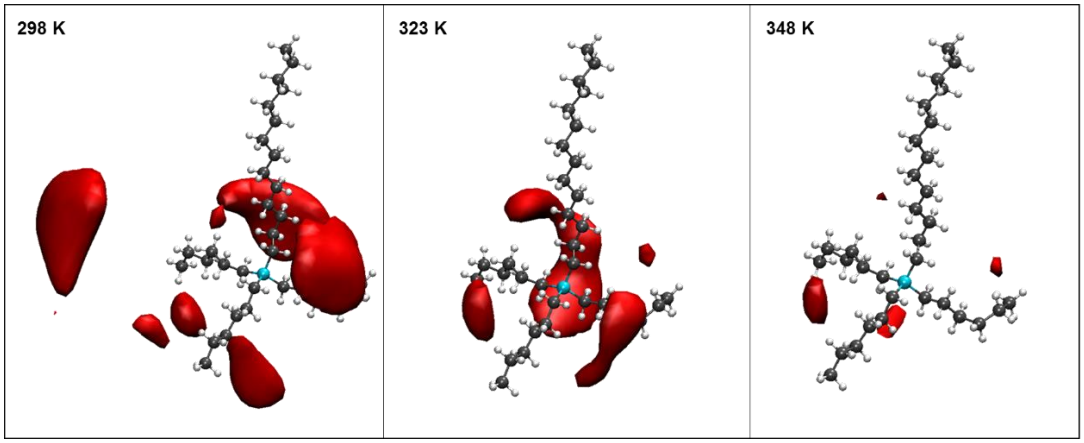

Figure 5.4. Intermolecular spatial distribution functions (SDFs) of the 50 carbon dioxide molecules around P_{66614} cation, at 3 different temperatures: 298 K, 323 K and 348 K. Isovalue of 0.26 used, reference molecule created from first time step. P is placed in the origin, C1P(1) in the x-axis, C1P(2) in the y-axis, of the reference plane.

Another tool used to describe the interactions of the IL-CO_2 is the use of pictorial spatial distribution functions (SDFs). These are presented in Figure 5.4 and Figure 5.5, and these show that with increasing temperature the probability of finding CO_2, close to the ion, decreases, a further (qualitative) reiteration of the quantitative results from the decreasing *g*(r)'s in the IL-CO_2 RDFs in Figure 5.1.

In the SDF for CO_2 around the cation (Figure 5.4), the approach of CO_2 can be in between any alkyl chains at T = 298 K, with the furthest left segment of isosurface representing the second coordination shell of the P_{66614}-**C**O_2 RDF in Figure 5.1. Furthermore, the isosurfaces at 323 K and 348 K seem to show some mirroring in approach; the probabilities of CO_2 approach in the equivalent region between the alkyl chains, depicted more clearly with smaller isosurfaces. Overall, we do observe that the interactions of the P-CO_2 are less pronounced than the interactions between N-CO_2, and this can be explained by the steric hindrance presented by the alkyl chains of the phosphonium cation.

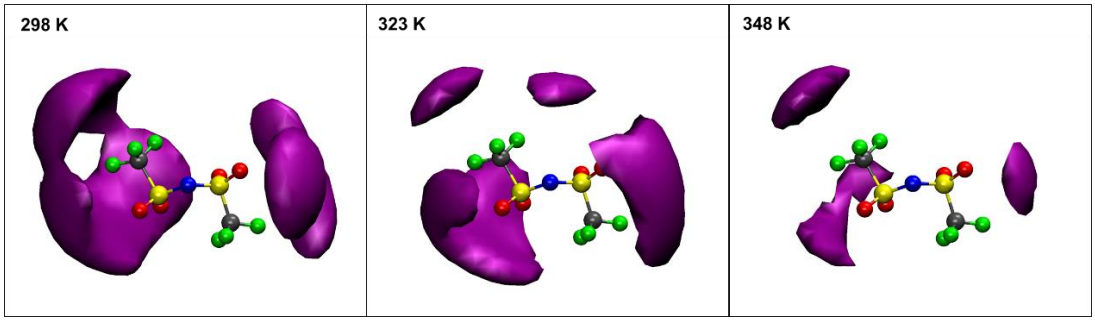

Figure 5.5. Intermolecular spatial distribution functions (SDFs) of the 50 carbon dioxide molecules around the anion, NTf_2, at 3 different temperatures: 298 K, 323 K and 348 K. Isovalue of 0.26 used, reference molecule created from first time step, which is in the "trans" configuration. N is placed in the origin, S(1) in the x-axis, O(1) in the y-axis, of the reference plane.

As expected, the isosurfaces shown in Figure 5.5, agree with the assertion that the CO_2 approaches the NTf_2 molecule around the S=O bonds. Moreover, whilst the reference molecule is in the *trans* configuration, this does not preclude the possibility of the *cis* configuration being existent in the simulation, thus explaining the rounded isosurface. The hole in the isosurface in this SDF at 298 K, also reinforces the idea that the coordination of the CO_2 molecule is with the S=O bonds as depicted in Figure 5.3, as it shows there is little probability of the CO_2 molecule approaching the NTF_2 molecule in the plane of the molecule, along the S-N-S angle.

To further explore the *cis*/*trans* behaviour of the NTf_2 anion with respect to the approach of the CO_2, a combined distribution function (CDF) was calculated with both the RDF of the O(NTf_2)-C(CO_2) distance and the C-S---S-C dihedral distribution function to describe the cis/trans behaviour of the anion. This analysis is presented in Figure 5.6.

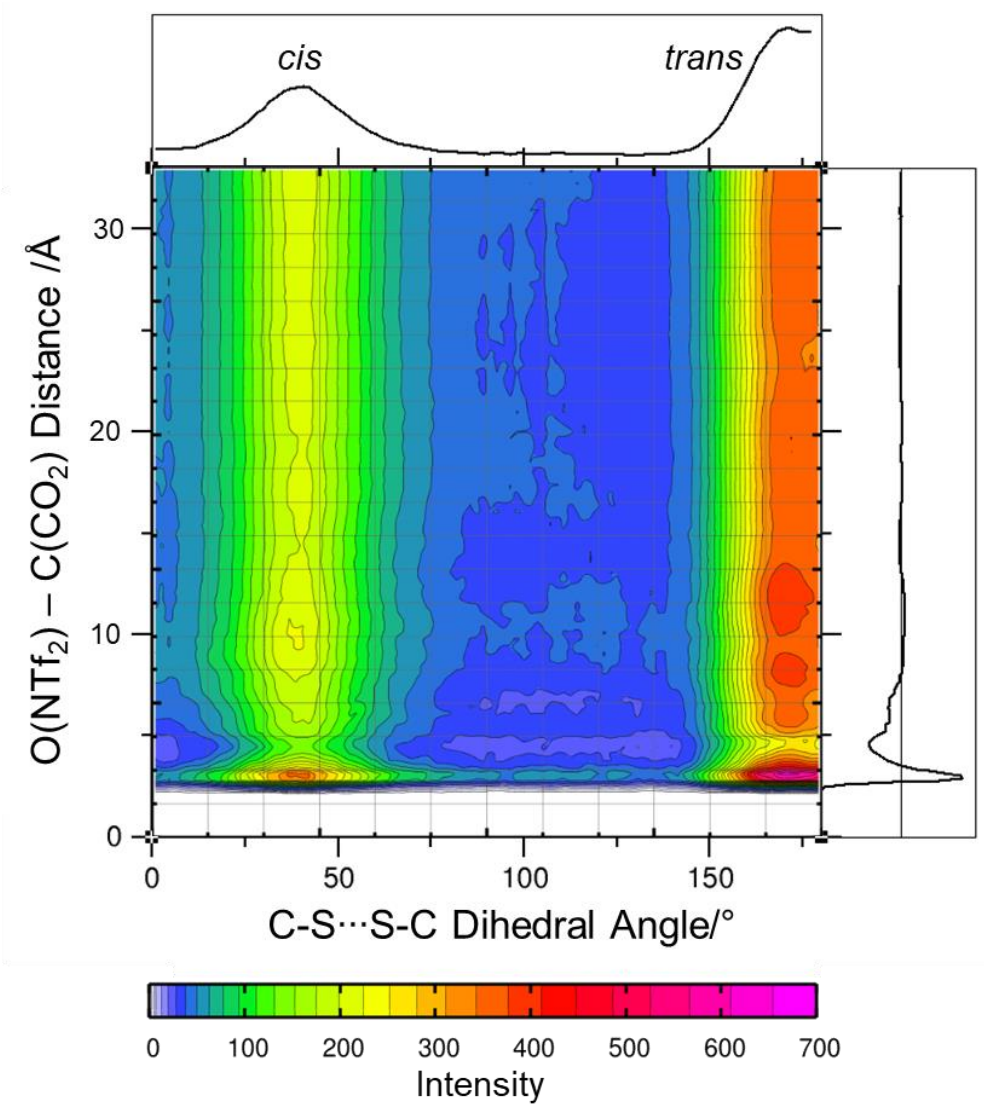

Figure 5.6. Combined radial/dihedral distribution function for $O(NTf_2)$-$C(CO_2)$ distance with C-S---S-C dihedral in NTf_2, at T = 298 K. The coloured intensity scale is a combination of g(r) for RDF and DDF *i.e.* higher on the intensity scale shows a higher occurrence.

As we have observed that the CO_2 coordinates closer to the anion than the cation, some further analysis was carried out on the anion-CO_2 interaction. A key observation made from the CDF in Figure 5.6 is that much of the CO_2 coordination with the anion is when the anion is in the *trans* configuration. Subsequently, a comparison of the cis/trans ratio, with and without CO_2 is depicted with dihedral distribution functions compared in Figure 5.7.

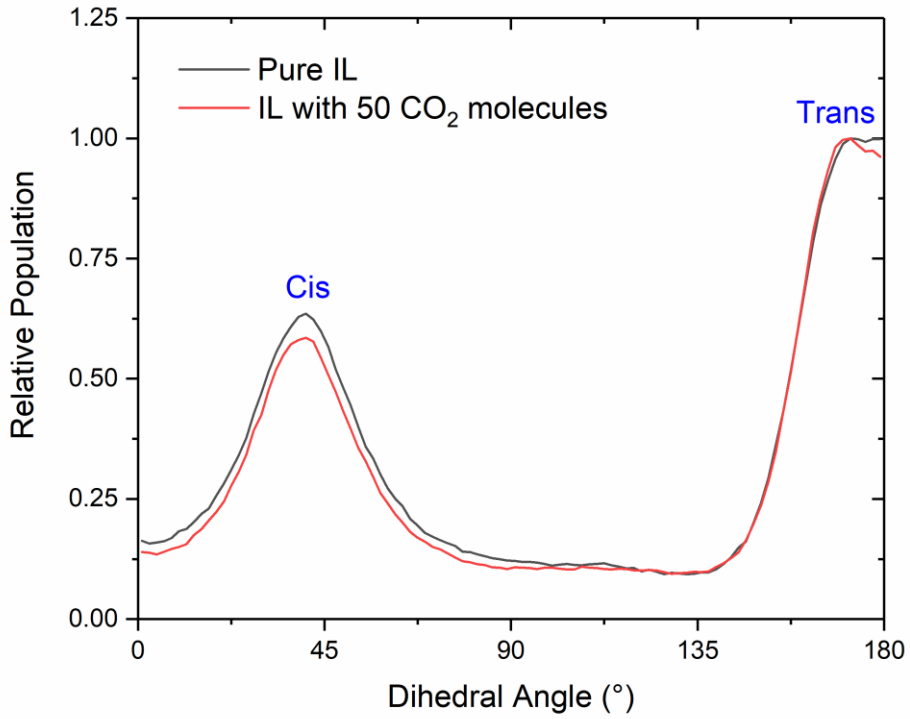

Figure 5.7. Distribution of the C-S···S-C dihedral angle as a function of the number of anions in pure IL $[P_{66614}][NTf_2]$ (black line) and IL with 50 CO_2 molecules (red line), at T = 298 K.

It is noted that the presence of 50 CO_2 molecules does, in fact, alter the cis: *trans* ratio at T = 298 K, by slightly decreasing the *cis* configuration relative to trans. The *cis* configuration is not at 0°, and in fact is just under 45°. The CO_2 may be interacting with some of the anions in a 2:1 ratio, which would explain the slight decrease in the *cis* configuration for the CO_2 molecules to approach on opposite sides of the molecule.

5.3.2 Structural and Diffusive Changes in $[P_{66614}][NTf_2]$ Induced by Carbon Dioxide Absorption

To study the influence of CO_2 absorption on the overall IL structure, RDFs were determined for the IL structure, pure and with CO_2, to be compared (counter) to each other. These results are shown in Figure 5.8. Previous simulation studies on imidazolium based ILs,[42], [73], [130], observed no significant structural changes induced by CO_2 presence. For the most part, these studies reported cation-anion RDFs, whilst here we have also compared the like-ion RDFs.

Overall, we do observe no significant structural changes in the basic underlying cation-anion structure, at least not in the first coordination sphere, with any changes being negligible. Nevertheless, we do observe notable qualitative differences in the anion-anion and cation-cation RDFs. Principally, there is a difference seen in the first coordination sphere in both P_{66614}-P_{66614} and NTf_2-NTf_2 RDFs, more noticeably in the cation-cation plot. These like-ion RDFs show a long-range order for all loadings of CO_2, and here we observe further differences induced by the presence of CO_2.

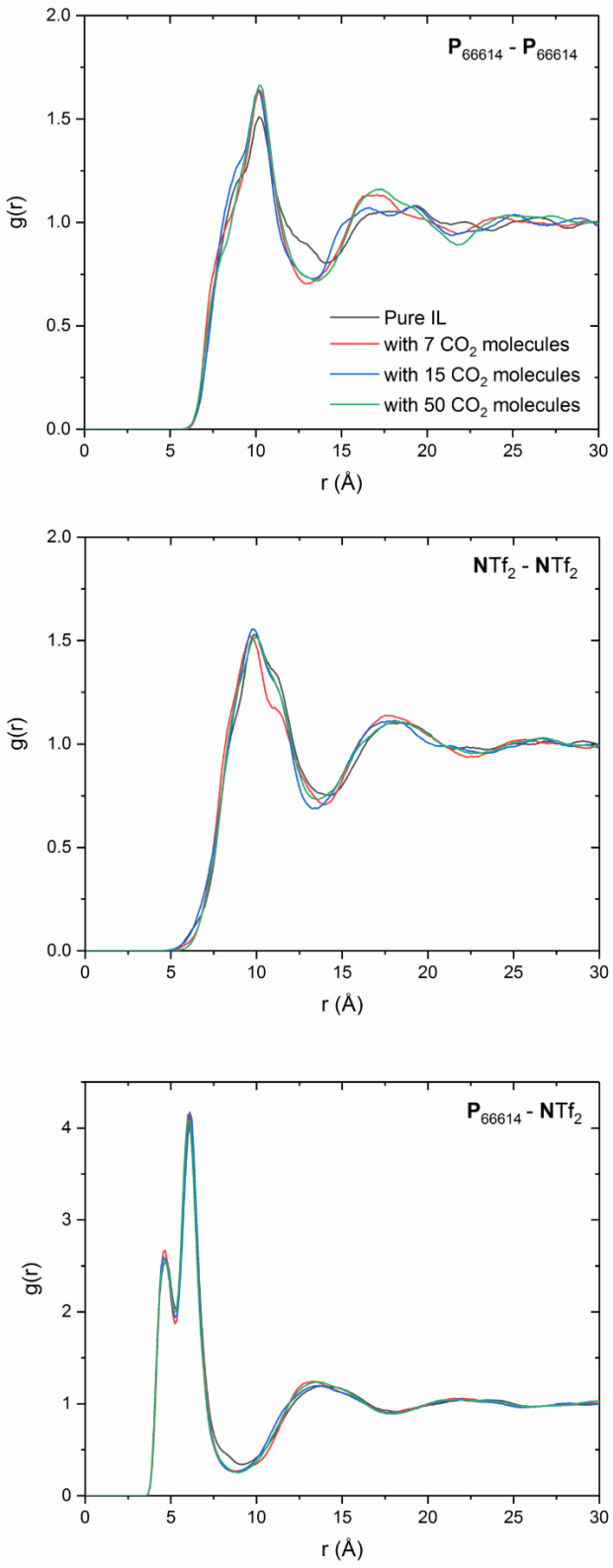

Figure 5.8. Site-site intermolecular radial distribution functions to compare pure IL $[P_{66614}][NTf_2]$ (black lines), IL with 7 CO_2 molecules (red lines), with 15 CO_2 molecules (blue lines) and with 50 CO_2 (green line) at T = 298 K.

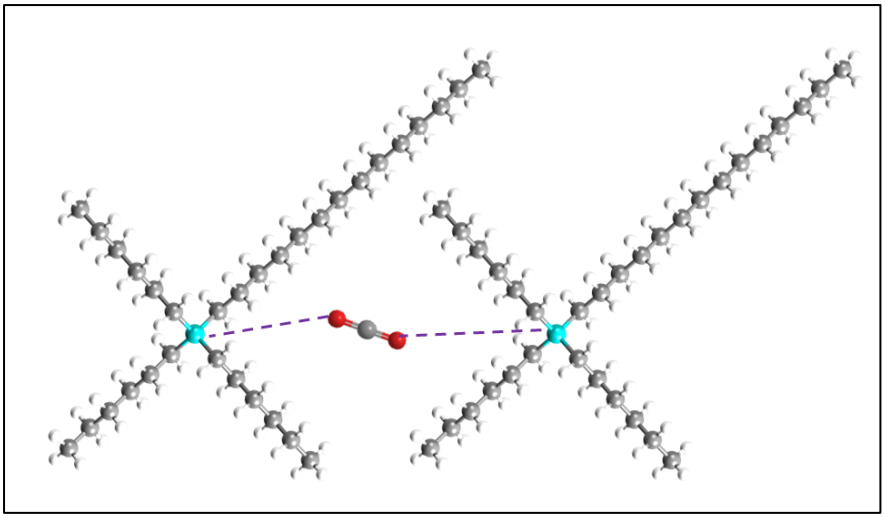

Figure 5.9. Graphical representation of the effect of a CO_2 molecule presence on the cation-cation interaction, P_{66614}-P_{66614}.

In the cation-cation, P_{66614}-P_{66614}, RDF we observe an increase in the first coordination peak g(r) by ~0.1, with as little as 7 CO_2 molecules in the system. This can be explained by the oxygens of the CO_2 molecule interacting with the positively charged phosphorus of two cations at the same time and thus slightly decreasing the distance between two cations compared to a pure IL system. This is illustratively shown in Figure 5.9.

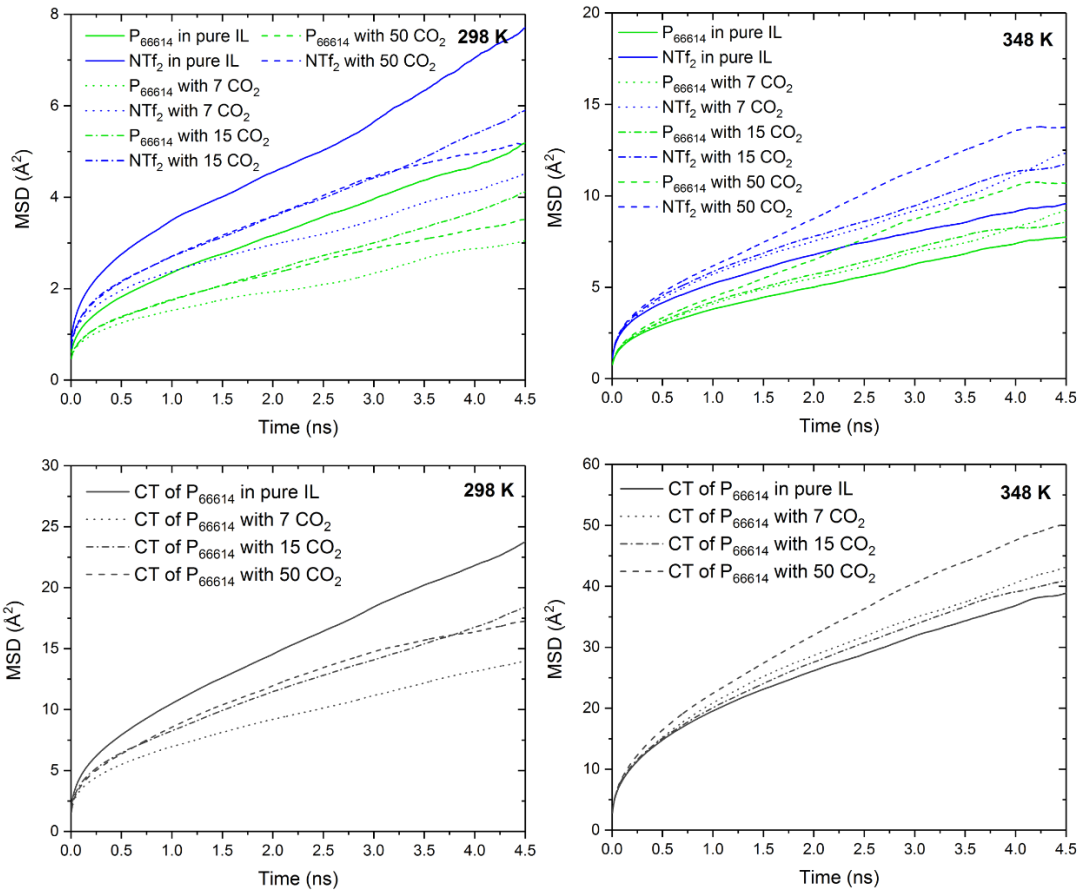

Figure 5.10. Top. Mean square displacement of phosphorus (P, blue plots) in cation $[P_{66614}]$ and nitrogen (N, green plots) atoms of anion $[NTf_2]$, at temperatures 298 and 348 K. **Bottom.** Mean square displacement of terminal carbons (CT, grey plots) in cation $[P_{66614}]$, at T = 298 and 348 K.

Diffusion of the IL in these systems have been calculated from the mean square displacements (MSDs), of the phosphorus (P) and terminal carbon (CT) of the cation $[P_{66614}]$, and the nitrogen (N) of the anion $[NTf_2]$, at temperatures 298 and 348 K. From to the MSD plots depicted in Figure 5.10, it can be deduced that at T = 298 K, all three atom types are slowed down by the presence of CO_2 molecules. The system with 7 CO_2 molecules shows the slowest dynamics of the 4 systems, with the 15 and 50 CO_2 systems showing similar diffusivity to each other, that is an intermediate between the pure IL and the 7 CO_2 system's dynamics.

Conversely, at T = 348 K, the presence of the CO_2 is shown to increase the diffusivity of the IL atom types. In this instance, the 50 CO_2 system has the largest effect on the IL dynamics, speeding up the ions the most, with the 7 and 15 CO_2 systems' showing similar diffusivity.

An explanation for this would be that at T = 298 K, the CO_2 molecules coordinate more permanently with the ions in the IL resulting in more sluggish dynamics for the IL. On the other hand, at a higher temperature, the CO_2 molecules would have enough energy to move and interact in different configurations within the IL structure. These interactions between the CO_2 molecules and the ions would be less strong thus fitting in with the the structural deductions made in section, 5.3.1, specifically, the reduction of the g(r)'s in the RDFs (Figure 5.1) and the smaller isosurfaces in the SDFs (Figure 5.4 and Figure 5.5) at higher temperatures.

5.3.3 Diffusion of Carbon Dioxide

To investigate the gas transport of the carbon dioxide, a self-diffusivity analysis was carried out on the MD simulations; MSDs were calculated for the CO_2 molecules, using the C as the central site. Figure 5.11 compares the MSDs of the carbon dioxide in the systems of different loading, 7, 15 and 50 CO_2 molecules, at temperatures ranging from 298 K to 398 K with increments of 25 K. We observe that as we increase temperature, we increase the diffusivity of all the CO_2 molecules, in every loading. This is expected with increasing kinetic energy at the higher temperatures.

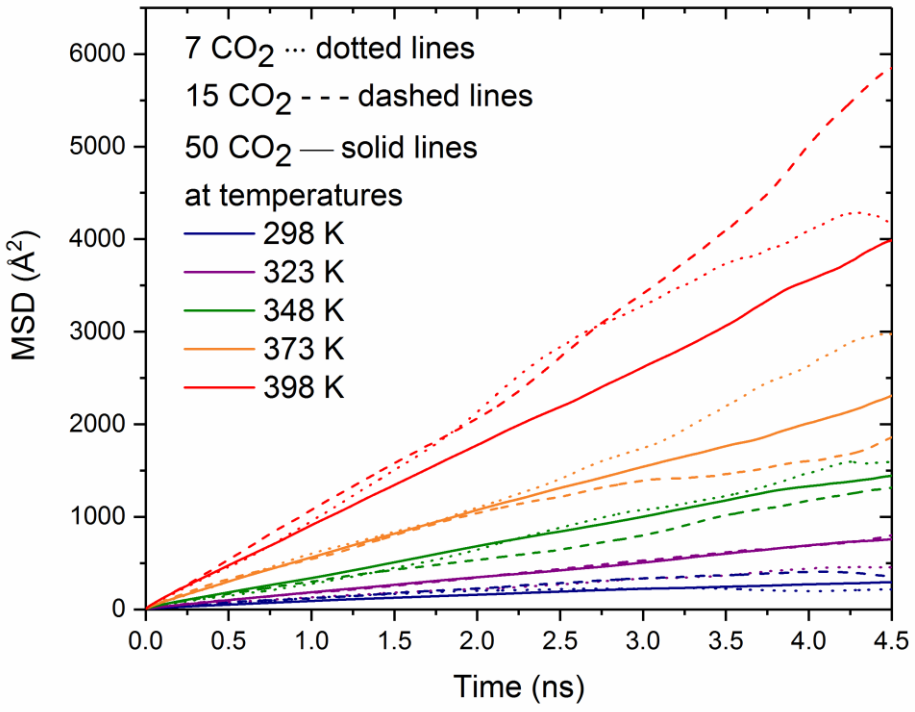

Figure 5.11. Mean square displacements of CO_2 molecules at the three different loadings of CO_2: 7 (dotted lines), 15 (dashed lines) and 50 (solid lines); at T = 298, 323, 348, 373 and 398 K.

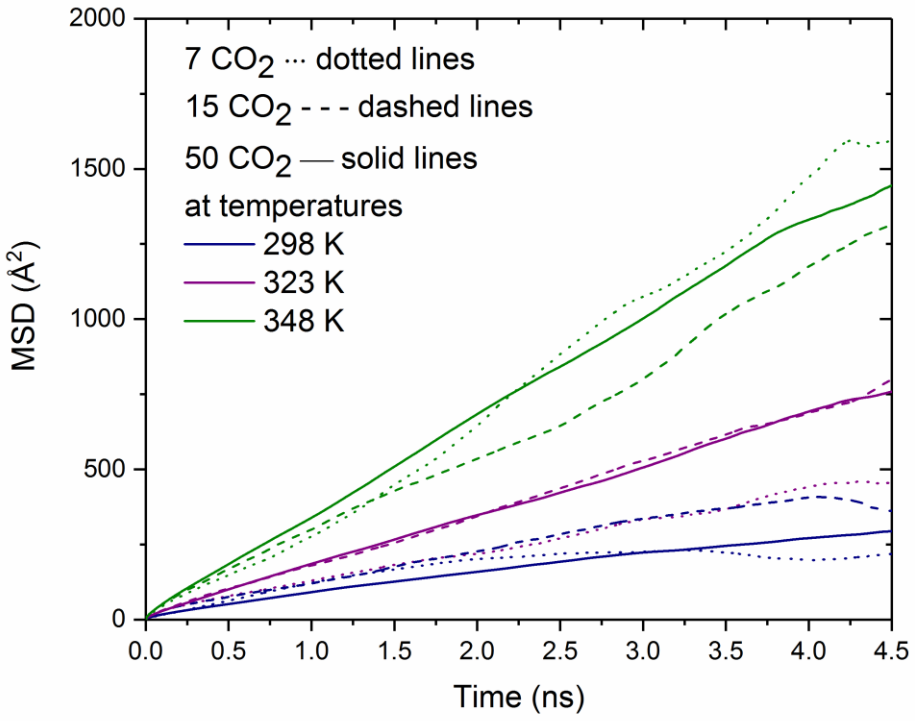

Figure 5.12. Mean square displacement of CO_2 molecules at the three different loadings of CO_2: 7 (dotted lines), 15 (dashed lines) and 50 (solid lines); at T = 298, 323, 348 K.

To compare the cooler temperature MSDs more closely, Figure 5.12 shows enlarged plots of the MSDs at temperatures 298, 323 and 348 K. We observe that the 50 CO_2 system shows dynamics that are consistent throughout the simulation; depicting good linearity in the diffusive regime. The 7 and 15 CO_2 systems demonstrate less linear behaviour. The range shown in the MSD plots match with previous simulation studies into the carbon dioxide diffusion in ILs. [97]

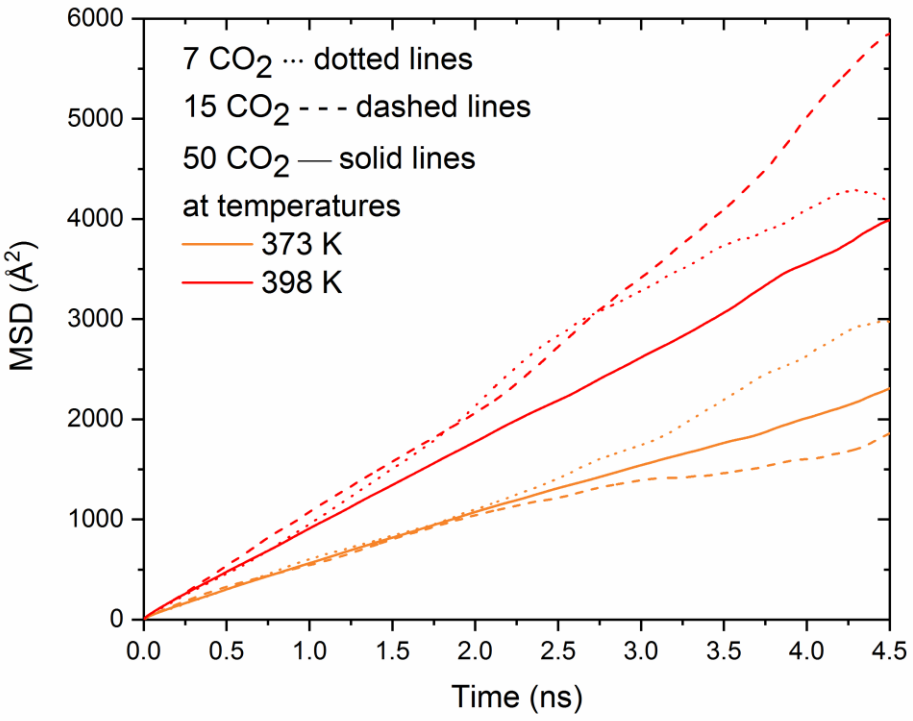

Figure 5.13. Mean square displacement of CO_2 molecules at the three different loadings of CO_2: 7 (dotted lines), 15 (dashed lines) and 50 (solid lines); *T* = 373 and 398 K.

At the higher temperatures Figure 5.13 shows enlarged plots of the MSDs at temperatures 373 and 398 K. Once again, we see the 50 CO_2 system showing good linearity in the diffusive regime, whilst the 7 and 15 CO_2 systems demonstrate less linear behaviour.

The explanation for this difference between the 7/15 CO_2 systems and the 50 CO_2 system could simply be that the statistics of calculating the MSD for 7 or 15 CO_2 molecules is poor, compared to the statistics in the MSD calculation with 50 CO_2 molecules. Nevertheless, it is important to note that the range shown in the MSD plots agree with previous simulation studies into the carbon dioxide diffusion in ILs. [45], [129]

Table 5.2. Diffusion coefficients D, × 10 -11 m^2 s^{-1}, of CO_2 molecules, in the systems of three different loadings.

Temperature (K)	**7 CO_2 molecules**	**15 CO_2 molecules**	**50 CO_2 molecules**
298	6.23	14.07	10.08
323	15.78	29.40	27.92
348	62.98	47.80	51.90
373	106.95	65.48	80.68
398	155.87	215.75	145.88

To quantitatively compare the CO_2 diffusivity, in the varying loading systems, one calculates the diffusion coefficients, Table 5.2. The diffusion coefficients show that in general the highest CO_2 diffusion is found in the 15 CO_2 system at 398 K. Moreover, all the CO_2 diffusion (even at lower temperatures) is higher than the diffusion of the IL components. The diffusion coefficients power imitates the diffusion coefficients of experimental studies of CO_2 diffusion in traditional ILs.[134]–[136]

The close to three times increase in diffusion coefficient of CO_2 in the 50 CO_2 system from T = 298 K to T = 323 K (Table 5.2) is explored further by plotting the RDFs of CO_2-CO_2 interactions and is presented in Figure 5.14.

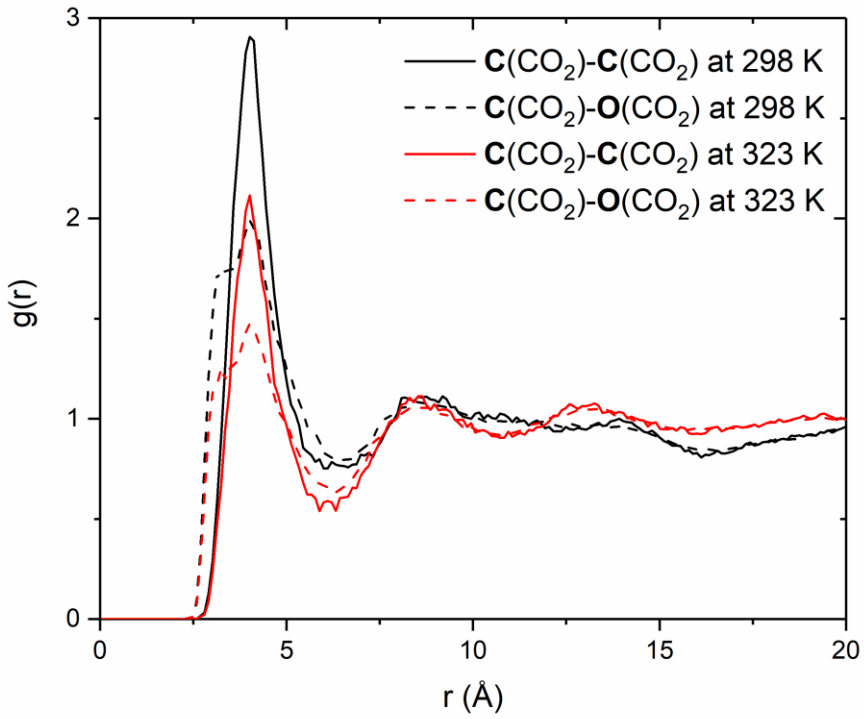

Figure 5.14. Comparison of atomic radial distribution functions between CO_2 molecules in the 50 CO_2 system at T = 298 K (black lines) and T = 323 K (red lines)

The increase in temperature has a significant and effect in both the peak intensities (decrease) and the long-range order of the CO_2-CO_2 coordination. This is explained by the increased temperature allowing for the amalgamation of the local minima to result in a more evenly dispersed system that yields a smoother RDF.

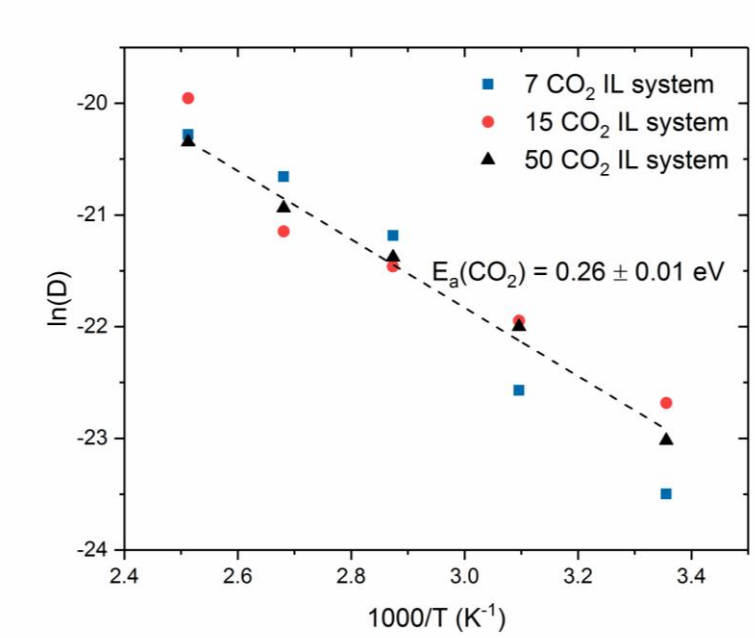

Figure 5.15. Arrhenius plot of diffusion coefficients of CO_2 in the three different loadings of CO_2: 7, 15 and 50 CO_2 molecules. Gradient and calculated activation energy of diffusion, $E_a(CO_2)$ in eV, is depicted for the 50 CO_2 plot.

Relating diffusion to activation energy of diffusion (Figure 5.15 and Table 5.3), E_a decreases with increasing CO_2 loading, indicating that higher loadings favour CO_2 migration in the system. This may be due to the increased presence of CO_2 increasing the dynamics of the IL as well as there being more cooperative movement of the CO_2.

Table 5.3. Carbon dioxide diffusion activation energies (eV) for temperature range 298 K – 398 K.

System	E_a of *D* (eV)	Error
7 CO_2 molecules	0.35	±0.03
15 CO_2 molecules	0.25	±0.03
50 CO_2 molecules	0.26	±0.01

5.3.4 A Bubble of Carbon Dioxide

In this segment, we present a short 150 ps MD simulation of a system, starting with 50 CO_2 molecules in a cluster at the centre of 250 ion pairs IL box. Using Packmol, we fixed the spherical packing of the CO_2 molecule, and the surrounding space was occupied by the cations and anions. After a short minimisation run where the sphere is fixed as a rigid body, a 150 ps MD run is calculated. Visualisations of the system at different intervals were displayed with VMD, and some key frames are snapshotted to show the behaviour of the cluster over time, Figure 5.16. The cluster is depicted to quickly diffuse out of the bubble cluster and into the IL structure.

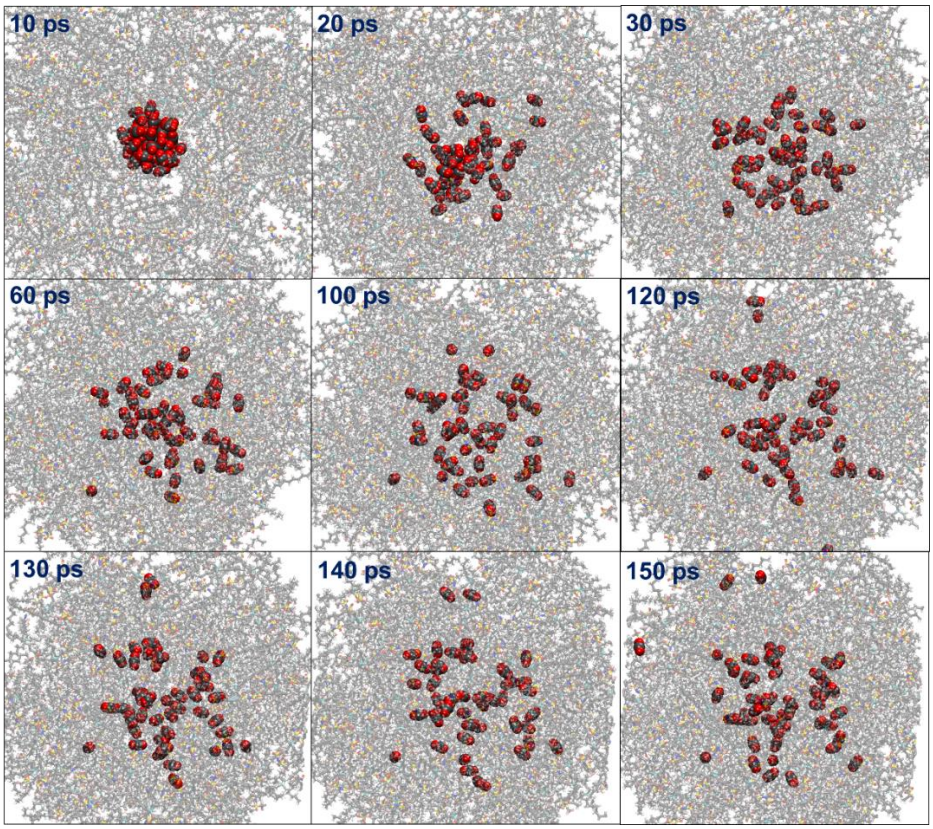

Figure 5.16. Snapshots of the simulation box using the VMD software. The box contains 250 ion pairs (displayed as dynamic bonds in transparent) with the 50 CO_2 molecules (displayed in the van der Waals representation, as glossy, carbon atoms in grey and oxygen in red).

5.4 Chapter Conclusions

In this chapter, the structural and diffusive properties of $[P_{66614}][NTF_2]$ is presented pure and with different loadings of CO_2. The coordination of CO_2 is found in closer proximity to the anion $[NTF_2]$ than the cation $[P_{66614}]$. The rationale for this is the presence of the polar S=O bond and less steric hindrance than the cation provides. Structural and diffusive changes are induced by the presence of CO_2 even at the small loading of 7 CO_2 molecules. The dynamics of the CO_2 in the system was analysed and the diffusion coefficients and activation energies were calculated.

There is no evidence of CO_2 aggregation in the systems, and even a cluster simulation saw CO_2 dispersion occur very quickly. CO_2 has a small but noticeable effect on the separation of ion pairs (but not with each pair). The diffusion of ions is noted to decrease with the addition of CO_2 at lower temperatures whilst at higher temperatures CO_2 presence sees ionic diffusion increase. It would be interesting to observe the diffusion in terms of ion pairs, for the CO_2 loadings, and the effect of increased loadings of CO_2.

Chapter 6

Concluding Remarks

6.1 Summary and Conclusions

In this thesis, a computational study of ionic liquids has been performed exploring the use as a carbon dioxide capture medium. The need for new means to capture CO_2 has been described and elucidated in Chapter 1 along with, detailing the desirable and unique features of ILs. With the vast range of ILs being researched, traditional and functionalised ILs are presented. To study the bulk properties of ILs, molecular dynamics simulations are proposed for this research project.

Primarily, the range of FFs for MD modelling of ILs are investigated in the literature, after which two FFs, CL&PFF and GAFF, are chosen for the simulating of 3 different ILs: $[P_{66614}][Cl]$, [BMIm][OAc] and [EMIm][DCA]. Experimental density ranges are well reproduced with both FFs, with CL&PFF yielding better data compared with experiment. Some similarities are seen in structures produced for all the ILs $[P_{66614}][Cl]$ and [BMIm][OAc] with both FFs but greater long range order is observed with CL&PFF. Density and structural consistency is achieved for changing simulation cell size of $[P_{66614}][Cl]$ with CL&PFF. Ultimately, the CL&PFF is selected for further modelling in this thesis.

As phosphonium-based ILs are thermally stable and economical, a systematic study of the structure and dynamics of the pure IL $[P_{66614}][NTf_2]$ is carried out. Over a range

of temperatures, simulated densities were in agreement with experimental data. When investigating the dynamics of the ions, we determine the cation diffuses slower than the anion, and that the trend in diffusivity of the simulated system is comparable to experimental viscosity. Structural distribution functions, such as RDFs, SDFs and DDFs are used to illustrate the structure of the IL at the various temperatures, and report differences, such as the increased long-range order with increasing temperature.

Lastly, simulations of pure $[P_{66614}][NTf_2]$ and $[P_{66614}][NTf_2]$ loaded with 7, 15 and 50 CO_2 are presented and evaluated. Structural and diffusive changes are induced by the presence of CO_2 even at the small loading of 7 CO_2 molecules. The dynamics of the CO_2 in the system was analysed and the diffusion coefficients and activation energies were calculated. We report an increase in CO_2 diffusivity with increased loading and there is no evidence of CO_2 aggregation in the systems. The diffusion of ions is noted to decrease with the addition of CO_2 at lower temperatures whilst at higher temperatures CO_2 presence sees ionic diffusion increase.

The research presented in this thesis aims to be both predictive and elucidating to experimental research, for the bulk properties of ILs along with the interactions with CO_2.

6.2 Ongoing Work

To follow on from the above work, a superbase IL system is considered for the aim of investigating the use of the CL&PFF for the tetra-alkyl phosphonium cation crossed over with Wu and Maginn's potential parameters for superbase anions,[45] specifically benzimidazolide, [Benzim] (parameters are detailed in Appendix I). Two systems have been constructed, a pure IL system with 300 ion pairs of $[P_{66614}]$[Benzim], and a 1:1 IL to CO_2 system with 300 ion pairs of IL and 300 CO_2 molecules. Charges for the cation are scaled to net +0.90 as the anion is scaled to -0.90. This was done as to approximate for charge transfer, first suggested by Chaban.[137] Chaban concluded that ionic transport was notably hindered by excessive Coulombic interactions and so suggested that uniform scaling of the electrostatic charges of all atoms improved the ionic dynamics simulated.

MD calculations were completed to 4 ns for the pure and with-CO_2 systems at 4 temperatures: 298 K, 308 K, 318 K and 328 K. Some rudimentary results from these systems are presented below. The density for the superbase across the range of temperatures is compared with experimental data, in Figure 6.1. Here we see that simulated density is underestimated compared to the experimental, in contradiction to the work presented here in Chapter 3 and 4, along with previous simulation studies.

To visually compare the pure and with-CO_2 system, Figure 6.2 shows the IL structure focusing on the phosphorus (cation) and nitrogen (anion), for the pure and the CO_2 system. It appears the IL structure forms channels for CO_2 sorption/presence.

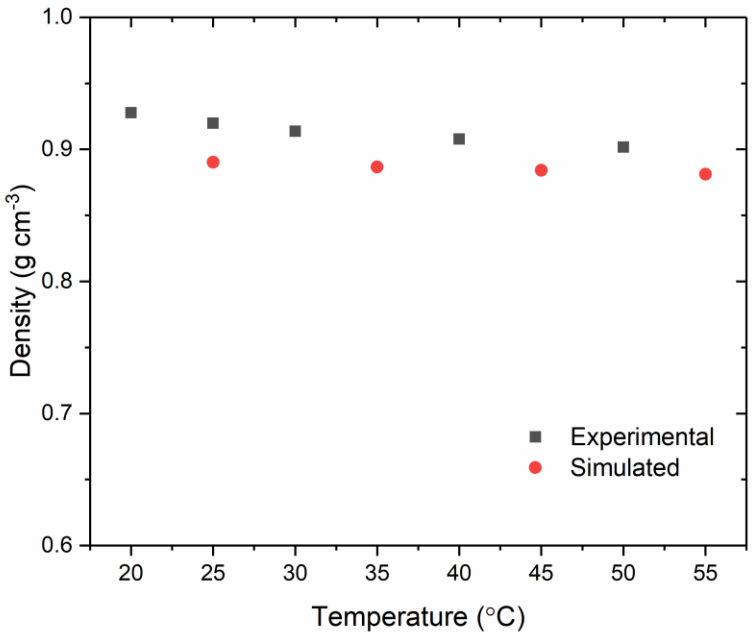

Figure 6.1. Simulated and experimental densities, g cm^{-3}, of $[P_{66614}]$[Benzim] shown as a function of temperature, °C.

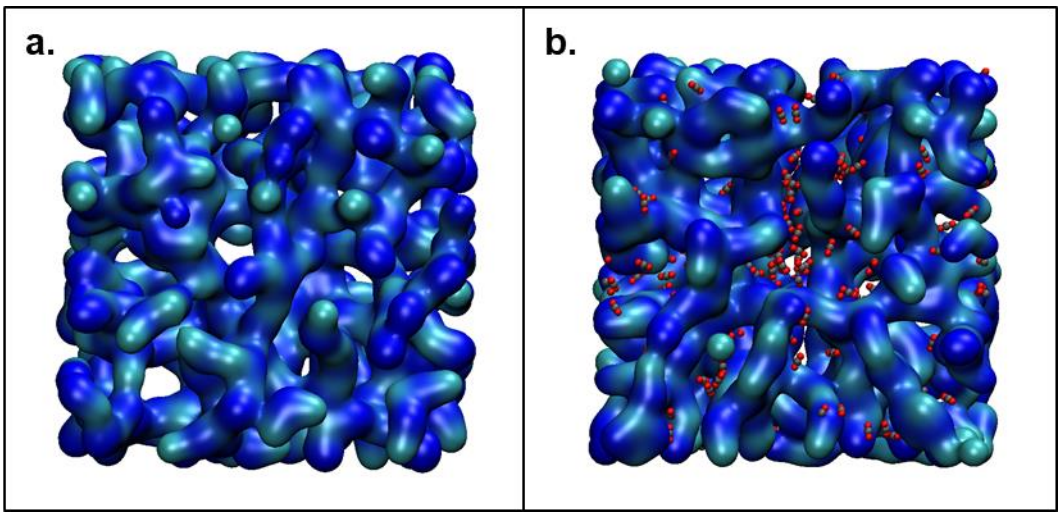

Figure 6.2. Snapshot of final configurations of pure P_{66614}Benzim (a.) and system of 1:1 P_{66614}Benzim: CO_2 (b.) at 298 K. Phosphorus of the cation (cyan) and nitrogen of the anion (blue) of IL shown in Surf visualisation of VMD, with CO_2 shown in grey (carbon) and red (oxygen).

Further analysis could be carried out on the pure and CO_2 system to calculate diffusivity and structural properties. Comparing the phosphorus diffusivity between the $[P_{66614}][NTf_2]$ and $[P_{66614}]$[Benzim] systems would also test if Chaban's technique does in deed improve the ionic transport.

6.3 Future Work

1. With Maginn's group having parameterised other superbase anions, combining the $[P_{66614}]$ cation with these would demonstrate a systematic characterising of a range of $[P_{66614}]$-suberbase ILs.
2. Additionally, IL systems with water are worthwhile to investigate as less is known about the impact of water in these superbase ILs.
3. Maginn also parameterised the superbase anions with CO_2 chemically bound to the aprotic anions (superbase), which would be an interesting variation to the pure IL/ IL with free CO_2 systems.
4. Another mixture system of interest would be an IL/monoethanolamine (MEA) system; MEA/IL systems have been reported to be beneficial in increasing CO_2 capacity and decrease changes in viscosity.

Bibliography

[1] J. Blunden and D. S. Arndt, “State of the Climate in 2016,” *Bull. Am. Meteorol. Soc.*, vol. 98, no. 8, pp. Si-S280, 2017.

[2] J. Hansen, M. Sato, R. Ruedy, K. Lo, D. W. Lea, and M. Medina-Elizade, “Global temperature change,” *Proc. Natl. Acad. Sci.*, vol. 103, no. 39, pp. 14288–14293, 2006.

[3] A. E. funded P. Grant, “A Comprehensive and Coordinate Approach to Carbon Capture and Utilisation (4CU),” 2012. [Online]. Available: http://4cu.org.uk/.

[4] S. Nanda, S. N. Reddy, S. K. Mitra, and J. A. Kozinski, “The progressive routes for carbon capture and sequestration,” *Energy Sci. Eng.*, vol. 4, no. 2, pp. 99–122, Mar. 2016.

[5] Y. Wang, L. Zhao, A. Otto, M. Robinius, and D. Stolten, “A Review of Post-combustion CO_2 Capture Technologies from Coal-fired Power Plants,” *Energy Procedia*, vol. 114, pp. 650–665, 2017.

[6] G. T. Rochelle, “Amine Scrubbing for CO_2 Capture,” *Science (80-.).*, vol. 325, no. 5948, pp. 1652–1654, 2009.

[7] D. M. D’Alessandro, B. Smit, and J. R. Long, “Carbon Dioxide Capture: Prospects for New Materials,” *Angew. Chemie Int. Ed.*, vol. 49, no. 35, pp. 6058–6082, 2010.

[8] M. Ramdin, T. W. de Loos, and T. J. H. Vlugt, “State-of-the-Art of CO_2 Capture with Ionic Liquids,” *Ind. Eng. Chem. Res.*, vol. 51, no. 24, pp. 8149–8177, 2012.

[9] S. Zhang, X. Ye, and Y. Lu, “Development of a Potassium Carbonate-based Absorption Process with Crystallization-enabled High-pressure Stripping for

CO_2 Capture: Vapor–liquid Equilibrium Behavior and CO_2 Stripping Performance of Carbonate/Bicarbonate Aqueous Systems," *Energy Procedia*, vol. 63, pp. 665–675, 2014.

[10] R. S. Haszeldine, "Carbon Capture and Storage: How Green Can Black Be?," *Science (80-.).*, vol. 325, no. 5948, p. 1647 LP-1652, Sep. 2009.

[11] Z. Zhang, Z.-Z. Yao, S. Xiang, and B. Chen, "Perspective of Microporous Metal-Organic Frameworks for CO_2 Capture and Separation," *Energy Environ. Sci.*, 2014.

[12] R. Krishna and J. M. van Baten, "A comparison of the CO_2 capture characteristics of zeolites and metal–organic frameworks," *Sep. Purif. Technol.*, vol. 87, no. 0, pp. 120–126, 2012.

[13] L. A. Blanchard, D. Hancu, E. J. Beckman, and J. F. Brennecke, "Green processing using ionic liquids and CO_2," *Nature*, vol. 399, no. 6731, pp. 28–29, 1999.

[14] K. R. Seddon, "Ionic liquids: A taste of the future," *Nat Mater*, vol. 2, no. 6, pp. 363–365, 2003.

[15] M. Freemantle, *An introduction to ionic liquids*. Royal Society of chemistry, 2010.

[16] J. L. Anderson, J. K. Dixon, E. J. Maginn, and J. F. Brennecke, "Measurement of SO_2 Solubility in Ionic Liquids," *J. Phys. Chem. B*, vol. 110, no. 31, pp. 15059–15062, 2006.

[17] A. Martinelli, "Ionic Liquids for Green Energy Applications - Local Structure and Dynamics by Advanced Spectroscopic Techniques," J. B. T.-I. L.-N. A. for the F. Kadokawa, Ed. Rijeka: InTech, 2013, pp. Ch. 09.

[18] J. S. Wilkes, "A short history of ionic liquids-from molten salts to neoteric

solvents," *Green Chem.*, vol. 4, no. 2, pp. 73–80, 2002.

[19] M. J. Earle and K. R. Seddon, "Ionic liquids. Green solvents for the future," *Pure Appl. Chem.*, vol. 72, no. 7, pp. 1391–1398, 2000.

[20] D. R. MacFarlane *et al.*, "Energy Applications of Ionic Liquids," *Energy Environ. Sci.*, vol. 7, no. 1, pp. 232–250, 2014.

[21] H. Zhao and S. V Malhotra, "Applications of Ionic Liquids in organic synthesis," *Aldrichimica Acta*, vol. 35, no. 3, pp. 75–83, 2002.

[22] S. Dai, Y. H. Ju, and C. E. Barnes, "Solvent extraction of strontium nitrate by a crown ether using room-temperature ionic liquids [dagger]," *J. Chem. Soc. Dalt. Trans.*, no. 8, pp. 1201–1202, 1999.

[23] J. G. Huddleston, H. D. Willauer, R. P. Swatloski, A. E. Visser, and R. D. Rogers, "Room temperature ionic liquids as novel media for 'clean' liquid-liquid extraction," *Chem. Commun.*, no. 16, pp. 1765–1766, 1998.

[24] N. D. Khupse and A. Kumar, "Ionic liquids: New materials with wide applications," *Indian J. Chem. Sect. A, Inorganic, bio-inorganic, Phys. Theor. Anal. Chem.*, vol. 49, no. 5, p. 635, 2010.

[25] N. V Plechkova and K. R. Seddon, "Applications of ionic liquids in the chemical industry," *Chem. Soc. Rev.*, vol. 37, no. 1, pp. 123–150, 2008.

[26] X. Zhang, X. Zhang, H. Dong, Z. Zhao, S. Zhang, and Y. Huang, "Carbon capture with ionic liquids: overview and progress," *Energy Environ. Sci.*, vol. 5, no. 5, pp. 6668–6681, 2012.

[27] A. E. Visser, J. D. Holbrey, and R. D. Rogers, "Hydrophobic ionic liquids incorporating N-alkylisoquinolinium cations and their utilization in liquid-liquid separations," *Chem Commun*, no. 23, pp. 2484–2485, 2001.

[28] A. E. Visser *et al.*, “Task-specific ionic liquids for the extraction of metal ions from aqueous solutions,” *Chem. Commun.*, no. 1, pp. 135–136, 2001.

[29] E. D. Bates, R. D. Mayton, I. Ntai, and J. H. Davis, “CO_2 Capture by a Task-Specific Ionic Liquid,” *J. Am. Chem. Soc.*, vol. 124, no. 6, pp. 926–927, 2002.

[30] L. M. Galán Sánchez, G. W. Meindersma, and A. B. de Haan, “Solvent Properties of Functionalized Ionic Liquids for CO_2 Absorption,” *Chem. Eng. Res. Des.*, vol. 85, no. 1, pp. 31–39, 2007.

[31] J. Zhang, S. Zhang, K. Dong, Y. Zhang, Y. Shen, and X. Lv, “Supported Absorption of CO_2 by Tetrabutylphosphonium Amino Acid Ionic Liquids,” *Chem. – A Eur. J.*, vol. 12, no. 15, pp. 4021–4026, 2006.

[32] K. Fukumoto, Y. Kohno, and H. Ohno, “Chiral Stability of Phosphonium-type Amino Acid Ionic Liquids,” *Chem. Lett.*, vol. 35, no. 11, pp. 1252–1253, 2006.

[33] K. Fukumoto, M. Yoshizawa, and H. Ohno, “Room Temperature Ionic Liquids from 20 Natural Amino Acids,” *J. Am. Chem. Soc.*, vol. 127, no. 8, pp. 2398–2399, 2005.

[34] B. E. Gurkan *et al.*, “Equimolar CO_2 Absorption by Anion-Functionalized Ionic Liquids,” *J. Am. Chem. Soc.*, vol. 132, no. 7, pp. 2116–2117, 2010.

[35] B. F. Goodrich *et al.*, “Experimental Measurements of Amine-Functionalized Anion-Tethered Ionic Liquids with Carbon Dioxide,” *Ind. Eng. Chem. Res.*, vol. 50, no. 1, pp. 111–118, 2010.

[36] B. F. Goodrich *et al.*, “Effect of Water and Temperature on Absorption of CO_2 by Amine-Functionalized Anion-Tethered Ionic Liquids,” *J. Phys. Chem. B*, vol. 115, no. 29, pp. 9140–9150, 2011.

[37] K. E. Gutowski and E. J. Maginn, “Amine-Functionalized Task-Specific Ionic Liquids: A Mechanistic Explanation for the Dramatic Increase in Viscosity upon

Complexation with CO_2 from Molecular Simulation," *J. Am. Chem. Soc.*, vol. 130, no. 44, pp. 14690–14704, 2008.

[38] D. Chinn, D. Vu, M. Driver, and L. Boudreau, "CO_2 removal from gas using ionic liquid absorbents." Google Patents, 2005.

[39] E. J. Maginn, "Design and Evaluation of Ionic Liquids as Novel CO_2 Absorbents," University of Notre Dame , 2005.

[40] M. B. Shiflett, D. J. Kasprzak, C. P. Junk, and A. Yokozeki, "Phase behavior of Carbon dioxide and [bmim][Ac] mixtures," *J. Chem. Thermodyn.*, vol. 40, no. 1, pp. 25–31, 2008.

[41] M. B. Shiflett, D. W. Drew, R. A. Cantini, and A. Yokozeki, "Carbon Dioxide Capture Using Ionic Liquid 1-Butyl-3-methylimidazolium Acetate," *Energy & Fuels*, vol. 24, no. 10, pp. 5781–5789, 2010.

[42] B. Gurkan *et al.*, "Molecular Design of High Capacity, Low Viscosity, Chemically Tunable Ionic Liquids for CO_2 Capture," *J. Phys. Chem. Lett.*, vol. 1, no. 24, pp. 3494–3499, 2010.

[43] S. Seo *et al.*, "Chemically Tunable Ionic Liquids with Aprotic Heterocyclic Anion (AHA) for CO2 Capture," *J. Phys. Chem. B*, vol. 118, no. 21, pp. 5740–5751, 2014.

[44] C. Wang, X. Luo, H. Luo, D. Jiang, H. Li, and S. Dai, "Tuning the Basicity of Ionic Liquids for Equimolar CO_2 Capture," *Angew. Chemie Int. Ed.*, vol. 50, no. 21, pp. 4918–4922, 2011.

[45] H. Wu and E. J. Maginn, "Water solubility and dynamics of CO_2 capture ionic liquids having aprotic heterocyclic anions," *Fluid Phase Equilib.*, vol. 368, no. 0, pp. 72–79, 2014.

[46] Z. Zhao, H. Dong, and X. Zhang, "The Research Progress of CO_2 Capture with

Ionic Liquids," *Chinese J. Chem. Eng.*, vol. 20, no. 1, pp. 120–129, 2012.

[47] P. Cserjési, N. Nemestóthy, and K. Bélafi-Bakó, "Gas separation properties of supported liquid membranes prepared with unconventional ionic liquids," *J. Memb. Sci.*, vol. 349, no. 1–2, pp. 6–11, 2010.

[48] P. Luis *et al.*, "Facilitated transport of CO_2 and SO_2 through Supported Ionic Liquid Membranes (SILMs)," *Desalination*, vol. 245, no. 1–3, pp. 485–493, 2009.

[49] S. Hanioka *et al.*, "CO_2 separation facilitated by task-specific ionic liquids using a supported liquid membrane," *J. Memb. Sci.*, vol. 314, no. 1–2, pp. 1–4, 2008.

[50] S. Shishatskiy, J. R. Pauls, S. P. Nunes, and K.-V. Peinemann, "Quaternary ammonium membrane materials for CO_2 separation," *J. Memb. Sci.*, vol. 359, no. 1–2, pp. 44–53, 2010.

[51] L. A. Neves, J. G. Crespo, and I. M. Coelhoso, "Gas permeation studies in supported ionic liquid membranes," *J. Memb. Sci.*, vol. 357, no. 1–2, pp. 160–170, 2010.

[52] Y.-I. Park, B.-S. Kim, Y.-H. Byun, S.-H. Lee, E.-W. Lee, and J.-M. Lee, "Preparation of supported ionic liquid membranes (SILMs) for the removal of acidic gases from crude natural gas," *Desalination*, vol. 236, no. 1–3, pp. 342–348, 2009.

[53] R. E. Baltus *et al.*, "Examination of the potential of ionic liquids for gas separations," *Sep. Sci. Technol.*, vol. 40, no. 1–3, pp. 525–541, 2005.

[54] Y. Moriya, T. Sasaki, and T. Yanase, "Gas collection method and apparatus therefor." Google Patents, 2007.

[55] D. D. Iarikov, P. Hacarlioglu, and S. T. Oyama, "Supported room temperature ionic liquid membranes for CO2/CH4 separation," *Chem. Eng. J.*, vol. 166, no.

1, pp. 401–406, 2011.

[56] P. Scovazzo, J. Kieft, D. A. Finan, C. Koval, D. DuBois, and R. Noble, “Gas separations using non-hexafluorophosphate $[PF_6]^-$ anion supported ionic liquid membranes,” *J. Memb. Sci.*, vol. 238, no. 1–2, pp. 57–63, 2004.

[57] J. E. Bara *et al.*, “Gas separations in fluoroalkyl-functionalized room-temperature ionic liquids using supported liquid membranes,” *Chem. Eng. J.*, vol. 147, no. 1, pp. 43–50, 2009.

[58] J. Tang, W. Sun, H. Tang, M. Radosz, and Y. Shen, “Enhanced CO_2 absorption of poly (ionic liquid) s,” *Macromolecules*, vol. 38, no. 6, pp. 2037–2039, 2005.

[59] J. Tang, H. Tang, W. Sun, M. Radosz, and Y. Shen, “Low-pressure CO_2 sorption in ammonium-based poly(ionic liquid)s,” *Polymer (Guildf).*, vol. 46, no. 26, pp. 12460–12467, 2005.

[60] S. P. M. Ventura *et al.*, “High pressure solubility data of carbon dioxide in (tri-iso-butyl(methyl)phosphonium tosylate&water) systems,” *J. Chem. Thermodyn.*, vol. 40, no. 8, pp. 1187–1192, 2008.

[61] D. Camper, J. E. Bara, D. L. Gin, and R. D. Noble, “Room-Temperature Ionic Liquid−Amine Solutions: Tunable Solvents for Efficient and Reversible Capture of CO_2” *Ind. Eng. Chem. Res.*, vol. 47, no. 21, pp. 8496–8498, 2008.

[62] Z. Feng, F. Cheng-Gang, W. You-Ting, W. Yuan-Tao, L. Ai-Min, and Z. Zhi-Bing, “Absorption of CO_2 in the aqueous solutions of functionalized ionic liquids and MDEA,” *Chem. Eng. J.*, vol. 160, no. 2, pp. 691–697, 2010.

[63] Y. Zhao *et al.*, “Density, Viscosity, and Performances of Carbon Dioxide Capture in 16 Absorbents of Amine + Ionic Liquid + H_2O, Ionic Liquid + H_2O, and Amine + H_2O Systems,” *J. Chem. Eng. Data*, vol. 55, no. 9, pp. 3513–3519, 2010.

[64] C. Wang, S. M. Mahurin, H. Luo, G. A. Baker, H. Li, and S. Dai, “Reversible and robust CO_2 capture by equimolar task-specific ionic liquid-superbase mixtures,” *Green Chem.*, vol. 12, no. 5, pp. 870–874, 2010.

[65] R. M. Lynden-Bell *et al.*, “Simulations of Ionic Liquids, Solutions, and Surfaces,” *Acc. Chem. Res.*, vol. 40, no. 11, pp. 1138–1145, 2007.

[66] E. J. Maginn, “Molecular simulation of ionic liquids: current status and future opportunities,” *J. Phys. Condens. Matter*, vol. 21, no. 37, p. 373101, 2009.

[67] C. G. Hanke, S. L. Price, and R. M. Lynden-Bell, “Intermolecular potentials for simulations of liquid imidazolium salts,” *Mol. Phys.*, vol. 99, no. 10, pp. 801–809, 2001.

[68] C. G. Hanke, N. A. Atamas, and R. M. Lynden-Bell, “Solvation of small molecules in imidazolium ionic liquids: a simulation study,” *Green Chem.*, vol. 4, no. 2, pp. 107–111, 2002.

[69] J. K. Shah, J. F. Brennecke, and E. J. Maginn, “Thermodynamic properties of the ionic liquid 1-n-butyl-3-methylimidazolium hexafluorophosphate from Monte Carlo simulations,” *Green Chem.*, vol. 4, no. 2, pp. 112–118, 2002.

[70] T. I. Morrow and E. J. Maginn, “Molecular Dynamics Study of the Ionic Liquid 1-n-Butyl-3-methylimidazolium Hexafluorophosphate,” *J. Phys. Chem. B*, vol. 106, no. 49, pp. 12807–12813, 2002.

[71] J. de Andrade, E. S. Böes, and H. Stassen, “Computational Study of Room Temperature Molten Salts Composed by 1-Alkyl-3-methylimidazolium CationsForce-Field Proposal and Validation,” *J. Phys. Chem. B*, vol. 106, no. 51, pp. 13344–13351, 2002.

[72] C. J. Margulis, H. A. Stern, and B. J. Berne, “Computer Simulation of a ‘Green Chemistry’ Room-Temperature Ionic Solvent,” *J. Phys. Chem. B*, vol. 106, no.

46, pp. 12017–12021, 2002.

[73] Z. Liu, S. Huang, and W. Wang, “A Refined Force Field for Molecular Simulation of Imidazolium-Based Ionic Liquids,” *J. Phys. Chem. B*, vol. 108, no. 34, pp. 12978–12989, 2004.

[74] I. Morrow Timothy and J. Maginn Edward, “Molecular Structure of Various Ionic Liquids from Gas Phase Ab Initio Calculations,” in *Ionic Liquids as Green Solvents*, vol. 856, no. 856, American Chemical Society, 2003, pp. 162–173.

[75] J. N. A. Canongia Lopes and A. A. H. Pádua, “Nanostructural Organization in Ionic Liquids,” *J. Phys. Chem. B*, vol. 110, no. 7, pp. 3330–3335, 2006.

[76] S. Stevanovic, A. Podgorsek, L. Moura, C. C. Santini, A. A. H. Padua, and M. F. Costa Gomes, “Absorption of Carbon Dioxide by Ionic Liquids with Carboxylate Anions,” *Int. J. Greenh. Gas Control*, vol. 17, no. 0, pp. 78–88, 2013.

[77] M. P. Allen and D. J. Tildesley, *Computer Simulations of Liquids*. Oxford: Clarendon Press, 1987.

[78] D. Frenkel and B. Smit, *Understanding Molecular Simulation: From Algorithms To Applications*, vol. 1. Academic press, 2001.

[79] G. H. Grant and W. G. (William G. Richards, *Computational chemistry*. Oxford University Press, 1996.

[80] W. F. Van Gunsteren and H. J. C. Berendsen, “A Leap-frog Algorithm for Stochastic Dynamics,” *Mol. Simul.*, vol. 1, no. 3, pp. 173–185, Mar. 1988.

[81] H. J. C. Berendsen, J. P. M. Postma, W. F. Vangunsteren, A. Dinola, and J. R. Haak, “Molecular-Dynamics with Coupling to an External Bath,” *J. Chem. Phys.*, vol. 81, no. 8, pp. 3684–3690, 1984.

[82] M. Parrinello and A. Rahman, “Crystal Structure and Pair Potentials: A Molecular-Dynamics Study,” *Phys. Rev. Lett.*, vol. 45, no. 14, pp. 1196–1199, Oct. 1980.

[83] D. J. Evans and B. L. Holian, “The Nose–Hoover thermostat,” *J. Chem. Phys.*, vol. 83, no. 8, pp. 4069–4074, Oct. 1985.

[84] W. F. Smith T. R.; Todorov I. T., “DL_POLY 2.20.” 2010.

[85] P. Atkins, J. De Paula, and J. Keeler, *Atkins’ Physical Chemistry*. Oxford University Press, 2018.

[86] P. P. Ewald, “The Calculation Of Optical And Electrostatic Grid Potential,” *Ann. Phys.*, vol. 64, no. 3, pp. 253–287, 1921.

[87] U. Essmann, L. Perera, M. L. Berkowitz, T. Darden, H. Lee, and L. G. Pedersen, “A Smooth Particle Mesh Ewald Method,” *J. Chem. Phys.*, vol. 103, no. 19, pp. 8577–8593, Nov. 1995.

[88] J. Canongia Lopes and A. H. Pádua, “CL&P: A Generic And Systematic Force Field For Ionic Liquids Modeling,” *Theor. Chem. Acc.*, vol. 131, no. 3, pp. 1–11, 2012.

[89] B. Kirchner and B. Clare, *Ionic Liquids*. Springer, 2009.

[90] J. N. Canongia Lopes, J. Deschamps, and A. A. H. Pádua, “Modeling Ionic Liquids Using a Systematic All-Atom Force Field,” *J. Phys. Chem. B*, vol. 108, no. 6, pp. 2038–2047, 2004.

[91] J. N. Canongia Lopes and A. A. H. Pádua, “Molecular Force Field for Ionic Liquids Composed of Triflate or Bistriflylimide Anions,” *J. Phys. Chem. B*, vol. 108, no. 43, pp. 16893–16898, 2004.

[92] J. N. Canongia Lopes and A. A. H. Pádua, “Molecular Force Field for Ionic

Liquids III: Imidazolium, Pyridinium, and Phosphonium Cations; Chloride, Bromide, and Dicyanamide Anions," *J. Phys. Chem. B*, vol. 110, no. 39, pp. 19586–19592, 2006.

[93] K. Shimizu, D. Almantariotis, M. F. C. Gomes, A. A. H. Pádua, and J. N. Canongia Lopes, "Molecular Force Field for Ionic Liquids V: Hydroxyethylimidazolium, Dimethoxy-2- Methylimidazolium, and Fluoroalkylimidazolium Cations and Bis(Fluorosulfonyl)Amide, Perfluoroalkanesulfonylamide, and Fluoroalkylfluorophosphate Anions," *J. Phys. Chem. B*, vol. 114, no. 10, pp. 3592–3600, 2010.

[94] J. Deschamps, M. F. Costa Gomes, and A. A. H. Pádua, "Molecular Simulation Study of Interactions of Carbon Dioxide and Water with Ionic Liquids," *Chemphyschem*, vol. 5, no. 7, pp. 1049–1052, 2004.

[95] F. Dommert, K. Wendler, R. Berger, L. Delle Site, and C. Holm, "Force Fields for Studying the Structure and Dynamics of Ionic Liquids: A Critical Review of Recent Developments," *Chemphyschem*, vol. 13, no. 7, pp. 1625–1637, 2012.

[96] V. V Chaban and O. V Prezhdo, "Computationally Efficient Prediction of Ionic Liquid Properties," *J. Phys. Chem. Lett.*, vol. 5, no. 11, pp. 1973–1977, 2014.

[97] J. C. Xu, S. Wang, W. Yu, Q. Q. Xu, W. B. Wang, and J. Z. Yin, "Molecular Dynamics Simulation for the Binary Mixtures of High Pressure Carbon Dioxide and Ionic Liquids," *Chinese J. Chem. Eng.*, vol. 22, no. 2, pp. 153–163, 2014.

[98] T. Köddermann, D. Reith, and R. Ludwig, "Comparison of Force Fields on the Basis of Various Model Approaches—How To Design the Best Model for the [CnMIM][NTf_2] Family of Ionic Liquids," *Chemphyschem*, vol. 14, no. 14, pp. 3368–3374, 2013.

[99] Y.-L. Wang, A. Lyubartsev, Z.-Y. Lu, and A. Laaksonen, "Multiscale Coarse-

Grained Simulations Of Ionic Liquids: Comparison Of Three Approaches To Derive Effective Potentials," *Phys. Chem. Chem. Phys.*, vol. 15, no. 20, pp. 7701–7712, 2013.

[100] F. Dommert *et al.*, "A Comparative Study Of Two Classical Force Fields On Statics And Dynamics Of [EMIM][BF_4] Investigated Via Molecular Dynamics Simulations," *J. Chem. Phys.*, vol. 129, no. 22, p. , 2008.

[101] T. Yan, C. J. Burnham, M. G. Del Pópolo, and G. A. Voth, "Molecular Dynamics Simulation of Ionic Liquids: The Effect of Electronic Polarizability," *J. Phys. Chem. B*, vol. 108, no. 32, pp. 11877–11881, 2004.

[102] O. Borodin, "Polarizable Force Field Development and Molecular Dynamics Simulations of Ionic Liquids," *J. Phys. Chem. B*, vol. 113, no. 33, pp. 11463–11478, 2009.

[103] F. Dommert and C. Holm, "Refining Classical Force Fields For Ionic Liquids: Theory And Application To [MMIM][Cl]," *Phys. Chem. Chem. Phys.*, vol. 15, no. 6, pp. 2037–2049, 2013.

[104] D. A. Case *et al.*, "AMBER 12." University of California, San Francisco, 2012.

[105] W. Smith and T. R. Forester, "DL_POLY_2.0: A general-purpose parallel molecular dynamics simulation package," *J. Mol. Graph.*, vol. 14, no. 3, pp. 136–141, 1996.

[106] I. T. Todorov, W. Smith, K. Trachenko, and M. T. Dove, "DL_POLY_3: New Dimensions In Molecular Dynamics Simulations Via Massive Parallelism," *J. Mater. Chem.*, vol. 16, no. 20, pp. 1911–1918, 2006.

[107] A. Padua, "fftool v1.0.0," Jun. 2015.

[108] L. Martínez, R. Andrade, E. G. Birgin, and J. M. Martínez, "PACKMOL: A Package For Building Initial Configurations For Molecular Dynamics

Simulations," *J. Comput. Chem.*, vol. 30, no. 13, pp. 2157–2164, 2009.

[109] J. M. Martínez and L. Martínez, "Packing Optimization For Automated Generation Of Complex System's Initial Configurations For Molecular Dynamics And Docking," *J. Comput. Chem.*, vol. 24, no. 7, pp. 819–825, May 2003.

[110] W. Humphrey, A. Dalke, and K. Schulten, "VMD: Visual molecular Dynamics," *J. Mol. Graph.*, vol. 14, no. 1, pp. 33–38, 1996.

[111] J. Wang, R. M. Wolf, J. W. Caldwell, P. A. Kollman, and D. A. Case, "Development And Testing Of A General Amber Force Field," *J. Comput. Chem.*, vol. 25, no. 9, pp. 1157–1174, 2004.

[112] R. Salomon-Ferrer, D. A. Case, and R. C. Walker, "An overview of the Amber biomolecular simulation package," *Wiley Interdiscip. Rev. Comput. Mol. Sci.*, vol. 3, no. 2, pp. 198–210, 2013.

[113] S. Zhang, N. Sun, X. He, X. Lu, and X. Zhang, "Physical Properties of Ionic Liquids: Database and Evaluation," *J. Phys. Chem. Ref. Data*, vol. 35, no. 4, pp. 1475–1517, 2006.

[114] T. Seiji, "Factors Controlling the Diffusion of Ions in Ionic Liquids," *ChemPhysChem*, vol. 13, no. 7, pp. 1664–1670, Apr. 2012.

[115] A. Heintz, J. K. Lehmann, E. Schmidt, and A. Wandschneider, "Diffusion Coefficients of Imidazolium Based Ionic Liquids in Aqueous Solutions," *J. Solution Chem.*, vol. 38, no. 8, pp. 1079–1083, Aug. 2009.

[116] A. F. Ferreira, P. N. Simões, and A. G. M. Ferreira, "Quaternary Phosphonium-Based Ionic Liquids: Thermal Stability And Heat Capacity Of The Liquid Phase," *J. Chem. Thermodyn.*, vol. 45, no. 1, pp. 16–27, 2012.

[117] A. Bhattacharjee, J. A. Lopes-da-Silva, M. G. Freire, J. A. P. Coutinho, and P.

J. Carvalho, “Thermophysical Properties Of Phosphonium-Based Ionic Liquids,” *Fluid Phase Equilib.*, vol. 400, pp. 103–113, Aug. 2015.

[118] K. Fraser and D. R. MacFarlane, *Phosphonium-Based Ionic Liquids: An Overview*, vol. 62. 2009.

[119] J. M. S. S. Esperança, H. J. R. Guedes, M. Blesic, and L. P. N. Rebelo, “Densities and Derived Thermodynamic Properties of Ionic Liquids. 3. Phosphonium-Based Ionic Liquids over an Extended Pressure Range,” *J. Chem. Eng. Data*, vol. 51, no. 1, pp. 237–242, Jan. 2006.

[120] X. Liu, G. Zhou, S. Zhang, and G. Yu, “Molecular Simulations Of Phosphonium-Based Ionic Liquid,” *Mol. Simul.*, vol. 36, no. 1, pp. 79–86, 2009.

[121] C. J. Bradaric, A. Downard, C. Kennedy, A. J. Robertson, and Y. Zhou, “Industrial Preparation Of Phosphonium Ionic Liquids,” *Green Chem.*, vol. 5, no. 2, pp. 143–152, 2003.

[122] S. F. R. Taylor *et al.*, “CO_2 Capture in Wet and Dry Superbase Ionic Liquids,” *J. Solution Chem.*, vol. 44, no. 3, pp. 511–527, Apr. 2015.

[123] S. Tsuzuki, W. Shinoda, H. Saito, M. Mikami, H. Tokuda, and M. Watanabe, “Molecular Dynamics Simulations of Ionic Liquids: Cation and Anion Dependence of Self-Diffusion Coefficients of Ions,” *J. Phys. Chem. B*, vol. 113, no. 31, pp. 10641–10649, Aug. 2009.

[124] C. Yue, D. Fang, L. Liu, and T.-F. Yi, “Synthesis And Application Of Task-Specific Ionic Liquids Used As Catalysts And/Or Solvents In Organic Unit Reactions,” *J. Mol. Liq.*, vol. 163, no. 3, pp. 99–121, 2011.

[125] X. Liu, G. Zhou, S. Zhang, and G. Yu, “Molecular Simulations Of Phosphonium-Based Ionic Liquid,” *Mol. Simul.*, vol. 36, no. 1, pp. 79–86, 2009.

[126] S. Sharma, A. Gupta, D. Dhabal, and H. K. Kashyap, “Pressure-Dependent

Morphology Of Trihexyl(Tetradecyl)Phosphonium Ionic Liquids: A Molecular Dynamics Study," *J. Chem. Phys.*, vol. 145, no. 13, p. 134506, Oct. 2016.

[127] D. M. Arkhipova, V. V Ermolaev, V. A. Miluykov, and O. G. Sinyashin, "Synthesis, Characterization, And Application Of Phosphonium Ionic Liquids," *Phosphorus. Sulfur. Silicon Relat. Elem.*, vol. 191, no. 11–12, pp. 1470–1471, Dec. 2016.

[128] M. Deetlefs, C. Hardacre, M. Nieuwenhuyzen, A. A. H. Padua, O. Sheppard, and A. K. Soper, "Liquid Structure of the Ionic Liquid 1,3-Dimethylimidazolium Bis{(trifluoromethyl)sulfonyl}amide," *J. Phys. Chem. B*, vol. 110, no. 24, pp. 12055–12061, Jun. 2006.

[129] M. E. Perez-Blanco and E. J. Maginn, "Molecular Dynamics Simulations of CO2 at an Ionic Liquid Interface: Adsorption, Ordering, and Interfacial Crossing," *J. Phys. Chem. B*, vol. 114, no. 36, pp. 11827–11837, 2010.

[130] M. Klähn and A. Seduraman, "What Determines CO_2 Solubility in Ionic Liquids? A Molecular Simulation Study," *J. Phys. Chem. B*, vol. 119, no. 31, pp. 10066–10078, Aug. 2015.

[131] L. Ferguson and P. Scovazzo, "Solubility, Diffusivity, and Permeability of Gases in Phosphonium-Based Room Temperature Ionic Liquids: Data and Correlations," *Ind. Eng. Chem. Res.*, vol. 46, no. 4, pp. 1369–1374, 2007.

[132] P. J. Carvalho, V. H. Álvarez, I. M. Marrucho, M. Aznar, and J. A. P. Coutinho, "High carbon Dioxide Solubilities In Trihexyltetradecylphosphonium-Based Ionic Liquids," *J. Supercrit. Fluids*, vol. 52, no. 3, pp. 258–265, 2010.

[133] J. J. Potoff and J. I. Siepmann, "Vapor–liquid Equilibria Of Mixtures Containing Alkanes, Carbon Dioxide, And Nitrogen," *AIChE J.*, vol. 47, no. 7, pp. 1676–1682, Jul. 2001.

[134] S. S. Moganty and R. E. Baltus, “Diffusivity of Carbon Dioxide in Room-Temperature Ionic Liquids,” *Ind. Eng. Chem. Res.*, vol. 49, no. 19, pp. 9370–9376, Oct. 2010.

[135] C. Moya, J. Palomar, M. Gonzalez-Miquel, J. Bedia, and F. Rodriguez, “Diffusion Coefficients of CO_2 in Ionic Liquids Estimated by Gravimetry,” *Ind. Eng. Chem. Res.*, vol. 53, no. 35, pp. 13782–13789, Sep. 2014.

[136] H. Liu, S. Dai, and D. Jiang, “Molecular Dynamics Simulation of Anion Effect on Solubility, Diffusivity, and Permeability of Carbon Dioxide in Ionic Liquids,” *Ind. Eng. Chem. Res.*, vol. 53, no. 25, pp. 10485–10490, Jun. 2014.

[137] V. Chaban, “Polarizability Versus Mobility: Atomistic Force Field For Ionic Liquids,” *Phys. Chem. Chem. Phys.*, vol. 13, no. 35, pp. 16055–16062, 2011.

Appendix I

CL&PFF

```
#           il.ff,
version
2017/12/06
                # Molecular force field for ionic liquids
                # Agilio Padua, J.N. Canongia Lopes
                # contributors: K. Shimizu, A. Podgorsek, F. Hammami, L. Gontrani, M. Mishra
                # questions to: agilio.padua@uca.fr
                #
                # units: kJ/mol, A, deg
                # bond and angle force constants are in the form k/2 (x - x0)^2
                # use 'cons' to indicate constrained bonds and angles
                # in improper dihedrals the central atom is the third in the list
                #
                # use with fftool to build input files for LAMMPS (or DLPOLY)


                ATOMS
                #     typ  m/u     q/e    pot   pars
                # dialkylimidazolium JPCB 108 (2004) 2038
                C1    CT  12.011  -0.17   lj    3.50   0.27614
                C2    CT  12.011   0.01   lj    3.50   0.27614
                CE    CT  12.011  -0.05   lj    3.50   0.27614
                CS    CT  12.011  -0.12   lj    3.50   0.27614
                CT    CT  12.011  -0.18   lj    3.50   0.27614
                CR    CR  12.011  -0.11   lj    3.55   0.29288
                CW    CW  12.011  -0.13   lj    3.55   0.29288
                HCR   HA   1.008   0.21   lj    2.42   0.12552
                HCW   HA   1.008   0.21   lj    2.42   0.12552
                HC    HC   1.008   0.06   lj    2.50   0.12552
                H1    HC   1.008   0.13   lj    2.50   0.12552
                NA    NA  14.007   0.15   lj    3.25   0.71128
                # dialkylmethylmidazolium JPCB 112 (2008) 5039
                CRM   CR  12.011   0.19   lj    3.55   0.29288
                NAM   NA  14.007   0.04   lj    3.25   0.71128
                CCR   CT  12.011  -0.26   lj    3.50   0.27614
                # aromatic OPLS-AA
                CA    CA  12.011  -0.115  lj    3.55   0.29288
                HA    HA   1.008   0.115  lj    2.42   0.12552
                # benzylimidazolium JPCB 117 (2013) 7416 (OPLS-AA benzyl ok)
```

```
C1T   CT  12.011   0.039  lj    3.50   0.27614
# toluene JACS 118 (1996) 11217; JCC 25 (2004) 1322
CAP   CA  12.011  -0.154  lj    3.55   0.29288
CAM   CA  12.011  -0.145  lj    3.55   0.29288
CAO   CA  12.011  -0.147  lj    3.55   0.29288
CAT   CA  12.011  -0.081  lj    3.55   0.29288
# CTT   CT  12.011  -0.197  lj    3.50   0.27614
HAT   HA   1.008   0.148  lj    2.42   0.12552
HT    HC   1.008   0.092  lj    2.42   0.12552
# pyridinium JPCB 110 (2006) 19586
NAP   NA  14.007   0.15   lj    3.25   0.71128
CAPO  CA  12.011   0.00   lj    3.55   0.29288
CAPM  CA  12.011  -0.07   lj    3.55   0.29288
CAPP  CA  12.011   0.02   lj    3.55   0.29288
HAP   HA   1.008   0.15   lj    2.42   0.12552
# isoquinolinium
NAQ   NA  14.007   0.305  lj    3.25   0.71128
CAQ   CA  12.011   0.185  lj    3.55   0.29288
# imidazolium fluoroalkyl JPCB 114 (2010) 3592
# fluoroalkyl OPLS-AA JPCA 105 (2001) 4118
C1H   CT  12.011  -0.05   lj    3.50   0.27614
C3F   CF  12.011   0.12   lj    3.50   0.27614
CTF   CF  12.011   0.36   lj    3.50   0.27614
CSF   CF  12.011   0.24   lj    3.50   0.27614
F     F   18.998  -0.12   lj    2.95   0.22175
# ammonium, pyrrolidinium JPCB 108 (2004) 16893
N4    NT  14.007   0.12   lj    3.25   0.71128
N3    NT  14.007   0.03   lj    3.25   0.71128
H3    HN   1.008   0.31   lj    0.00   0.00000
# alcohols OPLS-AA JACS 118 (1996) 11225; JPC 100 (1996) 18010
# cholinium same as OPLS-AA alcohols or ammonium (Ferid, Agilio)
CTO   CT  12.011   0.145  lj    3.50   0.27614
C2O   CT  12.011   0.205  lj    3.50   0.27614
H1O   HC   1.008   0.040  lj    2.50   0.12552
OH    OH  15.999  -0.683  lj    3.12   0.71128
HO    HO   1.008   0.418  lj    0.00   0.00000
# alkoxy imidazolium JPCB 114 (2010) 3595
COL   CT  12.011   0.275  lj    3.50   0.27614
# phosphonium OPLS-AA, JPCB 110 (2006) 19586
P3    PT  30.974   0.68   lj    3.74   0.83680
C1P   CT  12.011  -0.31   lj    3.50   0.27614
# lithium cation Aqvist
Li    Li   6.941  +1.00   lj    2.126  0.07648
# sodium cation
Na    Na  22.990  +1.00   lj    3.33   0.01160
# tetrafluoroborate anion
```

```
B     B   10.811   0.96   lj    3.58   0.39750
FB    F   18.998  -0.49   lj    3.12   0.25520
# hexafluorophosphate JCSPerkin2 (1999) 2365
P     P   30.974   1.34   lj    3.74   0.83680
FP    F   18.998  -0.39   lj    3.12   0.25520
# chloride JPCB 108 (2004) 2038
Cl    Cl  35.453  -1.00   lj    3.65   0.83000
# bromide JPCB 110 (2006) 19586
Br    Br  79.904  -1.00   lj    3.97   0.86000
# bistriflamide JPCB 108 (2004) 16893
F1    FB  18.998  -0.16   lj    2.95   0.22175
CBT   CF  12.011   0.35   lj    3.50   0.27614
SBT   SB  32.066   1.02   lj    3.55   1.04600
OBT   OB  15.999  -0.53   lj    2.96   0.87864
NBT   NB  14.000  -0.66   lj    3.25   0.71128
# triflate JPCB 108 (2004) 16893
OTF   OB  15.999  -0.63   lj    2.96   0.87864
# longer perfluoroalkanesulfonylamides
C1F   CF  12.011   0.19   lj    3.50   0.27614
# bis(fluorosulfonyl)amide
FSI   FB  18.998  -0.13   lj    2.95   0.22175
# dicyanamide JPCB 110 (2006) 19586
N3A   N3  14.000  -0.76   lj    3.25   0.71128
CZA   CZ  12.011   0.64   lj    3.30   0.27614
NZA   NZ  14.001  -0.76   lj    3.20   0.71128
# acetate OPLS-AA
O2    O2  15.999  -0.80   lj    2.96   0.87864
CO2   CO  12.011   0.70   lj    3.75   0.43932
CTA   CT  12.011  -0.28   lj    3.50   0.27614
# trifluorocetate PCCP 17 (2015) 22321
O2F   OC  15.999  -0.75   lj    2.96   0.87864
CFA   CF  12.011   0.40   lj    3.50   0.27614
FFA   F   18.998  -0.20   lj    2.95   0.22175
# alkylsulfates JPCB 112 (2008) 5039
SO    SO  32.066   1.18   lj    3.55   1.04600
OS4   OS  15.999  -0.65   lj    3.15   0.83700
OC4   OC  15.999  -0.45   lj    2.90   0.58600
CS4   CT  12.011   0.22   lj    3.50   0.27600
HS4   HC   1.008   0.00   lj    2.50   0.12600
# alkylsulfonates JPCB 112 (2008) 5039
OS3   OS  15.999  -0.68   lj    3.15   0.83700
CS3   CT  12.011  -0.14   lj    3.50   0.27600
HS3   HC   1.008   0.00   lj    2.50   0.12600
# thiocyanate JCP 128 (2008) 154504
SK    SK  32.066  -0.72   lj    3.55   1.04600
CK    CK  12.011   0.44   lj    3.40   0.35980
```

```
NK    NK  14.001  -0.72   lj    3.25   0.71128
# tricyanomethanide MG Martin STTR report 2008, our charges
#C3A  C3A  12.011  -0.910  lj    3.55   0.33742
#CN   CN   12.011   0.655  lj    3.12   0.83680
#NC   NC   14.001  -0.685  lj    3.30   2.51040
# tricyanomethanide OPLS nitriles, our charges
C3A  C3A  12.011  -0.910  lj    3.55   0.29288
CN   CN   12.011   0.655  lj    3.30   0.27614
NC   NC   14.001  -0.685  lj    3.20   0.71128


BONDS
# i j    pot    re/A    kr/kJmol-1
# alkanes OPLS-AA JACS118(1996)11225, JPC100(1996)18010
HC  CT   cons   1.090   2845.0
CT  CT   harm   1.529   2242.0
# aromatics AMBER JACS 117(1995)5179
CA  CA   harm   1.400   3924.6
CA  HA   cons   1.080   3071.1
# toluene AMBER JACS 117(1995)5179
CA  CT   harm   1.510   2652.7
# pyridinium JPCB110(2006)19586
CA  NA   harm   1.340   4042.0
# dialkylimidazolium JPCB108(2004)2038
CR  HA   cons   1.080   2845.0
CW  HA   cons   1.080   2845.0
CR  NA   harm   1.315   3992.0
CW  NA   harm   1.378   3574.0
CW  CW   harm   1.341   4352.0
NA  CT   harm   1.466   2820.0
# dialkylimethylmidazolium JPCB112(2008)5039
CR  CT   harm   1.510   2653.0
# fluoroalkyl JPCA105(2001)4118, JPCA106(2002)10116
CT  CF   harm   1.529   2242.6
F   CF   harm   1.332   3071.1
CF  CF   harm   1.529   2242.6
# ammonium, pyrrolidinium OPLS-AA JACS121(1999)4827, AMBER
NT  CT   harm   1.448   3196.6
HN  NT   cons   1.010   3632.0
# phosphonium OPLS-AA JPCB110(2006)19586
PT  CT   harm   1.81    3550.0
# hydroxyl OPLS-AA JACS 118(1996)11225, JPC 100(1996)18010
CT  OH   harm   1.410   2677.8
HO  OH   cons   0.945   4627.5
# tetrafluoroborate
B   F    harm   1.394   3235.0
```

```
# hexafluorophosphate JCSPerkin2(1999)2365
P   F    harm   1.606   3100.0
# triflate and bistriflamide JPCB108(2004)16893
FB  CF   harm   1.323   3698.0
CF  SB   harm   1.818   1950.0
SB  OB   harm   1.437   5331.0
NB  SB   harm   1.570   3137.0
# bis(fluorosulfonyl)amide
FB  SB   harm   1.575   1879.0
# dicyanamide JPCB110(2006)19586
N3  CZ   harm   1.310   4206.0
CZ  NZ   harm   1.157   5439.2
# acetate OPLS-AA
CO  O2   harm   1.250   5489.0
CT  CO   harm   1.522   2653.0
# alkylsulfates JPCB112(2008)5039
CT  OC   harm   1.402    745.8
OS  SO   harm   1.455   5331.0
OC  SO   harm   1.633   1789.6
# alkylsulfonates JPCB112(2008)
CT  SO   harm   1.792   1970.0
# thiocyanate JCP128(2008)154504, our MP2
SK  CK   harm   1.67    2836.8
CK  NK   harm   1.19   12221.5
# tricyanomethanide MG Martin STTR report 2008
#C3A  CN  harm   1.408   1799.12
#CN   NC  harm   1.167   5062.64
# tricyanomethanide OPLS nitriles
C3A  CN  harm   1.412   3347.2
CN   NC  harm   1.157   5439.2


ANGLES
# i j   k    pot    th/deg  ka/kjmol-1
# alkyl OPLS-AA JACS118(1996)11225, JPC100(1996)18010
CT  CT  CT   harm   112.7   488.3
CT  CT  HC   harm   110.7   313.8
HC  CT  HC   harm   107.8   276.1
# aromatics AMBER JACS 117(1995)5179
CA  CA  HA   harm   120.0   292.9
CA  CA  CA   harm   120.0   527.2
# toluene AMBER JACS 117(1995)5179
CA  CA  CT   harm   120.0   585.8
CA  CT  HC   harm   109.5   418.4
# pyridinium JPCB110(2006)19586
CA  NA  CA   harm   120.4   585.8
```

CA NA CT harm 119.8 585.8
CA CA NA harm 120.0 585.8
NA CA HA harm 120.0 292.9
dialkylimidazolium JPCB108(2004)2038
CW NA CR harm 108.0 585.8
CW NA CT harm 125.6 585.8
CR NA CT harm 126.4 585.8
NA CR HA harm 125.1 292.9
NA CR NA harm 109.8 585.8
NA CW CW harm 107.1 585.8
NA CW HA harm 122.0 292.9
CW CW HA harm 130.9 292.9
NA CT HC harm 110.7 313.8
NA CT CT harm 112.7 488.3
dialkylimethylmidazolium JPCB112(2008)5039
CT CR NA harm 125.8 585.8
CR CT HC harm 110.7 313.8
benzylimidazolium AMBER
NA CT CA harm 111.2 669.4
fluoroalkyl JPCA105(2001)4118, JPCA106(2002)10116
HC CT CF harm 110.7 313.8
F CF CT harm 109.5 418.4
CT CF CF harm 112.7 488.3
CT CT CF harm 112.7 488.3
F CF F harm 109.1 644.3
F CF CF harm 109.5 418.4
CF CF CF harm 112.7 488.3
ammonium, pyrrolidinium OPLS-AA JACS121(1999)4827, AMBER
NT CT CT harm 109.5 470.3
CT NT CT harm 107.2 433.5
HC CT NT harm 109.5 292.9
HN NT CT harm 109.5 292.9
phosphonium OPLS-AA, JPCB110(2006)19586
CT PT CT harm 109.5 607.8
HC CT PT harm 110.1 389.9
CT CT PT harm 115.2 509.1
hydroxyl JACS 118(1996)11225, JPC 100(1996)18010
CT CT OH harm 109.5 418.4
HC CT OH harm 109.5 292.9
CT OH HO harm 108.5 460.2
tetrafluoroborate anion
F B F harm 109.5 669.5
hexafluorophosphate JCSPerkin2(1999)2365
F P F harm 90.0 1165.0
triflate and bistriflamide JPCB108(2004)16893
FB CF FB harm 107.1 781.0

```
FB  CF  SB   harm   111.7   694.0
OB  SB  OB   harm   118.5   969.0
CF  SB  OB   harm   102.6   870.0
NB  SB  OB   harm   113.6   789.0
NB  SB  CF   harm   103.5   764.0
SB  NB  SB   harm   125.6   671.0
# longer perfluoroalkanesulfonylamides
SB  CF  CF   harm   115.9   418.4
FB  CF  CF   harm   109.5   418.4
# bis(fluorosulfonyl)amide
FB  SB  OB   harm   104.1  1077.0
FB  SB  NB   harm   103.0   902.0
# dicyanamide JPCB110(2006)19586
CZ  N3  CZ   harm   118.5   362.0
N3  CZ  NZ   harm   175.2   425.0
# acetate OPLS-AA JPCB (2004)
O2  CO  O2   harm   126.0   669.4
CT  CO  O2   harm   117.0   585.8
HC  CT  CO   harm   109.5   298.9
# trifluoroacetate OPLS-AA
F   CF  CO   harm   109.5   418.4
CF  CO  O2   harm   117.0   585.8
# alkylsulfates JPCB112(2008)5039
OS  SO  OS   harm   114.0   969.0
OC  SO  OS   harm   103.5  1239.6
CT  OC  SO   harm   116.6   300.5
HC  CT  OC   harm   109.7   488.7
CT  CT  OC   harm   107.8   765.6
# alkylsulfonates JPCB112(2008)5039
CT  SO  OS   harm   104.5   870.0
HC  CT  SO   harm   107.3   390.3
CT  CT  SO   harm   113.3   583.0
# thiocyanate JCP128(2008)154504
SK  CK  NK   harm   180.0   651.9
# tricyanomethanide MG Martin STTR report 2008
#C3A CN  NB   harm   180.0   251.04
#CN  C3A CN   harm   120.0   368.19
# tricyanomethanide OPLS nitriles
C3A CN  NC   harm   180.0   1255.2
CN  C3A CN   harm   120.0    585.8


DIHEDRALS
# i j   k   l   pot    v1       v2       v3       v4
# alkanes OPLS-AA JACS 118 (1996) 11225; JPC 100 (1996) 18010
HC  CT  CT  HC   opls   0.0000    0.0000    1.2552    0.0000
```

CT CT CT HC opls 0.0000 0.0000 1.2552 0.0000
CT CT CT CT opls 5.4392 -0.2092 0.8368 0.0000
aromatics AMBER JACS 117 (1995) 5179
CA CA CA CA opls 0.0000 30.3340 0.0000 0.0000
CA CA CA HA opls 0.0000 30.3340 0.0000 0.0000
HA CA CA HA opls 0.0000 30.3340 0.0000 0.0000
toluene AMBER JACS 117 (1995) 5179
CT CA CA CA opls 0.0000 30.3340 0.0000 0.0000
CT CA CA HA opls 0.0000 30.3340 0.0000 0.0000
CA CA CT HC opls 0.0000 0.0000 0.0000 0.0000
pyridinium JPCB 110 (2006) 19586
NA CA CA CA opls 0.0000 30.3340 0.0000 0.0000
NA CA CA HA opls 0.0000 30.3340 0.0000 0.0000
CA NA CA CA opls 0.0000 12.5520 0.0000 0.0000
CA NA CA HA opls 0.0000 12.5520 0.0000 0.0000
CT NA CA CA opls 0.0000 12.5520 0.0000 0.0000
CT NA CA HA opls 0.0000 12.5520 0.0000 0.0000
CA NA CT HC opls 0.0000 0.0000 0.0000 0.0000
CA NA CT CT opls 0.0000 1.0920 0.0000 0.7930
dialkylimidazolium JPCB 108 (2004) 2038
CW NA CR NA opls 0.0000 19.4600 0.0000 0.0000
CW NA CR HA opls 0.0000 19.4600 0.0000 0.0000
CT NA CR NA opls 0.0000 19.4600 0.0000 0.0000
CT NA CR HA opls 0.0000 19.4600 0.0000 0.0000
CR NA CW CW opls 0.0000 12.5520 0.0000 0.0000
CR NA CW HA opls 0.0000 12.5520 0.0000 0.0000
CT NA CW CW opls 0.0000 12.5520 0.0000 0.0000
CT NA CW HA opls 0.0000 12.5520 0.0000 0.0000
NA CW CW NA opls 0.0000 44.9800 0.0000 0.0000
NA CW CW HA opls 0.0000 44.9800 0.0000 0.0000
HA CW CW HA opls 0.0000 44.9800 0.0000 0.0000
CW NA CT HC opls 0.0000 0.0000 0.5190 0.0000
CR NA CT HC opls 0.0000 0.0000 0.0000 0.0000
CW NA CT CT opls -7.1535 6.1064 0.7939 0.0000
CR NA CT CT opls -5.2691 0.0000 0.0000 0.0000
NA CT CT CT opls -7.4797 3.1642 -1.2026 0.0000
NA CT CT HC opls 0.0000 0.0000 0.3670 0.0000
dialkylimethylmidazolium JPCB 112 (2008) 5039
CW NA CR CT opls 0.0000 19.4600 0.0000 0.0000
CT NA CR CT opls 0.0000 19.4600 0.0000 0.0000
NA CR CT HC opls 0.0000 0.0000 0.0000 0.0000
benzylimidazolium AMBER wildcards
NA CT CA CA opls 0.0000 0.0000 0.0000 0.0000
CA CT NA CR opls 0.0000 0.0000 0.0000 0.0000
fluoroalkyl JPCA 105 (2001) 4118; JPCA 106 (2002) 10116
F CF CT HC opls 0.0000 0.0000 1.2134 0.0000

F CF CT CT opls 0.0000 0.0000 1.9372 0.0000
F CF CF CT opls 0.0000 0.0000 2.7656 0.0000
HC CT CT CF opls 0.0000 0.0000 0.5565 0.0000
HC CT CF CF opls 0.0000 0.0000 0.7573 0.0000
CF CF CF CT opls 14.6750 -0.9179 -2.8980 -2.0174
CF CF CT CT opls -0.5881 -0.7642 -0.3170 -0.3179
CF CT CT NA opls 0.0000 0.0000 0.0000 0.0000
F CF CF F opls -10.4600 0.0000 1.0460 0.0000
F CF CF CF opls 1.2552 0.0000 1.6736 0.0000
CF CF CF CF opls 27.7064 3.9664 -5.8074 -8.8617
ammonium, pyrrolidinium OPLS-AA JACS 121 (1999) 4827
HC CT CT NT opls -4.2384 -2.9665 1.9790 0.0000
CT CT CT NT opls 10.0081 -2.8200 2.3012 0.0000
CT NT CT CT opls 1.7405 -0.5356 2.9079 0.0000
HC CT NT CT opls 0.0000 0.0000 2.3430 0.0000
HN NT CT HC opls 0.0000 0.0000 1.6736 0.0000
HN NT CT CT opls -0.7950 -1.7447 1.7489 0.0000
cholinium: unpublished
OH CT CT NT opls -44.0515 -5.4349 0.0000 0.0000
#OH CT CT NT opls -44.0515 -5.0148 0.0000 -3.1510
phosphonium OPLS-AA, JPCB 110 (2006) 19586
CT PT CT HC opls 0.0000 0.0000 0.9270 0.0000
CT PT CT CT opls 0.0000 0.0000 1.1330 0.0000
PT CT CT HC opls 0.0000 0.0000 0.4650 0.0000
PT CT CT CT opls -3.2480 0.9880 -0.7150 0.0000
hydroxyl JACS 118 (1996) 11225; AMBER98 (OCCO) 117 (1995) 5179
HC CT OH HO opls 0.0000 0.0000 1.8828 0.0000
CT CT OH HO opls -1.4895 -0.7280 2.0585 0.0000
HC CT CT OH opls 0.0000 0.0000 1.9581 0.0000
OH CT CT OH opls 0.0000 -9.8324 1.2050 0.0000
triflate and bistriflamide JPCB 108 (2004) 16893
OB SB CF FB opls 0.0000 0.0000 1.4510 0.0000
NB SB CF FB opls 0.0000 0.0000 1.3220 0.0000
OB SB NB SB opls 0.0000 0.0000 -0.0150 0.0000
SB NB SB CF opls 32.7730 -10.4200 -3.1950 0.0000
longer perfluoroalkanesulfonylamides
F CF CF FB opls -10.4600 0.0000 1.0460 0.0000
SB CF CF FB opls 0.0000 0.0000 1.4530 0.0000
SB CF CF F opls 0.0000 0.0000 1.4530 0.0000
OB SB CF CF opls 0.0000 0.0000 -0.7400 0.0000
NB SB CF CF opls -3.0940 0.0000 0.0000 0.0000
SB CF CF CF opls 50.0900 0.0000 -4.6260 -4.0080
bis(fluorosulfonyl)amide
FB SB NB SB opls 13.4514 -12.3373 -8.4874 -2.8654
dicyanamide JPCB 110 (2006) 19586
NZ CZ N3 CZ opls 4.0800 0.0000 0.0000 0.0000

```
# acetate OPLS-AA JPCB (2004)
HC  CT  CO  O2   opls   0.0000    0.0000    0.0000    0.0000
# trifluoroacetate
F   CF  CO  O2   opls   0.0000    0.0000    0.0000    0.0000
# alkylsulfates JPCB 112 (2008) 5039
OS  SO  OC  CT   opls   0.0000    0.0000    2.4815    0.0000
SO  OC  CT  HC   opls   0.0000    0.0000    1.6858    0.0000
SO  OC  CT  CT   opls  -6.0142   -3.1133    1.4941    0.0000
OC  CT  CT  HC   opls   0.0000    0.0000    2.0698    0.0000
OC  CT  CT  CT   opls   4.3893   -1.8273    2.9705    0.0000
# alkylsulfonates JPCB 112 (2008) 5039
OS  SO  CT  HC   opls   0.0000    0.0000    1.6250    0.0000
OS  SO  CT  CT   opls   0.0000    0.0000    1.3938    0.0000
SO  CT  CT  HC   opls   0.0000    0.0000    1.3797    0.0000
SO  CT  CT  CT   opls -16.1000   -2.0046    0.7674    0.0000
# tricyanomethanide
# NC  CN  C3A CN   opls   0.0000    0.0000    0.0000    0.0000


IMPROPER
# improper C aromatics AMBER JACS 117 (1995) 5179
CA  CA  CA  HA   opls   0.0000    9.2048    0.0000    0.0000
CA  CA  CA  CA   opls   0.0000    9.2048    0.0000    0.0000
CA  CA  CA  CT   opls   0.0000    9.2048    0.0000    0.0000
CA  CA  NA  CT   opls   0.0000    9.2048    0.0000    0.0000
CA  NA  CA  HA   opls   0.0000    9.2048    0.0000    0.0000
# improper imidazolium ring AMBER JACS 117 (1995) 5179
CR  CW  NA  CT   opls   0.0000    8.3680    0.0000    0.0000
CR  CW  NA  HA   opls   0.0000    8.3680    0.0000    0.0000
NA  NA  CR  HA   opls   0.0000    9.2048    0.0000    0.0000
NA  NA  CR  CT   opls   0.0000    9.2048    0.0000    0.0000
NA  CW  CW  HA   opls   0.0000    9.2048    0.0000    0.0000
# improper tricyanomethanide AMBER JACS 117 (1995) 5179
CN  CN  C3A CN   opls   0.0000    9.2048    0.0000    0.0000
# improper carbonyl AMBER JACS 117 (1995 )5179
CT  O2  CO  O2   opls   0.0000   87.8640    0.0000    0.0000
```

TraPPE FF for CO_2

Nonbonded Interactions

#	(pseudo)atom	type	ε/k_B [K]	σ [Å]	q [e]
1	C	O=[C]=O	27.0	2.800	0.700
2	O	[O]=C=O	79.0	3.050	-0.350
3	O	[O]=C=O	79.0	3.050	-0.350

Bond Lengths

#	Stretch	Type	Length [Å]
1	1 – 2	O=(C=O)	1.160
2	2 – 3	O=(C=O)	1.160

Bond Angles

#	Bend	Type	θ [°]
1	2 – 1 – 3	O=(C)=O	180.0

Supporting Information for:

Water Solubility and Dynamics of CO2 Capture Ionic Liquids Having Aprotic Heterocyclic Anions Hao Wu, Edward J. Maginn*

* Electronic mail: ed@nd.edu Force Field Parameters

(Only for Benzim (BnIm))

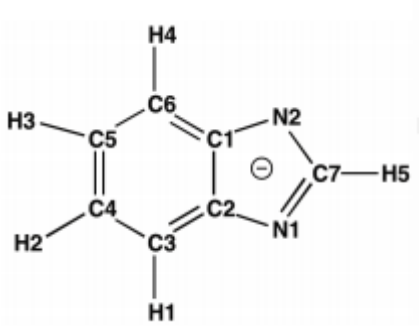

Table S1 Lennard-Jones Parameters and Atom Charges

Atom name Atom type σ (Å) ε (kJ/mol) Atom charge

BnIm				
C1	ca	3.400	0.3598	0.475081
C2	ca	3.400	0.3598	0.475081
C3	ca	3.400	0.3598	-0.373863
C4	ca	3.400	0.3598	-0.217454
C5	ca	3.400	0.3598	-0.217454
C6	ca	3.400	0.3598	-0.373863
C7	cc	3.400	0.3598	0.502687
H1	ha	2.600	0.0628	0.149782
H2	ha	2.600	0.0628	0.109643
H3	ha	2.600	0.0628	0.109643
H4	ha	2.600	0.0628	0.149782
H5	h5	2.421	0.0628	0.000257
N1	nc	3.250	0.7112	-0.844661
N2	nc	3.250	0.7112	-0.844661

Table S2 Bond Parameters

Atom 1 Atom 2 K b (kJ/mol) r 0 (Å)

BnIm			
ca	ca	2002	1.387
ca	nc	2062	1.336
ca	ha	1440	1.087
cc	h5	1489	1.079
cc	nc	1806	1.376

Table S3 Angle Parameters

Atom 1 Atom 2 Atom 3 K θ (kJ/mol) θ 0 (deg)

BnIm				
ca	ca	ca	281.1	119.97
ca	ca	nc	293.5	119.72
ca	ca	ha	202.7	120.01
ca	nc	cc	291.3	110.07
h5	cc	nc	206.2	123.7
nc	cc	nc	284.8	123.87

Table S4 Dihedral Parameters

Atom 1	Atom 2	Atom 3	Atom 4	K φ (kJ/mol)	n	γ (deg)
BnIm						
ca	ca	ca	ca	15.17	2	180
ca	ca	ca	ha	15.17	2	180
ca	ca	nc	cc	20.08	2	180
h5	cc	nc	ca	19.87	2	180
nc	cc	nc	ca	19.87	2	180
ca	ca	ca	nc	15.17	2	180
ha	ca	ca	nc	15.17	2	180
ha	ca	ca	ha	15.17	2	180
nc	ca	ca	nc	15.17	2	180

Table S5 Improper Torsion Parameters

Atom 1	Atom 2	Atom 3	Atom 4	Kφ (kJ/mol)	n	γ (deg)
BnIm						
ca	ca	ca	nc	4.602	2	180
ca	ca	ca	ha	4.602	2	180
h5	nc	cc	nc	4.602	2	180

Appendix II

Benchmarking on Archer for AMBER, DL_POLY Classic, DL_POLY 4

250 IPs of $P_{66614}Cl$ was modelled for 30 ps.

Number of Cores/ Running Time in minutes	DL_POLY Classic	DL_POLY 4	AMBER
24	73.6	30.5	4.2
48	43.9	23.7	3.4
72	37.4	Na**	3.2
96	28.3	Na**	2.9

** DL_POLY 4 uses domain decomposition parallelism which limits the number of atoms per core.